MULTISCALE CHARACTERIZATION OF MECHANICAL AND FRACTURE PROPERTIES OF CORTICAL BONE SPECIMENS

BY

KAVYA MENDU

THESIS

Submitted in partial fulfillment of the requirements
for the degree of Master of Science in Civil Engineering
in the Graduate College of the
University of Illinois at Urbana-Champaign, 2017

Urbana, Illinois

Adviser:

Assistant Professor Ange-Therese Akono

ABSTRACT

Bone is a hierarchical material with multiple length scales ranging from mineralized collagen fibrils at the nanoscale, single lamella at the sub microscale, lamellar structure at the microscale, osteons at the mesoscale to a whole bone at the macroscale. Several fracture testing methods are available including the three-point bending test, the compact tension test and the double cantilever test. However, these methods are confined to the macroscopic scale. At the microscopic scale, Vickers Fracture Indentation was proposed. Nevertheless, the study observed instances of varied crack lengths making it irreproducible and thus there is a need for further advancement on the testing front at the lower length scales. The research objective is to measure the fracture properties of bone at the level of osteons and at lower length scales using scratch testing. Cortical Bone Specimens obtained from porcine and bovine femurs have been cut, ground, polished and tested using an arduous experimental procedure. The nature of the fracture observed exhibited a strong anisotropy with toughening mechanisms and a competition between plastic flow and brittle fracture. Scanning Electron Microscopy revealed the presence of micro cracking, crack bridging, crack deflection and flaking or chipping along the length of the scratch. The process of applying nonlinear fracture mechanics methodologies such as the *J*-integral or the energetic size effect law in the analysis used to determine the fracture toughness of bone was meticulous. The results of this investigation showed not only a coupling between elasticity and fracture characteristics but also a

mixed mode fracture involved in the determination of the fracture resistance. The investigation employs scratch tests which determine the fracture properties not only at the microscale but also at the lower length scales due to the scalability of the scratch tests. Furthermore, nanoindentation tests were conducted on cortical bone specimens to determine their mechanical properties. Due to the viscoelasticity and viscoplasticity exhibited by cortical bone specimens, creep induced rate effect studies were carried out and their influence on the fracture properties was studied. The presented research paves the way towards a deeper understanding of the fragility of hard biological tissues. The knowledge gained could be applied to inform novel treatment for bone diseases, prevention of bone brittlement and design of advanced structural materials.

ACKNOWLEDGEMENTS

The success and outcome of this thesis is a result of lot of assistance and support from many people. I would like to extend my deep gratitude to my advisor, Dr. Ange Therese Akono for her patience and constant guidance through the course of this study. I feel lucky to have been associated with her. Thank you for being a constant source for encouragement and inspiration. I am grateful to the donors of the Ravindra Kinra and Kavita Kinra Fellowship which supported my graduate studies I further extend my gratitude towards Beckman Institute and Frederick Seitz Material Science Laboratory at University of Illinois at Urbana Champaign for providing me with advanced technology useful for my study.

I would like to take this opportunity to thank my lab mates Jiaxin Chen, Pooyan Kabir, Yue Cui, Radhika Pavgi and Caroline Johnson for their support and friendship. Thank you to Amrita Kataruka and Orieka Okeoghene for your association in the Bone project as well. I also thank my undergraduate assistant, Jasmine Puthuvelil for being very helpful. I also extend my greetings to my friends who have been a part of this journey. Finally, I would like to whole heartedly thank my parents for their unwavering support and guidance. Thank you for always guiding me through the right path.

TABLE OF CONTENTS

CHAPTER 1

INTRODUCTION

1.1 Industrial Context

Bone that forms the skeletal system provides structural functions such as support, mobility and protection to the human body. Bones are complex hierarchical structures. These multifunctional organs sustain the loads applied onto them due to the self-weight of the body or other external factors.

Fracture of bones can occur due to various reasons such as age, diseases and sudden impact loads or stresses (Ritchie, 2010). Depending on the nature, fracture can be treated by the following methods such as, surgical or conservative. Conservative methods of treatment include pain management, immobilization of the fractured bone using a cast or a sort of bone stabilization followed by natural healing of the bone. Whereas, surgical methods are used for fractures with highly impaired bones or at locations which aren't very suitable for conservative methods. Hip fractures due to osteoporosis are the examples of fractures treated surgically. As described by the International Osteoporosis Foundation (IOF), osteoporosis, meaning porous bone, is a disease in which the density and quality of the bone are reduced. Thus the bones become porous and fragile. According to the US Department of Health and Human services, diseases like osteoporosis

increases the risk of bone fracture. Further, fracture treatment remains one of the most expensive treatments and is an economic burden on the individual and the family.

According to the International Osteoporosis Foundation (IOF), worldwide, osteoporosis results in 8.9 million fractures annually, causing an osteoporotic fracture every 3 seconds. Hip, forearm and clinical vertebral fractures are reportedly the fractures faced by patients suffering from osteoporosis. Bone, being a living tissue has the property of cyclic replacement of the old bone cells with that of the new ones. For an individual affected by osteoporosis, the rate at which the bones rebuild the new cells is lower than the rate at which the old ones are detached. Thus, a loss in the bone mass occurs, increasing the risk of fractures.

To reduce the risk and occurrence of fractures, improvement in the prevention and treatment methodologies is an ideal solution. To attain such an advancement, a better understanding of the bone structure is required. Bone being a hierarchical material, there is a need to study the mechanical and fracture properties at various length scales. A fundamental understanding is necessary to improve the design of the bone implants or bone grafts to make them more suitable to the existing bone structure by matching its functionality and properties at all levels. Furthermore, an understanding of the bone structure at various levels helps to design materials with better properties, such as lighter weight, higher toughness and simultaneously equipped with self-healing mechanisms.

1.2 Research Objective

Bone has a low density, high strength, high toughness and resists fracture through toughening mechanisms (Feng et al., 2012). The toughening mechanisms are of two types. Intrinsic toughening mechanisms such as micro cracking and crack deflection induce ductility into the material. They also result in extended plasticity. Extrinsic toughening mechanisms include crack bridging which prevents the macro cracks from propagating upon the application of stress (Zimmerman et al., 2012).

The last quarter of the century was dedicated to understand the bone structure and strength and this led to several studies directed to determine the properties of bone specimens. Compact tension tests, three -point bending tests on single notched specimens were among the macroscopic tests conducted on this front (Behiri and Bonfield, 1980; Wright and Hayes, 1977; Rho et al, 1977). Although, these methodologies yielded in a better understanding of bone mainly at the macroscopic level, there is a need to study the different properties at meso, micro and nano scales. This resulted in further advancements in the experimental methodologies.

Thus, the objective of this study is to investigate the mechanical and fracture properties of bone at smaller length scales. Nano indentation tests were used to study the properties at the nanoscale or the submicron scale. The tests provide the elastic modulus and hardness of the bone. These mechanical properties are related to the fracture toughness of bone. Fracture toughness of bone is

expressed in terms of the stress intensity factor, K_c, which is the measure of resistance of bone to brittle fracture (Nalla et al., 2005). To understand these fracture properties at the microscopic length scale, a novel experimental technique, the micro scratch test was adopted on the bone specimens. These tests unlike the large-scale mechanical tests require smaller volumes of specimens. Thus, a large number of specimens are available from whole bones. Further, methods like optical microscopy and scanning electron microscopy were used in conjunction with the above testing procedures to attain microstructural information of the material. Chemical characterization of bone was performed using the X-ray diffraction studies. The porcine or swine bone specimens were tested due to their histological similarity to the human bones (Feng et al., 2012). Bovine bone specimens were also tested in order to probe specimens with larger corresponding areas, thus facilitating more tests on a single specimen.

1.3 Thesis Outline

This report is structured into five major parts. Part I is a general presentation which provides the introduction and industrial context pertaining to the study. It also puts forth the research objective and introduces the testing methodologies adopted for the study. Part II of the thesis provides an account of the microstructural characterization of cortical bone. Chapter 2 presents an extensive literature review of the bone histology, an account of the various experimental techniques developed over the years and an emphasis on the need for multiscale modeling of materials as

pointed out by several researchers. Chapter 3 explains the various imaging or microscopy techniques used in this study for the advanced material characterization. Chapter 4 provides an account of the range of equipment used for the determination of the chemical composition of the material. The principles upon which the instruments are designed and the specimens used for the study are thoroughly explained.

The next part, Part III, is devoted to micro scratch testing on the cortical bone specimens. Chapter 5 describes the theory of scratch testing and the description of the micro scratch testing equipment used for testing the cortical bone specimens. Chapter 6 explains the novel application of the micro scratch testing on the cortical bone specimens. The rigorous procedure adopted to obtain flat and polished specimens for the micro scale testing is described in detail as well.

Part IV consists of two chapters. Chapter 7 describes the theory of indentation and the Oliver and Pharr method used for the analysis of the load displacement curves obtained from the indentation technique. It also describes the nanoindentation testing equipment used for the study. Chapter 8 gives a detailed account of the application of the nanoindentation technique to the cortical bone specimens. It also describes the analysis and results obtained from the tests.

Part V consists of two chapters. Bone being a heterogeneous material with creep effects, requires a rate effect analysis. This analysis and testing procedures are described in chapter 9.

Chapter 10 summarizes the mechanical and fracture properties obtained from the analysis of the numerous tests conducted as a part of this research. It also lists the conclusions drawn from this study and provides the perspectives for future work and open questions related to the research.

1.4 Research Objectives/Significance

A multiscale investigation of mechanical and fracture properties of bone specimens is required in order to better understand the different hierarchical levels of bone structure. Adopting testing methodologies such as micro scratch tests and nanoindentation tests will improve the understanding of the bone microstructure. The scalability and reproducibility of the tests leads to the possibility of upscaling the mechanical and fracture properties to the macroscale after their determination at the microscale.

In addition, the study forms a basis for the implementation of a novel experimental technique, micro scratch tests, which can hereafter be useful for the determination of the fracture properties of complex materials like bone. Thus, this research not only deepens the understanding of fracture processes but also may contribute to the improvement of health care by enabling the development of bone implants or grafts with enhanced-performance.

1.5 Chapter Summary

This chapter provides an introduction to the investigation of the mechanical and fracture characteristics of cortical bone specimens. It describes the significance of the research and the corresponding industrial context. The chapter also introduces the various testing procedures which are used as tools for this study. A thesis outline is defined as well.

CHAPTER 2

LITERATURE REVIEW

2.1 Multiscale Thought Model of Cortical Bone

"The human skeleton is a mechanically optimized biological system whose composition and organization reflect the functional demands made on it."

Thomas Einhorn (1992)

The mechanical demands have a huge influence on the bone biology. Bone is characterized by huge variability and diversity. Researchers attributed this variability to the hierarchical organization of bone in conjunction with constitutive relations that define the materials properties (Fritsch and Hellmich, 2006). Furthermore, bone is regarded as a structural material with low density yet high strength, high stiffness and high fracture toughness. These collective properties are ideal attributes for material scientists. A very important necessity and area of research is the coexistence of strength and toughness in materials, along with a low strength to weight ratio (Ritchie, 2011). Strength is the ability of the material to resist the permanent deformation under an applied load. Toughness is the ability of the material to absorb mechanical energy without crack propagation. There is always a need to develop materials with optimized strength and toughness.

This natural integration of strength and toughness is observed in bone. Thus, bone has garnered a lot of interest in the research community for the past several decades.

Numerous studies (Akkus et al.,2003; Bonfield, 2011; Brown, 2000; Norman et al. 1995; Weiner and Wagner 1998) have been conducted over the past to study the various levels of hierarchical bone structure. The exceptional mechanical properties of bone are thought to result from this hierarchical structure and complex heterogeneity over various levels from the nanoscopic to the macroscopic length scales (Feng and Jasuik, 2011).

Bone mineral is mainly composed of calcium, phosphorus, oxygen and hydrogen. Moreover, mineralized collagen fibrils are considered as the building blocks of the bone material and are thought to perform important mechanical functions (Fei and Asa 2011). Collagen is made up of amino acids, which are in turn made up of carbon, nitrogen, oxygen and hydrogen. Collagen is the most abundant protein in the animal kingdom. Collagen molecules are considered to be of 16 types, yet three major types are said to be abundantly available in the body, types I, II and III (Gerard et. al., 2000).

Bone, a basic unit of human skeletal system can be classified based on its location, shape, size or structure. For instance, bones located in the skull, pelvis or ribs are flat shaped. Whereas, bones located in the limbs are tubular shaped and the ones located in the face are irregular. Bones

in specific tendons are sesamoid in shape. Furthermore, with regards to size, tubular bones located in the limbs are long while the cuboidal shaped bones located in the foot or wrist are short.

Bones located at different locations have different designations. For example, the bone located at the knee cap is known as patella, the one immediately above the knee cap is known as femur and the ones immediately below it are tibia and fibula. Femur and tibia, the long tubular bones, can be divided into three major components along their length. As shown in Figure 2.1, the components are: diaphysis, metaphysis and epiphysis (Hill, 2017). Epiphysis can be further classified into distal epiphysis and proximal epiphysis. The diaphysis region corresponds to the elongated hollow central part of the bone, which consists of thick compact or cortical bone and encompasses the medullary cavity or the bone marrow. The epiphysis regions correspond to the ends of the bone, and are mainly composed of trabecular or cancellous bone. The proximal epiphysis region is that end of the bone which is closer to the central part of the body. Whereas, the distal epiphysis is the end which is farther from the central part of the body. The region which forms a connection between the diaphysis and epiphysis is the metaphysis region. This region enables the bone to grow and consists of the connecting cartilage too. The metaphysis region generally disappears with age, as the bone is fully formed.

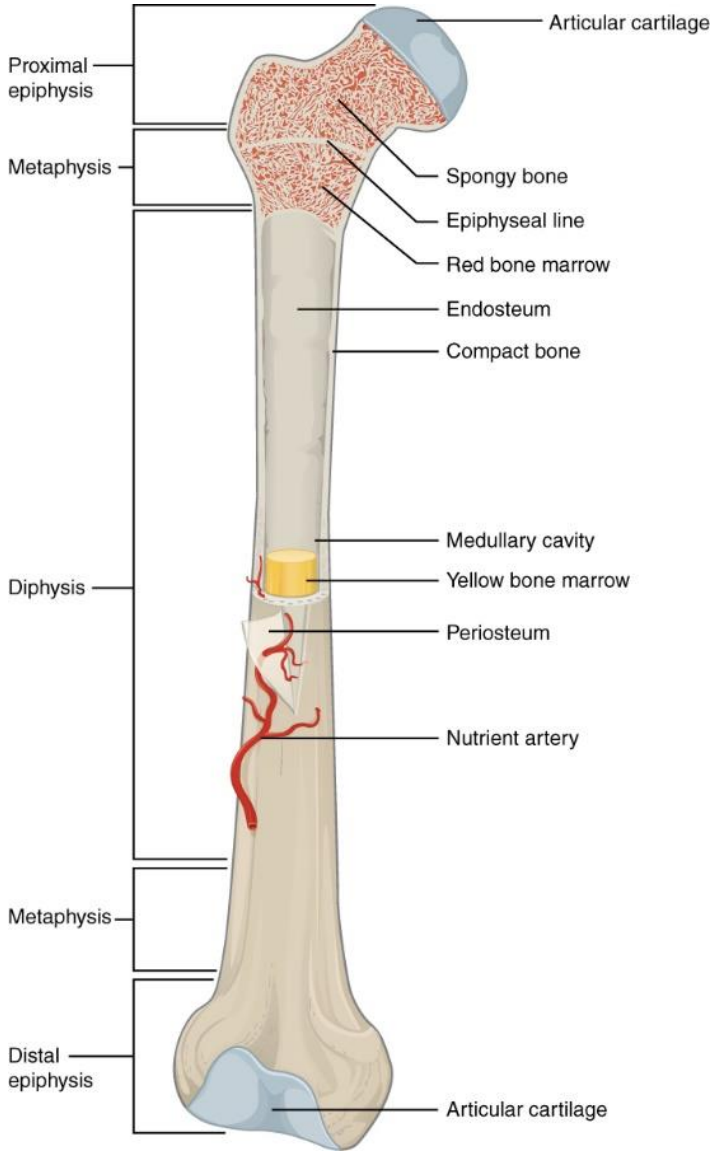

Figure 2.1 Components of a long bone along its longitudinal axis (Source: http://cnx.org/content/col11496/1.6/).

At the macroscopic level, bone can be classified as trabecular bone and compact or cortical bone (Ashman and Rho, 1988). As shown in Figure 2.2, trabecular bone consists of a sponge-like network of delicate bar-like structures which are branched and interconnected to each other. This sponge-like network gives the trabecular bone its alternate name as spongy or cancellous bone. On the other hand, cortical bone which forms the thick-walled tube of long bone contains no spaces or discontinuities visible to the naked eye. Cortical bone has a greater density than trabecular or cancellous bone.

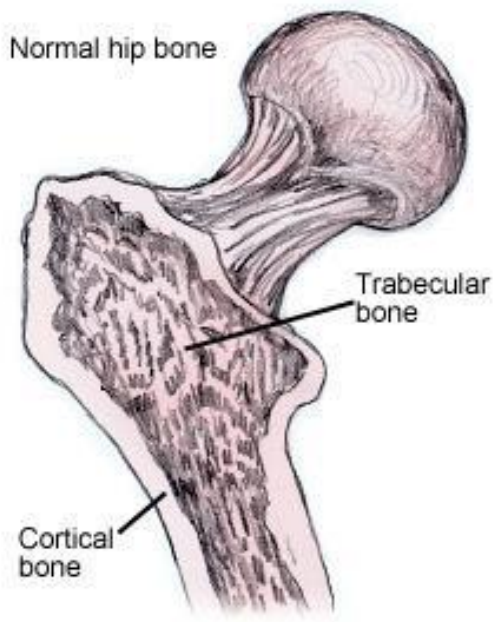

Figure 2.2 Bone at the macroscopic length scale distinguished as Trabecular bone and Cortical Bone (Benjamin McVay Petre, 2013).

The cross section of the bone can be further divided into various components as shown in Figure 2.3. Periosteum is a connective tissue which covers the surface of bone and is the location which consists of muscles. Haversian canal system surrounded by cement lines often referred to osteons are the major components of the cortical bone which extend along the longitudinal axis of the bone. Haversian canals are about 50μm in diameter. Cement lines are described in the later part of the literature. Osteocytes are bone cells formed in the osteons which evolve due to the evolution and remodeling of the bone. These osteocytes are located in the gaps called lacunae located in the osteons. Lamellae are concentric thin layer or membrane like structures surrounding the haversian canals. Osteocytes further develop into features like canaliculi as shown in the Figure 2.3. Volkmann's canals are the horizontal canals which contain blood vessels and nerves from the periosteum.

The previous work of Currey et al., 1969 suggests that bone density, a measure of the bone mineral content, and mechanical properties such as strength and stiffness are correlated. X-ray methods were used to determine the bone mineral content in the living animals. Nevertheless, the study couldn't determine the role played by collagen alone and collagen mineral composite to a great detail. However, subsequent studies answered this question. However, bone's properties are also affected by the morphology. Due to the hierarchical structure, often compared to fiber

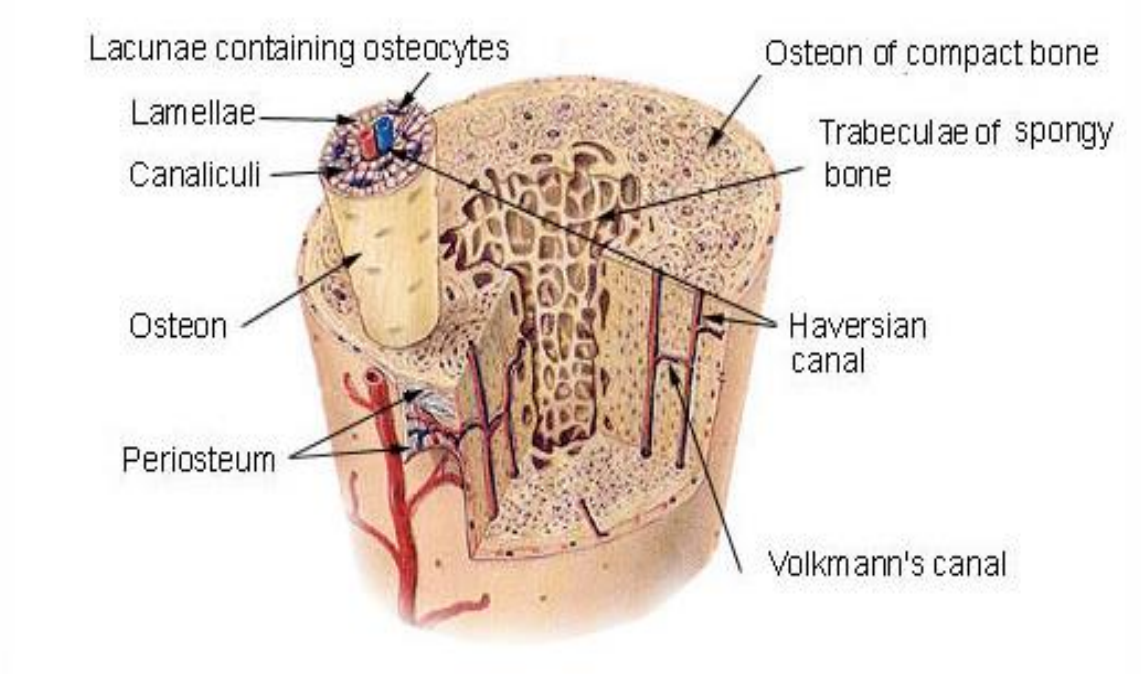

Figure 2.3 Cross section of the bone showing the trabecular bone and compact bone further classified into bone cells (osteocytes), haversian canal, volkmann's canal, lamellae, canaliculi, periosteum and lacunae. (Source: https://training.seer.cancer.gov/anatomy/skeletal/tissue.html).

reinforced materials, as a consequence bone exhibits a pronounced anisotropy. This might lead to a reduced strength values in the transverse direction. For a long bone like femur, the strong direction is said to be aligned with the femoral shaft direction. The circumferential and radial directions are said to be relatively weaker though they are functionally adequate (Fyhrie et al., 2015). Thus, for a femur, a loading direction along its long axis is preferable.

Bone structure reveals the presence of several structural mechanisms at the microscopic scale. Osteons inclusive of the haversian canal system are found amidst the interstitial lamellae

matrix in the cortical bone region. Cement lines surround the osteonal structures and separate them from the interstitial region (Burr et al., 1988). The cement lines have a lower shear strength when compared to osteons. Yet, they control fracture and fatigue by absorbing the mechanical energy. The energy absorption stops the crack propagation and provides viscous damping in the cortical region.

At the nanometer length scale, cross linked mineralized collagen fibrils interposed with mineral platelets are present (Hang et al., 2011). Atomic Force Microscopy in conjunction with Scanning Electron Microscopy are advanced methods used to examine and determine the mechanical properties of individual mineralized collagen fibrils.

Four major models have been proposed, which arrange the different features of bone at different length scales. Gupta (2010) described bone as a material which is divided into seven levels of hierarchy from collagen molecules at the nanoscale to the whole bone at the macro scale. Analogously, Weiner and Warner (1998) used a seven-level hierarchical model to describe bone. This one extends from the whole bone at centimeter length scale to unstained and unmineralised collagen at the nanometer length scale. Ritchie (2011) proposed a seven-level hierarchical model like that of Weiner and Warner (1998), though with a slight variation of the ranges of the length scales at each level. On the other hand, Fritsch and Hellmich (2007) proposed a model with five levels of hierarchy. This one extends from crosslinked collagen matrix at the nanometer length

scale to the extracellular lamellae at the microscopic length scale. Each of these models are discussed in detail as follows.

Comprehensively, Gupta (2010) described bone as a seven-level hierarchical material. Type I collagen molecules with extended platelets of carbonated apatite and a fraction of non-collagenous proteins are considered at the nanometer length scale. The fibrils form the arrays of collagen composite which eventually lead to the formation of primary and secondary osteonal structures. However, the study suggests the presence of lamellae at the microscopic length scale. The lamellae are considered as the building blocks of the osteons which are at the mesoscopic length scale. Furthermore, lamellae are considered to have a diameter around 5μm. Finally, at the macroscopic level, there exists the whole bone which extends from few millimeters to centimeters on the length scale.

A similar model with seven hierarchical levels of bone was proposed by Weiner and Warner (1998). Figure 2.4, is adopted from this paper, "The Material Bone: Structure-Mechanical Function Relations, 1998" and shows various levels considered for that study. Level 7 corresponds to the whole bovine bone, up to 10 cm on the length scale, level 6 shows a micrograph of a fractured section through a human femur which is 5500 years old. Level 5 parallels the osteons and the subsequent level 4 corresponds to the fibril array patterns. Level 3, as described in the study

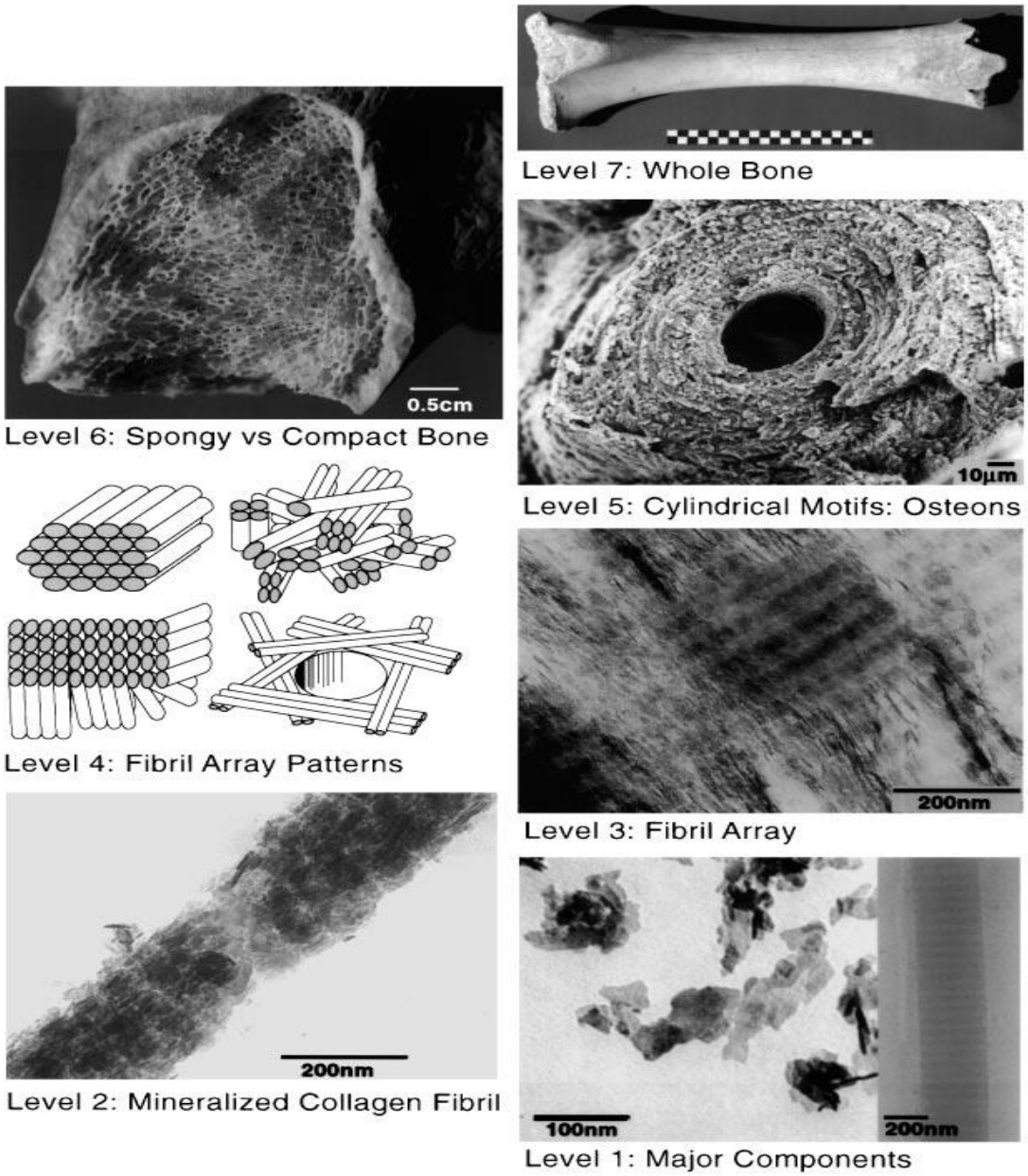

Figure 2.4 Weiner and Wagner seven level hierarchical model of bone structure (Weiner & Wagner,1998).

corresponds to fibril array, level 2 to mineralized collagen fibril and level 1 to isolated crystals from human bone and unmineralized and unstained collagen from turkey bone (tendon).

On a similar ground as Weiner & Warner (1998), a seven-level hierarchical model was proposed by another study as well (Ritchie,2011). Figure 2.5 shows Ritchie's seven level hierarchical model and the corresponding toughening mechanisms at each level. Bone was characterized as a Bone tissue at the macro level, length scale of 50cm, followed by osteons and haversian canals at around 100 nm, fiber patterns at 50nm, fibril arrays at a length of 10nm, mineralized collagen fibrils at around 1mm, triple helical collagen at around 300 nm and finally amino acids at a length scale of 1 nm. The classification plays an important role in the mechanical testing of specimens as well. The study also gives an account of the toughening mechanisms at different levels. Micro cracking, crack deflection or crack bridging are the toughening mechanisms exhibited by bone (Zimmermann et al., 2011). Microcracking is an intrinsic toughening mechanism. It diffuses or distributes the applied force over a large area by creating smaller cracks. This crack formation increases the fracture resistance of the material (Vashishth et al., 2000, Fergal et al., 2005). Crack deflection is an extrinsic toughening mechanism. It deflects the crack orientation, there by generating resistance to crack propagation in the orientation which supports large crack growth (Mohsin et al., 2006, Zimmermann et al., 2011). Crack deflection and twisting at the location of osteons, uncracked ligament bridging, bridging of the collagen – fibril,

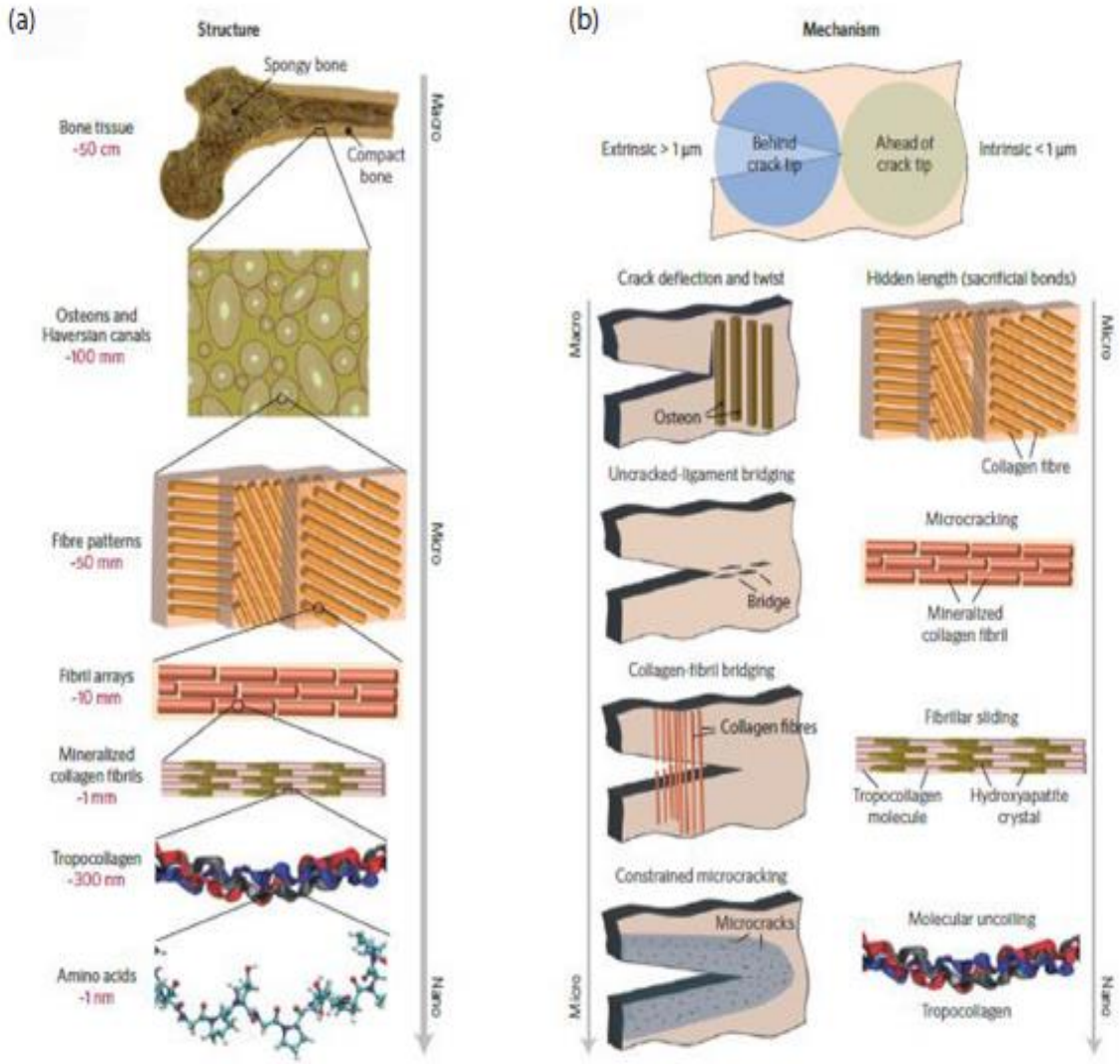

Figure 2.5 (a) Ritchie's seven levels of hierarchical model and (b) corresponding toughening mechanisms at each level.

constrained micro cracking and occurrence of sacrificial bonds were the various toughening mechanisms observed from the macro level to the micro level. Similarly, micro cracking of the mineralized collagen fibrils, fibrillar sliding of tropocollagen molecules and hydroxyapatite crystals and molecular uncoiling of tropocollagen were described as the different toughening mechanisms observed from micro scale to nano scale.

Fritsch and Hellmich (2007) represented bone as a hierarchical material too, but with a difference in the model and representations. Five levels of bone were considered for the study of homogenization of material properties in this study. Level one, around 10nm, contains the crosslinked collagen matrix corresponding to wet collagen, followed by the next level, 100-500nm on the length scale, which consists of a matrix with two phases, the collagen-hydroxyapatite network or the fibril phase. Level three, extending over a length scale of 100-500nm, is the extrafibrillar space or the hydroxyapatite foam, corresponding to a matrix, with the hydroxyapatite material formulated as circular inclusions in an ellipsoidal representative volume element. Level four, at a length scale of 5-10μm, is the extracellular bone matrix or the ultrastructure with the mineralized collagen fibrils oriented in a particular direction in order to show the anisotropic nature corresponding to the material properties exhibited by bone. Final level, level 5 consists of the extravascular bone material which is an agglomeration of extracellular bone matrix and lacunae at a length scale of around 100μm as shown in Figure 2.6.

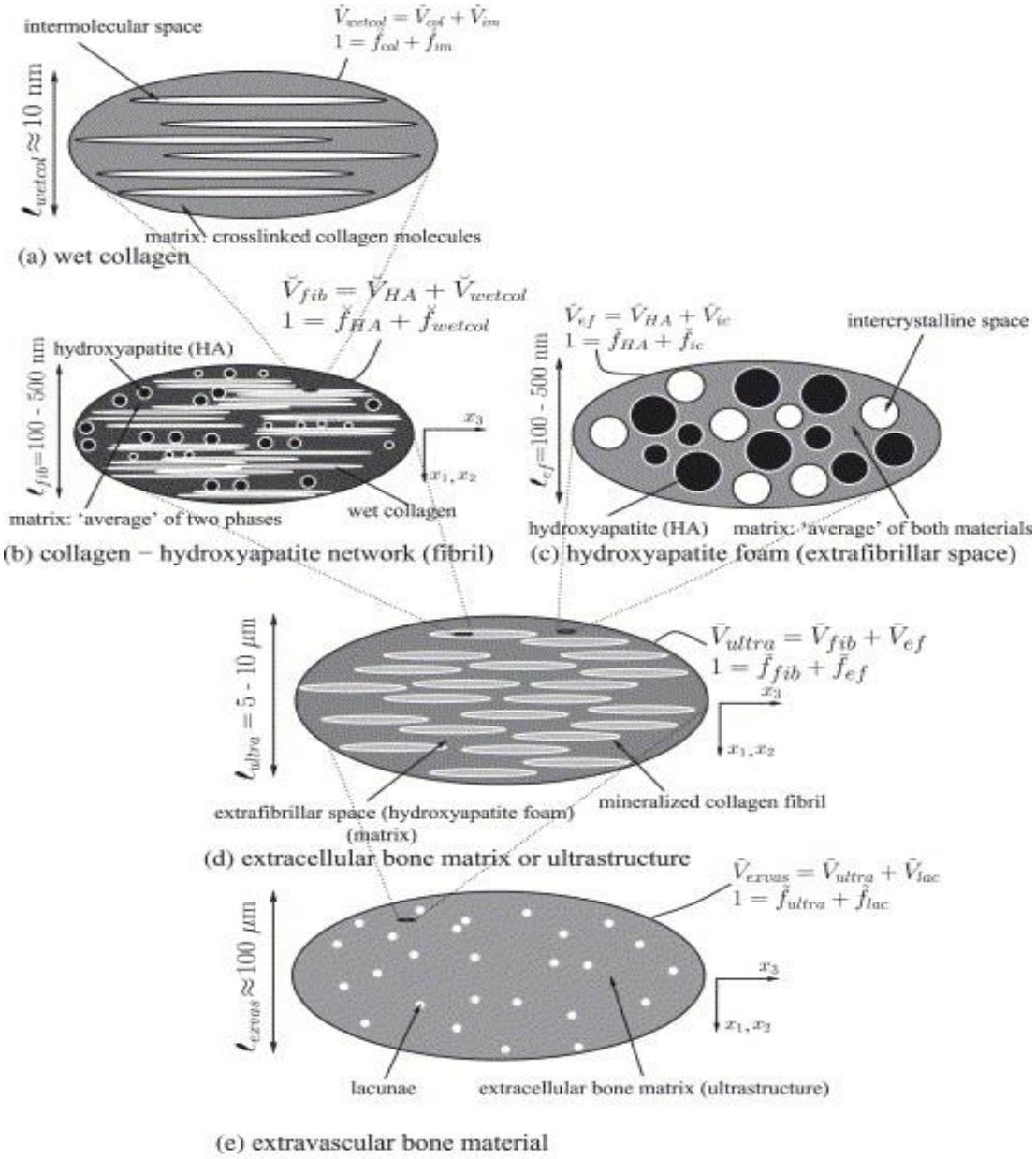

Figure 2.6 Schematic Representation of the Bone Material as a hierarchical material made up of five levels (Fritsch & Hellmich, 2007).

Thus, several studies over the last few decades provided a deep understanding of the bone histology. An extensive account on the hierarchy of bone material is available for researchers who take up the study of bone. A clear understanding of the bone histology is essential to determine the various factors influencing the mechanical properties of bone at various length scales.

2.2 Mechanical Testing of Cortical Bone

From section 2.1, we understand that bone is composed of cancellous and cortical regions. Cancellous bone is highly porous, while the cortical bone is denser. Thus, there exists a gradient of porosity in this dynamically changing and adopting bone structure. The changes in the bone microstructure can occur primarily due to aging, disease which effects the bone mass and density or due to the continual physiological loading (Tang and Vashishth, 2011; Akkus et al., 2003).

Aging leads to an increase in the risk of bone fracture (Zimmermann et al., 2011). This can be attributed to the reduction in the bone mineral density (Hui et al., 1988). Bone mineral density quantifies the bone mass which aids the identification of the bones with a high risk of fracture (Marshall et al., 1996). However, bone mineral density alone doesn't completely quantify the age-related increase in the risk of bone fracture. Changes at the microscopic and nanoscopic length scales also contribute to the deterioration of resistance of bone to fracture. Increase in the osteon density, increase in osteon size (McCalden et al., 1993; Evans and Charles, 1976) increase in the

nonenzymatic cross link densities, increase in the porosity and finally an increase in the microdamage because of cyclic loading (Frost, 1987; Burr et al., 1985; Carter & Hayes; 1977; Martin & Burr, 1982; Mori & Burr, 1993) leads to an increase in the risk of bone fracture. An increase in the osteon density with age is due to the remodeling of osteons. Remodeling of osteons effect the intrinsic repair and rehabilitation of the microdamage which the bone underwent due to in vivo cyclic loading (Schaffler et al., 1995). Table 2.1, shows a summary of the above-mentioned age related changes that the bone undergoes, which eventually lead to a reduction in its mechanical properties.

Table 2.1 Changes in the properties of cortical bone because of aging.

Number	Reference	Property	Change with age
1	McCalden et al., 1993; Evans, 1976	Osteon Density	Increase
2	McCalden et al., 1993; Evans, 1976	Osteon Size	Decrease
3	McCalden et al., 1993	Porosity	Increase
4	Sell & Monnier, 1989; Wang et al, 2002	Crosslinks	Increase
5	Schaffler, 1995	Microdamage	Increase

Aging was observed to cause a reduction in the strength properties when determined using a three-point bending test of unnotched specimens (Zimmermann et al., 2011). A 5% loss in the yield strength and 10% loss in peak strength with age were reported. Corresponding fracture

toughness properties, when determined using the R-curve measurements showed a decrease in toughness with age. The toughness reported exhibited a decrease by four folds with age. At the micrometer length scale, using Environmental Scanning Electron Microscopy and X-ray computed tomography, it was observed that smaller and fewer uncracked ligament bridges were found in the aged specimens. Uncracked ligament bridges that occur between the microcracks are an extrinsic toughening mechanism which carries the load which would otherwise be used for crack growth. At the sub micrometer length scale, small angle X-ray scattering and wide-angle X-ray diffraction were conducted. Mineralized collagen fibers showed an increase in the strain by 25% in aged specimens when compared to that of young specimens for a given strain. Thus, fibrils grew stiffer with age. Furthermore, a higher amount of collagen crosslinking was observed in the aged specimens. When considering length scales between micrometer to near-millimeter range, extrinsic toughening mechanisms such as crack bridging and deflection were observed. A decrease in the size and frequency of these mechanisms with age were reported. Secondary osteons which are primarily responsible for these toughening mechanisms were reported to increase with age. This increase in osteon density is thought to cause a decrease in the size and number of crack bridges in the aged specimens. Thus, a reduction in bone strength with a loss in plasticity and peak strength and a corresponding decrease in fracture toughness was observed with age. The study further concludes that the cortical bone derives its strength and toughness from energy dissipation

mechanisms. Aging is considered to affect these mechanisms, leading to a reduction in strength, ductility (plasticity) and intrinsic toughness.

Diseases which effect the bone mass and density also play an important role in the reduction of strength and toughness of cortical bone. Bone, a complex hierarchical material, is known for the intrinsic self-repair and removal of the microdamage as a result of in vivo cyclic loading (Ager et al., 2006; Frost, 1960; Burr et al., 1990; Gupta, 2010; McCalden et al., 1993). Pathological conditions effect these intrinsic mechanisms leading to a bone which is highly susceptible to failure even when subjected to low loads. Bone mass density experiences a reduction due to such condition. This marks the occurrence of stress fractures even when subjected to low impact loads due to the inability of the bone to absorb the energy resulting from these interactions. In osteoporosis, a similar phenomenon is observed. Reduction in the bone mass, increase in the porosity, rate of repair slower than the rate of damage thus eventually leading to a catastrophic failure of bone when subjected to low loads as well were reported (Devas, 1993; Forwood and Parker, 1991; Frost, 1985; Parfitt, 1993; Schaffler et al., 1989).

As described earlier in this section, besides aging and disease, physiological loading condition is one of the major parameters which leads to changes in the bone microstructure. Several researchers performed three-point bending tests (Phelps et al, 2000; Martin & Burr, 1985; Piekarski, 1970). Also, fracture properties of the specimen were studied using not only notched

specimens, but also un notched specimens (Evans 1973). Furthermore, the bone specimens tested so far have been distinctively in three main orientations, axial, tangential or radial (Emmanuelle et al., 2014; Reilly and Burstein, 1975). Figure 2.7 shows the three orientations along which the cortical bone is tested. However, in this study, axial was referred to the longitudinal specimens and tangential was referred to the transverse specimens. The longitudinal specimens with the force direction perpendicular to the longitudinal direction of bone have osteons surrounding the haversian canals running along the longitudinal direction. The transverse specimens have the direction of force applied on to them in a direction parallel to the longitudinal axis of bone. Haversian canals and other channels run parallel to this direction. As discussed earlier in section 1.2, several tests such as three-point bending tests, uniaxial tensile and compressive tests were conducted on bone specimens. Figure 2.8 shows a schematic of a three-point bending test conducted on a femoral bone specimen. These tests measure the elastic modulus of bone specimens and Table 2.2 is a summary of the same. Besides the macroscopic tests which determine the mechanical properties of cortical bone specimens as listed in Table 2.2, tests were conducted to determine the fracture

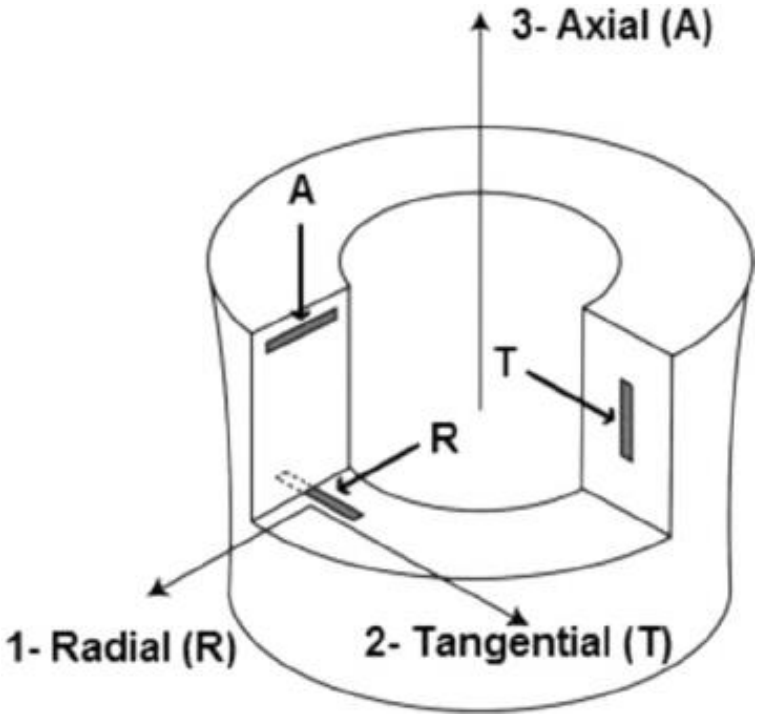

Figure 2.7 Schematic showing the different orientations to study the anisotropy of bone (Emmanuelle et al., 2014).

toughness as well. The fracture toughness of the specimens was measured in terms of the stress intensity factor K_c. Notched and unnotched specimens were tested and the K_c value was determined. Furthermore, compact tension tests and sandwich tests were reported in the literature (Pope and Outeater, 1972).

Table 2.2 Summary of the testing methods and the average young's modulus reported by various researchers.

Reference	Testing Method	Bone Type	Orientation	Young's modulus (GPa)
Stefan et al. (2010)	Three-point bending test	Human femur	NR*	17.85
Stefan et al. (2010)	Three-point bending test	Bovine tibiae	NR*	22.35
Yan et al. (2007)	Three-point bending test	Bovine femur	Transverse	17.5
Yan et al. (2007)	Three-point bending test	Bovine femur	Longitudinal	12.1
Rho et al. (1997)	Tensile Testing	Human Tibiae	NR*	10.4±3.5
Hodgskinson and Curey (1992)	Microhardness	Bovine Femur	NR*	15
Reilly and Burstein (1975)	Uniaxial tension and compression	Bovine femur	Transverse	12
Reilly and Burstein (1975)	Uniaxial tension and compression	Bovine femur	Radial	10
Townsend et al. (1975)	Inelastic Buckling	Human Tibia	NR*	11.38

* NR – Not reported

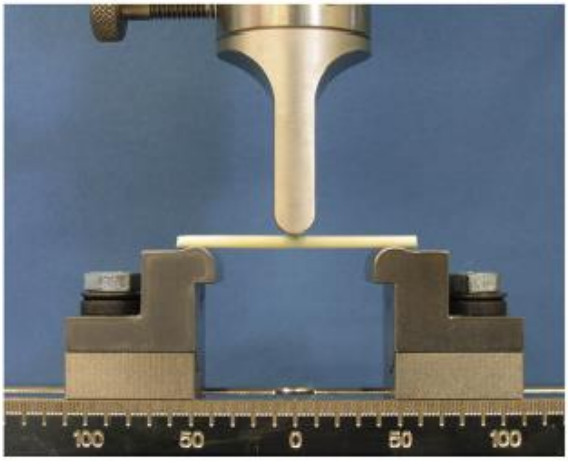

Figure 2.8 Schematic of three-point bending test on bovine tibiae (S. Unger et al., 2010).

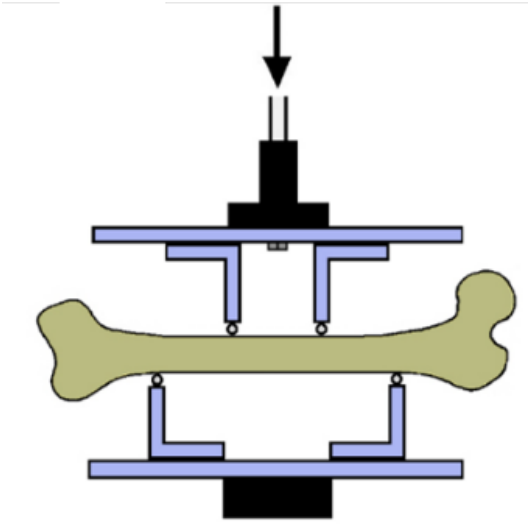

Figure 2.9 Four-point bending on bone specimen (Edsberg et al., 2000).

Table 2.3 Summary of the fracture toughness values as obtained by a plethora of studies on bone specimens.

Reference	Testing Method	Bone Source	Fracture Direction	Fracture Toughness (MPa $m^{1/2}$)
Melvin and Evans (1973)	Single-edge notched beam	Bovine Femur	Longitudinal	3.21±0.43
Melvin and Evans (1973)	Single-edge notched beam	Bovine Femur	Transverse	5.58±0.52
Behiri and Bonfield (1980)	Compact Tension	Bovine Tibia	Longitudinal	2.8-6.3
Norman et al. (1992)	Compact Tension	Bovine Tibia	Transverse	4.93-12.64
Vashisth et al (1992)	Compact Tension	Human Tibia	Longitudinal	1.6-2.5
Wang et al (1998)	Compact Sandwich	Baboon femur	Longitudinal	2.25±0.18
Ziuopus and currey (1998)	Single-edge notched beam	Human femur	Longitudinal	6.4
Wang et al (2002)	Single-edge notched beam	Human Femur	Transverse	5.09±0.98
De Santis et al (2000)	Chevron-notched short rod	Bovine Femur	Longitudinal	4.8±0.5
Yan et al (2006)	Chevron-notched beam	Human femur	Transverse	5.8±0.5
Yan et al (2006)	Chevron-notched beam	Manatee rib	Transverse	4.5±0.5
Nalla et al (2003)	Fatigue precracked flexure	Human humerus	Longitudinal	3.53±0.13
Nalla et al (2003)	Fatigue precracked flexure	Human humerus	Transverse	5.33±0.41

The majority of the tests mentioned so far give an account of the properties of cortical bone specimens at the macro scale. Bone, as discussed earlier is a hierarchical material and determination of the properties up to the nanoscale through the meso and micro scales is very essential. Nanoindentation technique which performs indents on relatively smaller areas helps in probing the mechanical properties of the material at the nano and micro scales (Oliver and Pharr, 1992; Gao and Wu, 1993; Page et al., 1998). Nanoindentations were performed on the cortical bone specimens to characterize their mechanical properties (Hoffler et al, 2005; Donnelly et al, 2006; Kruzic et al, 2009). Fracture properties at the microscale were determined as well using three-point bending tests and nanoindentations. The models proposed for the fracture property characterization were mainly based on the linear elastic fracture mechanics (Reilly and Burstein, 2006; Norman et al., 1995; Phelps et al., 2000). Further, bone was modelled either as a linearly elastic isotropic material, or transversely isotropic or orthotropic material (Hellmich and Ulm, 2005).

Table 2.4 Summary of elastic modulus values obtained by micro and nano scale studies on cortical bone specimens.

Reference	Testing Method	Bone Source	Orientation	Young's modulus (GPa)
Feng et al. (2012)	Nanoindentation	Porcine Femur	Longitudinal	15
Rho et al. (1997)	Nanoindentation	Human Tibia	Transverse	15±3.0
Rho et al. (1997)	Nanoindentation	Human Tibia	Longitudinal	19.6±3.5

Table 2.4 (cont.)

Rho et al. (1993)	Ultrasonic testing	Human Tibia	NR	14.8±1.4
Carnelli et al. (2011)	Nanoindentation	Bovine Tibia	NR	13.72
Hengsberger et al. (2001)	Nanoindentation	Human Femur	NR	18-20

Experimental investigations so far aimed at determining the fracture properties using a single mode fracture (Zimmerman et al, 2010). Very few researchers have shown the incidence of occurrence of mixed mode fracture in the cortical bone specimens. Later, studies showed the R-curve behavior exhibited by bone specimens (Yeni et al., 1995, Vashisth et al., 2001) and the necessity to incorporate the inelastic behavior in the study of the fracture properties of bone. Besides, the several studies conducted until date used single sized specimens. Having the knowledge of size effects on the measured properties, there is a need for adopting new experimental methodologies, which capture not only the inelastic behavior but also the size effects. The micro scratch test, newly introduced into the field of experimental fracture mechanics is one such method which caters to the needs.

2.3 Chapter Summary

This chapter gives an account on the several studies carried out on bone at various hierarchical levels. Several experimental methodologies were adopted to understand the mechanical properties and their behavior with age, disease and physiological loading conditions. Nanoindentation

technique was adopted to determine the elastic modulus and hardness at the nanoscale. Tests like the three-point bending test on notched specimens were conducted on the cortical bone samples to determine strength and toughness parameters. Microstructure was examined using advanced imaging techniques.

Thus, from the literature, we see that even though there are several experimental techniques at different length scales, there is a gap of knowledge at the microscale. The reason is, most of the experiments are carried out at the macro scale and they do not address the local behavior of the material at the lower length scales such as microscale. Thus, there is a need for a rigorous framework to be adopted to determine the properties at the microscale. In order to address this, a novel experimental technique was implemented to determine the fracture properties of cortical bone at the mesoscale and macroscale levels.

CHAPTER 3

INSTRUMENTED IMAGING TECHNIQUES

As an initial step of scientific study, it is essential to understand the structure and form of the specimens used for the study. Microscopy techniques play a very important role in this regard. Especially, the importance of microscopy is deeply felt in the investigation of biological materials, whose features are in general at very small length scales. This calls for an advanced surface and sub surface investigation of the cortical bone specimens.

3.1 Optical Microscopy

Optical Microscopy, one of the oldest forms of imaging techniques, enables us to magnify the images of small specimens whose features are invisible to the naked eye. This technique uses visible light and a series of lens to magnify the images. A typical optical microscope consists of a very simple schematic as shown in Figure 3.1. The advancements made in the optical microscopy techniques use the charge coupled devices (CCDs) instead of the eye piece shown in the figure. These CCDs capture the image of the specimens and display the micrograph on the screen.

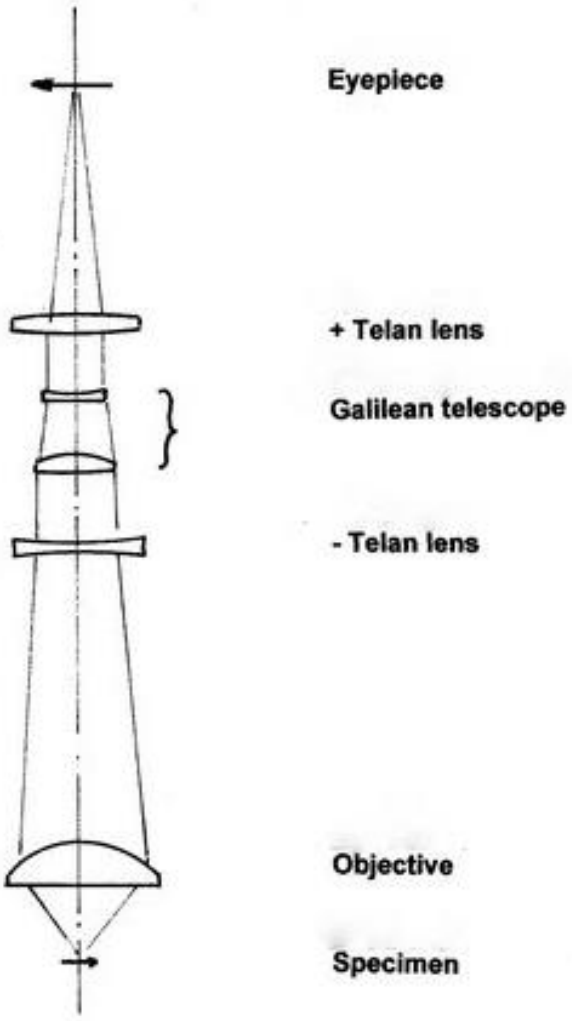

Figure 3.1 Schematic of the working of optical microscope (Source: http://www.microscopy.uk.org.uk/mag/artjun12 /fs-optovar.html).

At the Sustainability and Nanomechanics Laboratory at the University of Illinois at Urbana Champaign, having access to the Nikon Video Optical Microscope manufactured by Anton Paar

(Anton Paar USA Inc., Ashland, VA), several optical microscopy images of the cortical bone samples were captured. The optical microscope enables imaging at four levels of magnification namely, 5x, 20x, 50x and 100x. The Figures 3.2 and 3.3 show the optical microscopy images of longitudinal and transverse Cortical Bone Specimens, orientations as described in the chapter 2.

The Figure 3.2 shows the features of the longitudinal bovine cortical bone at the mesoscopic length scale. Interstitial matrix, osteons, cement lines surrounding the osteons, haversian canals and lacunae. Also, the optical microscope images show us a proof of the extensive polishing procedure adopted to obtain smooth and flat surfaces for the experimental investigation. The Figure 3.3 shows the features of the transverse bovine cortical bone at the length scale similar to that shown in Figure 3.2.

As a comparison between the two sets of figures, we observe that the osteon density is higher in the case of longitudinal specimens when compared to that of the transverse cortical bone specimens. This is expected due to directionality of the features of the bone specimens and the orientation of cutting. In Figure 3.3 (a), we can see the long dark regions which represent the canal like structures.

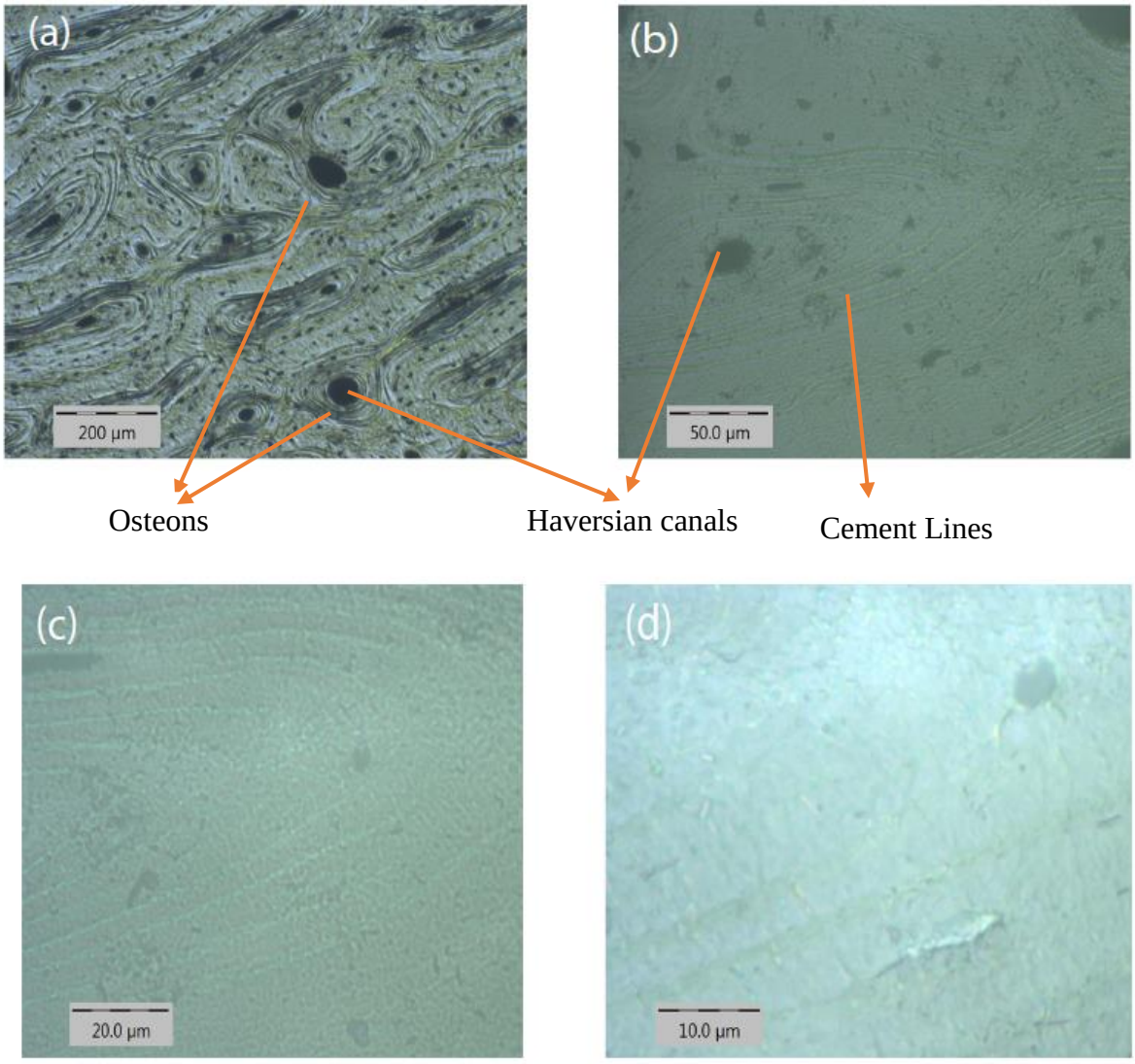

Figure 3.2 Optical Microscopy Images of Longitudinal Bovine Cortical Bone (a) Image at 5x zoom (b) Image at 20x (c) Image at 50x (d) Image at 100x.

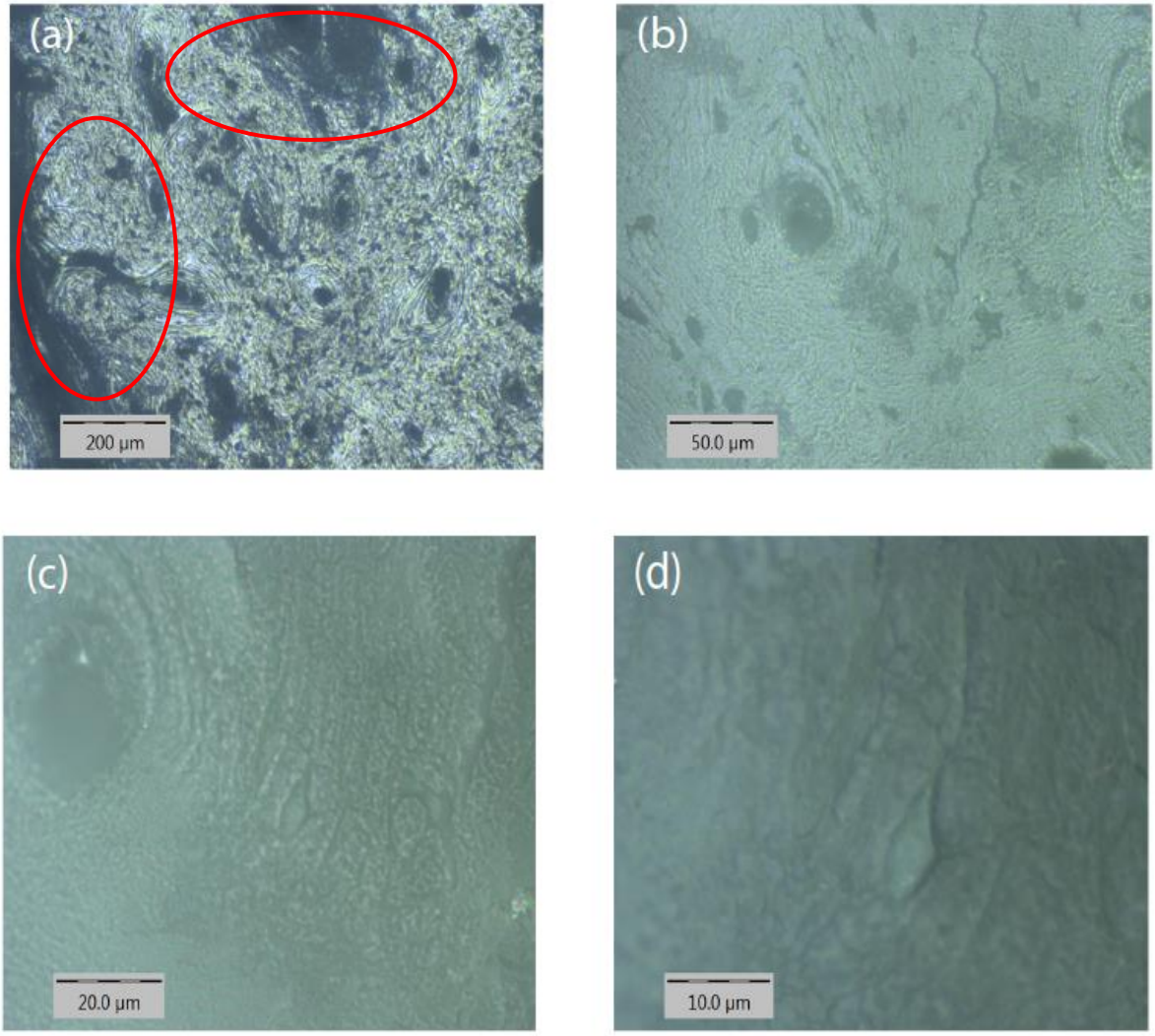

Figure 3.3 Optical Microscopy Images of Transverse Bovine (a) Image at 5x zoom showing dark regions which correspond to the canal like structures (b) Image at 20x (c) Image at 50x (d) Image at 100x.

3.2 Scanning Electron Microscopy

As mentioned at the beginning of the chapter there is a need for the surface and sub surface investigation of the specimens. Optical Microscopy images provided information only in the range of visible light. In order to probe features beyond those that are noticeable using the visible light, we need to adopt advanced technology.

Scanning Electron Microscopy with higher resolution and depth of focus is one such advancement over optical microscopy. Scanning Electron Microscopes enables us to capture images of the surface using thermionic electron beam emission. Dry and small samples whose surfaces are to be studied are placed in the vacuum, and an electron beam is then focused on to the surface. Based on the way the reflected electrons are captured, we have certain signal emission types at our disposal. Secondary Electron Emission Signal is a result of capturing electrons obtained from the surface after an inelastic scattering, thus leading to a non-conservative kinetic energy of the focused electron beam when compared before and after the beam is in interaction with the specimen surface. This is one of the most widely used signals for the Scanning Electron Microscopy Technique. Back scattered electron signals correspond to high energy electrons reflected or scattered from the surface due to elastic scattering unlike the secondary electron emission. These signals probe deeper than that of the secondary electron emissions.

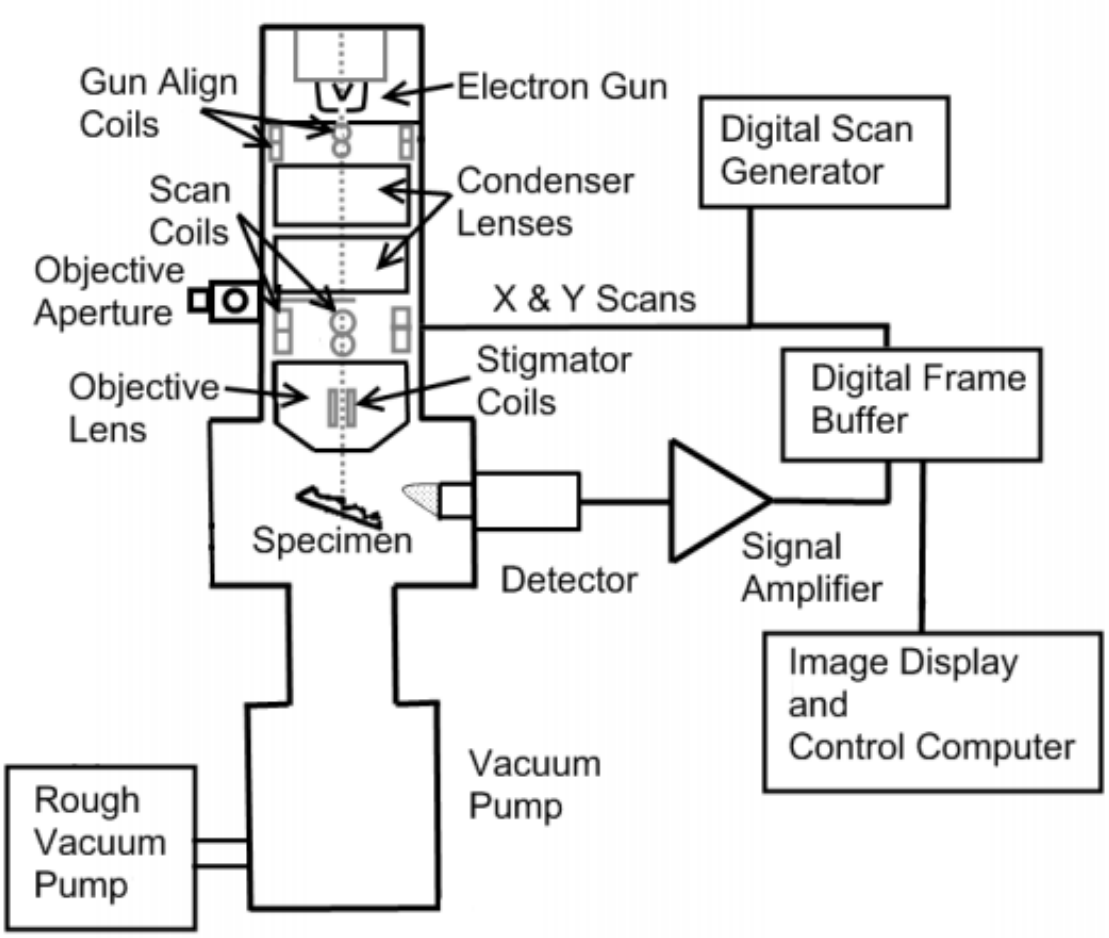

Figure 3.4 Schematic of the SEM Instrument set up (adopted from AMC Proceedings, 2016).

The Scanning Electron Microscope adopted for this study is the JEOL 6060V general purpose Scanning Electron Microscope available at the Frederick Seitz Material Research Laboratory, University of Illinois at Urbana Champaign was employed. This instrument supports an accelerating voltage up to a 30KV, both in the high and low vacuum modes employed for the

Secondary electron emission and backscattering electron emission respectively. Objective lens is a conical lens which enables a working distance from 6 to 48mm, with an aperture of 30 micron. Magnification enabled on the devices ranges from x5 to 300,000.

Figure 3.5 JEOL 6060 V Scanning Electron Microscope at Fredrick Seitz Material Research Laboratory, University of Illinois at Urbana Champaign (Source: www.jeolusa.com).

Secondary Electron Emission may not be the best method when testing biological materials as most of the materials tend to have a non-conductive surface unlike most of the metals and alloys which can be visualized with a great resolution up to several levels of magnification. Besides, the specimens used for this study are cortical bone specimens embedded in epoxy which make them

even more non-conductive due to the presence of a resin. Under the above-mentioned circumstances, it is essential to adopt the technique of Back Scattering Electron Detection.

Also, for the cortical bone specimens used in the study, there were instances of the specimen's surfaces getting charged when using secondary electron emission. This was avoided to a considerable extent when the images were being captured using backscattering technique. The Figures 3.6 to 3.8 show a comparison of the images which project the surface captured using two different electron emission signals.

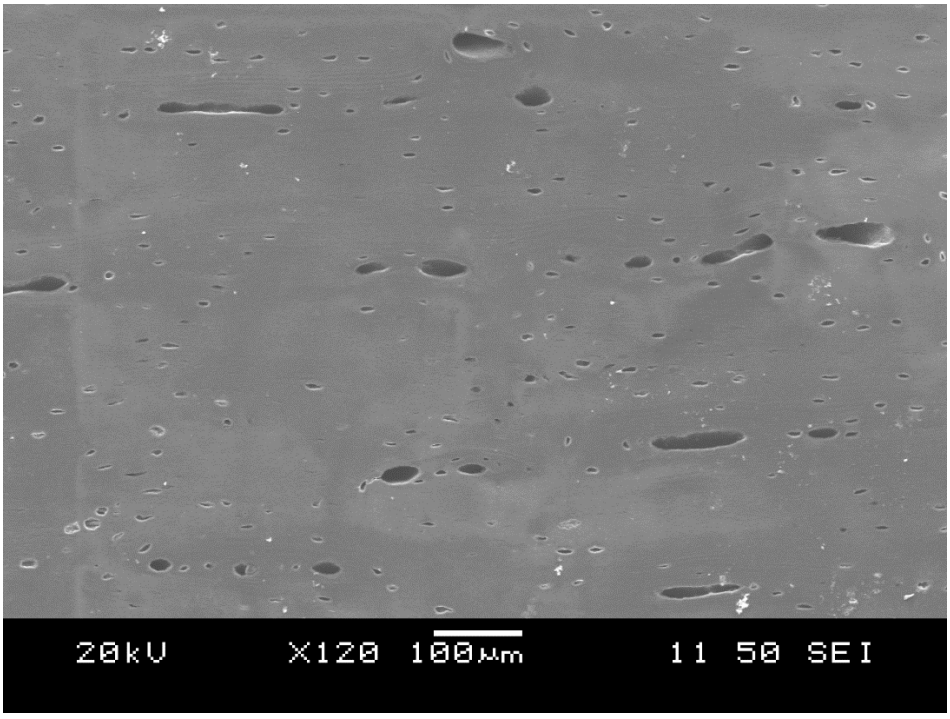

Figure 3.6 SEM image of cortical bone specimen captured using Secondary Electron Emission Signal.

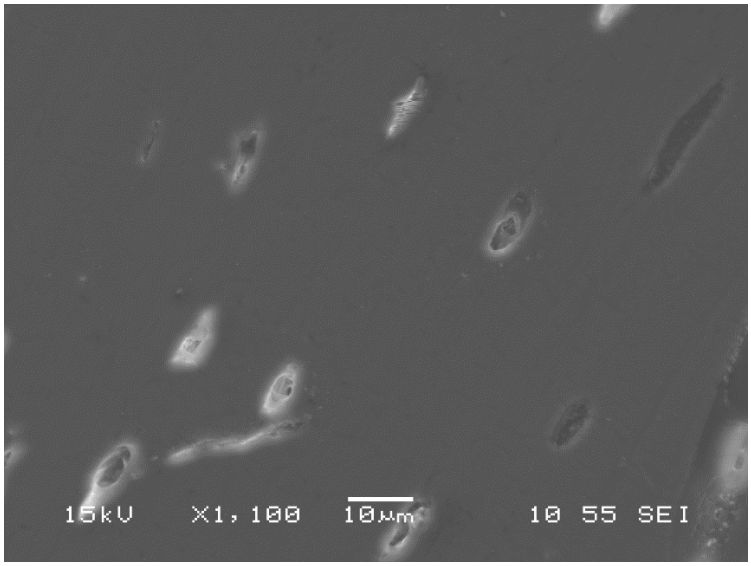

Figure 3.7 SEM image of cortical bone specimen captured using Secondary Electron Emission Signal.

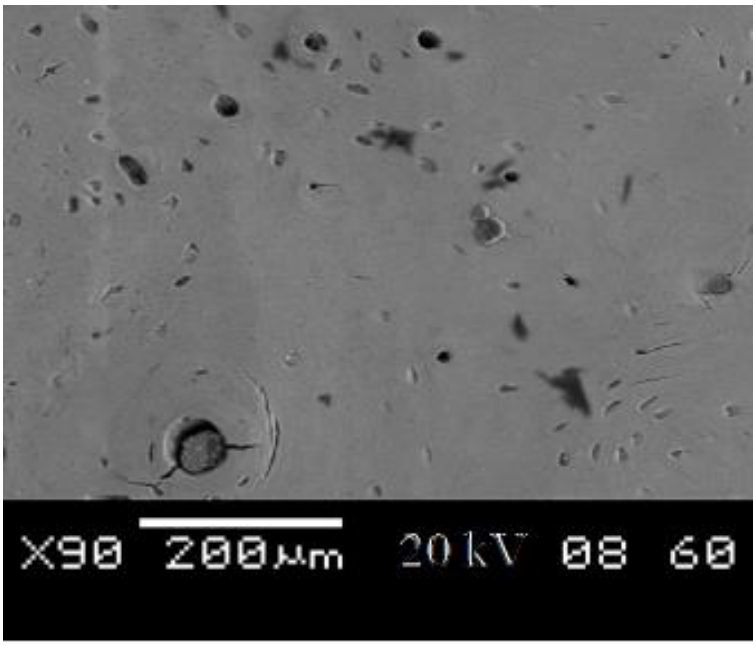

Figure 3.8 SEM image of cortical bone specimen captured using Backscattered Electron Emission.

Furthermore, several combinations of the JEOL 6060V specifications were tried for a number of times by trial and error on a significant number of cortical bone specimens which finally led to the parameters which could be efficiently used in capturing images of these non-conductive cortical bone specimens.

Firstly, the specimens were placed in the specimen holder and a copper tape is placed on the specimen and as well as on the specimen holder in order to make the specimens conductive enough to reflect the electrons.

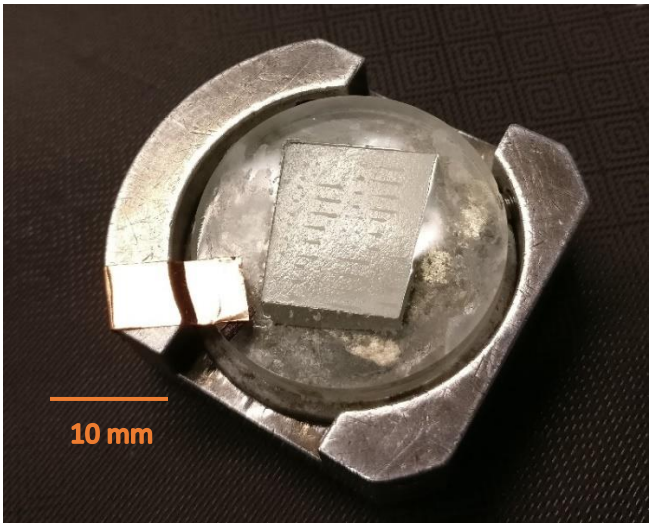

Figure 3.9 Bovine Cortical Bone specimen prepared for Scanning Electron Microscopy.

Later the specimens were placed in the vacuum chamber and the high vacuum, secondary electron emission signal was employed in order to make the initial gun alignments, aperture and stigmatism corrections at an accelerating voltage of around 15KV for several of the investigations

and a voltage of 30KV for certain studies as well. The adopted spot size for bone specimens was in the range of 50-60. This value was on the higher end and thus lead to a certain loss of resolution, but captures certain features and phenomenon well.

The working distance adopted for the study was maintained at quite low at around 10-11mm. Scanning Electron Microscopy Images shows the topology of the bone specimens at greater magnifications. The Figures 3.10 and 3.11 show different features such as osteons, cement lines, haversian canals and lacunae with greater resolution when compared to the optical microscopy images. Also, these images can be further processed for determining parameters such as osteon density.

To attain further higher resolutions of the images, the JEOL 7000F Analytical SEM, with a Schottky Field Emission Gun was tried. This is a high-resolution Scanning Electron Microscope. The cortical bone specimens used for this study could not reach the vacuum thus making it impossible to use this high-resolution microscope for the study.

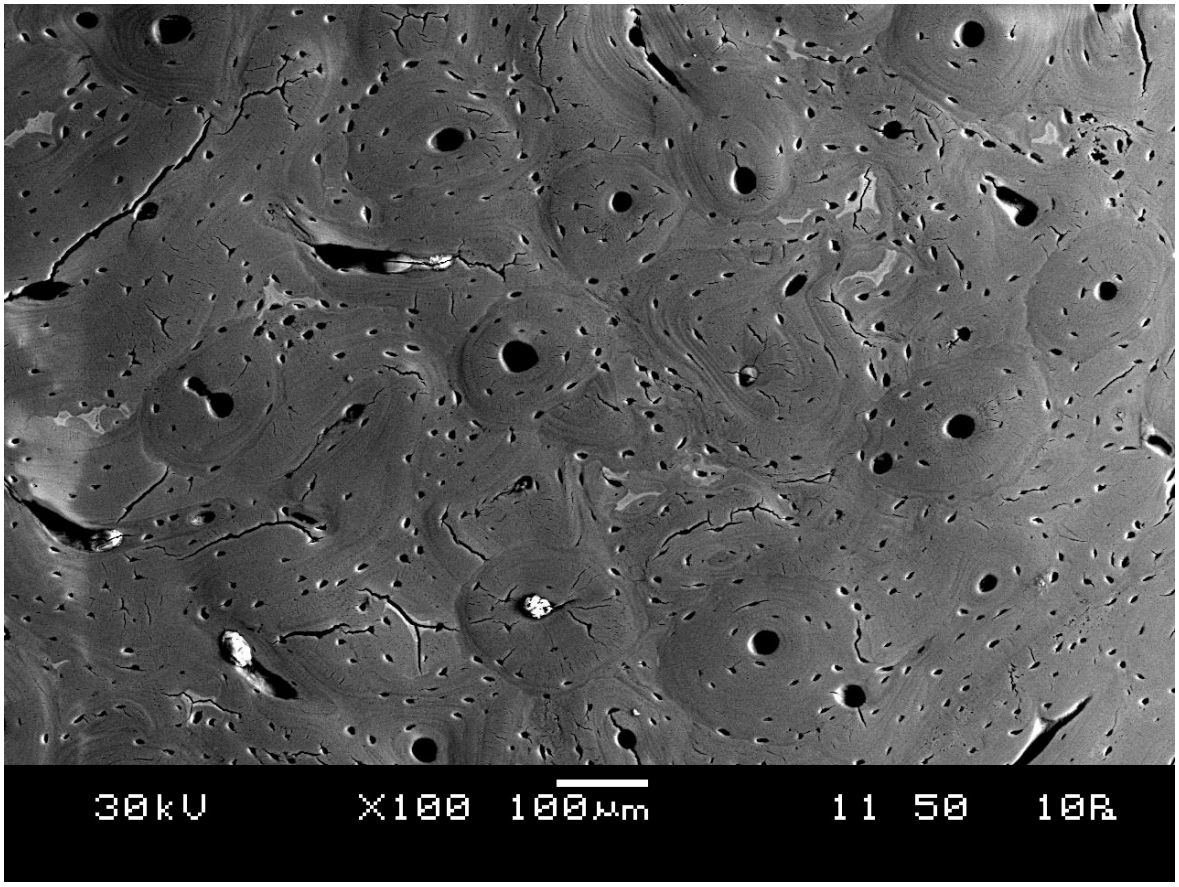

Figure 3.10 Scanning Electron Microscope Image of the Cortical Bovine Bone; The image shows the features such as cement lines, haversian canals and osteons.

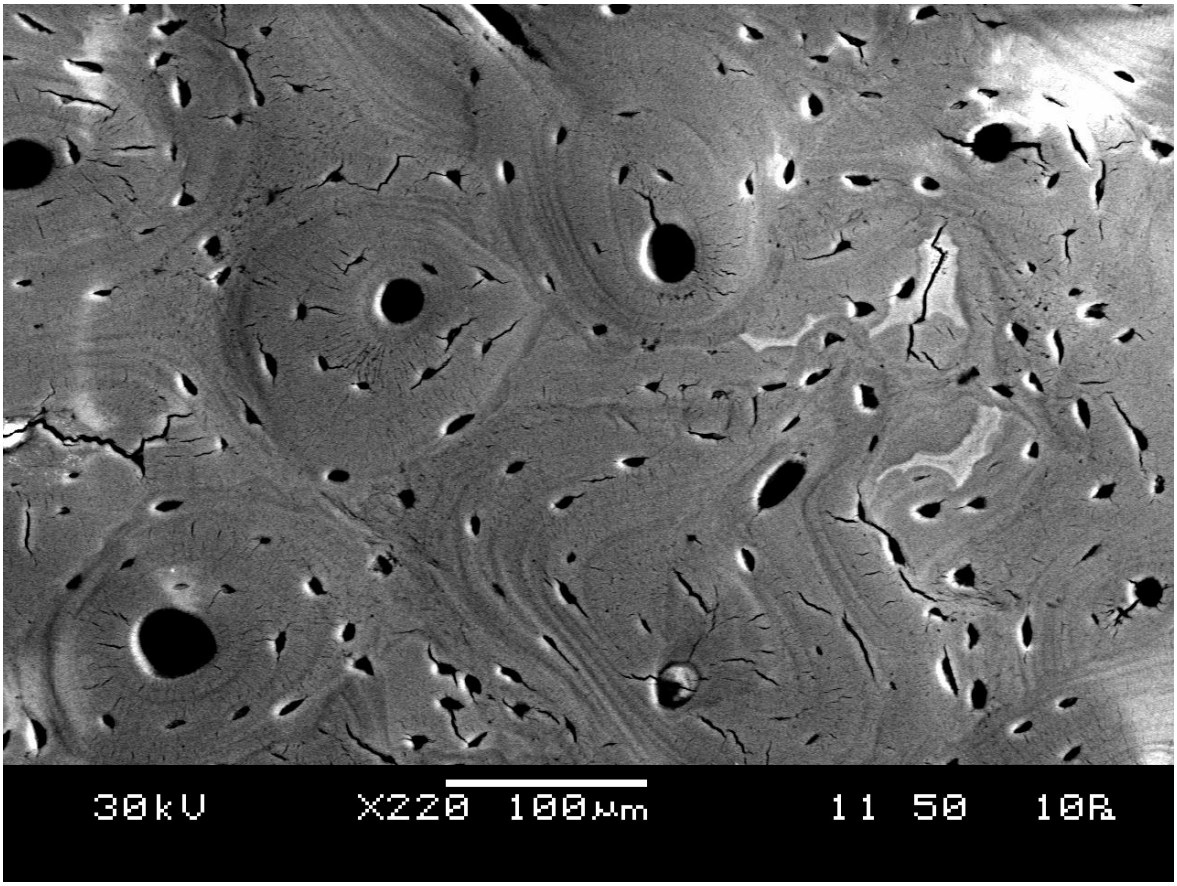

Figure 3.11 Scanning Electron Microscope Image of the Cortical Bovine Bone.

3.3 Environmental Scanning Electron Microscopy

The limitation faced while using JEOL 7000F Analytical SEM motivated the use of a high-end Field Emission Environmental Scanning Electron Microscope, Philips XL30 ESEM-FEG at the Beckman Institute, University of Illinois at Urbana Champaign. The Philips XL30 ESEM FEG is equipped with the Everhart-Thornley secondary electron detector and Robinson series 6

scintillator-type backscattered electron detector (BSD), plus solid state low and standard voltage BSDs. It also consists of Gaseous secondary electron detectors.

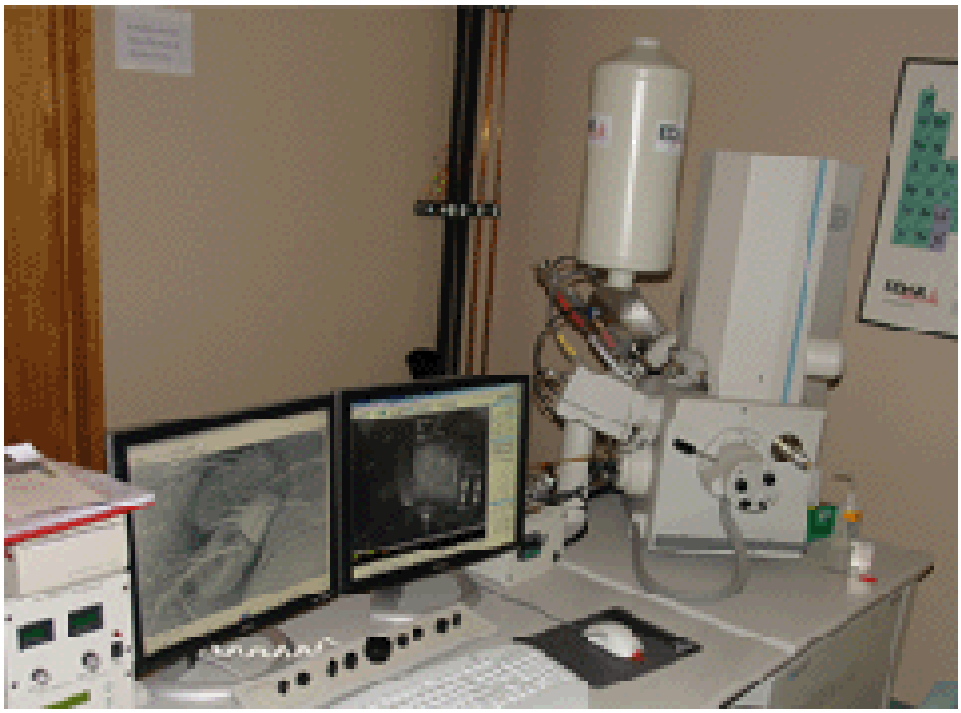

Figure 3.12 Philips XL 30 ESEM FEG, Beckman Institute, University of Illinois at Urbana Champaign (Source: www.itg.beckman.illinois.edu).

Environmental SEM is more powerful than the general purpose or the analytical SEM as ESEMs operate in the wet mode. Thus, even if the specimens aren't completely dried, there arises no concern of the specimens not reaching their vacuum. These Environmental Scanning Electron Microscopes are specifically designed for biological and other non-conductive or non-

metallic substances. Further, they do not require the specimens to be coated. The charging of the specimens is inherently avoided by the ESEMs due to wet imaging mode.

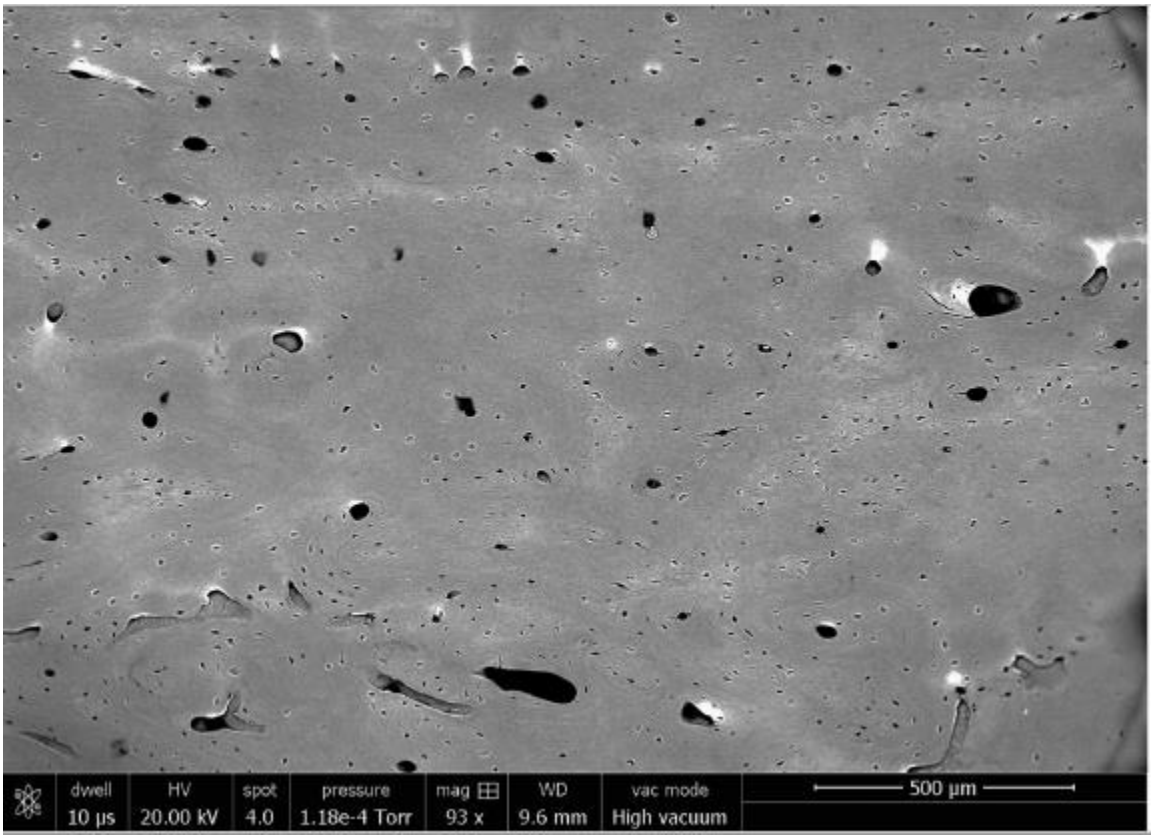

Figure 3.13 Environmental Scanning Electron Microscopy Image of Transverse Cortical Bone specimen at 93x.

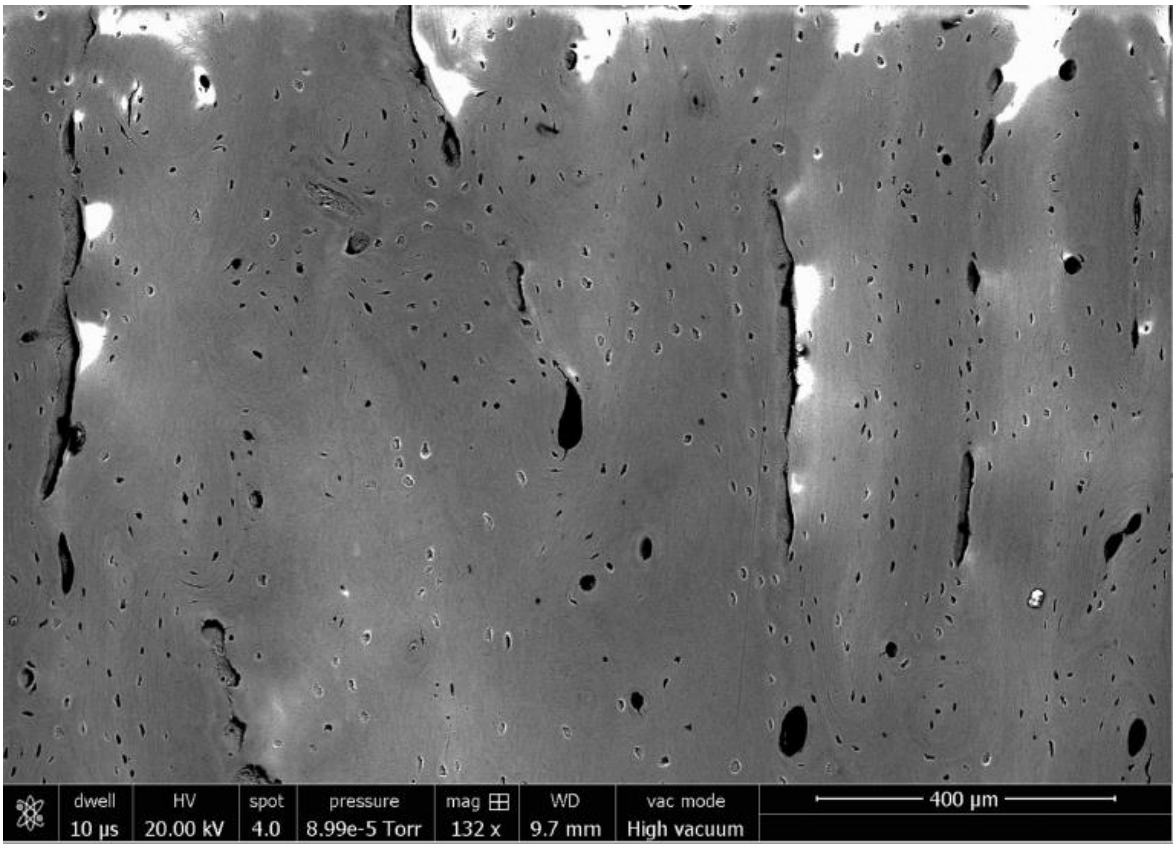

Figure 3.14 Environmental Scanning Electron Microscopy Image of Transverse Cortical bone at 132x.

3.4 Zeiss Confocal Microscopy

Besides the scanning electron microscopy, several other microscopy techniques were explored as well. Zeiss Confocal Microscopy is a product of such exploration. A confocal laser scanning microscope scans a sample sequentially point by point, or multiple points at once. The pixel information is assembled into an image. As a result, one acquire optical sections with high contrast and high resolution in x, y and z directions.

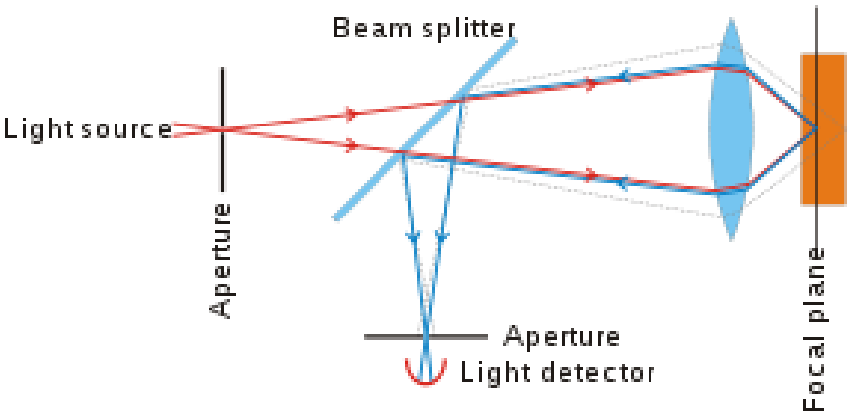

Figure 3.15 Schematic showing the principle of Confocal Microscopy (Source: www.cityofhope.org).

Figure 3.16 Zeiss Confocal Microscopy (Source: www.cityofhope.org).

The Laser Scanning Microscopy 8 family delivers supreme image quality with the highest sensitivity for quantitative imaging in life sciences and mainly for advanced topography analyses on materials surfaces. The Zeiss Confocal Microscope in the Material Research Laboratory, UIUC uses violet light as the monochromatic laser that is focused on the specimens.

The surfaces of the cortical bone specimens embedded in epoxy could not be detected to the fullest, as this instrument required the surfaces to be coated using certain coloring substances such as basic fuchsin at the time of sample preparation itself, so that sufficient light gets reflected from the surface. However, the surfaces captured using the instrument are shown here in Figure 3.16.

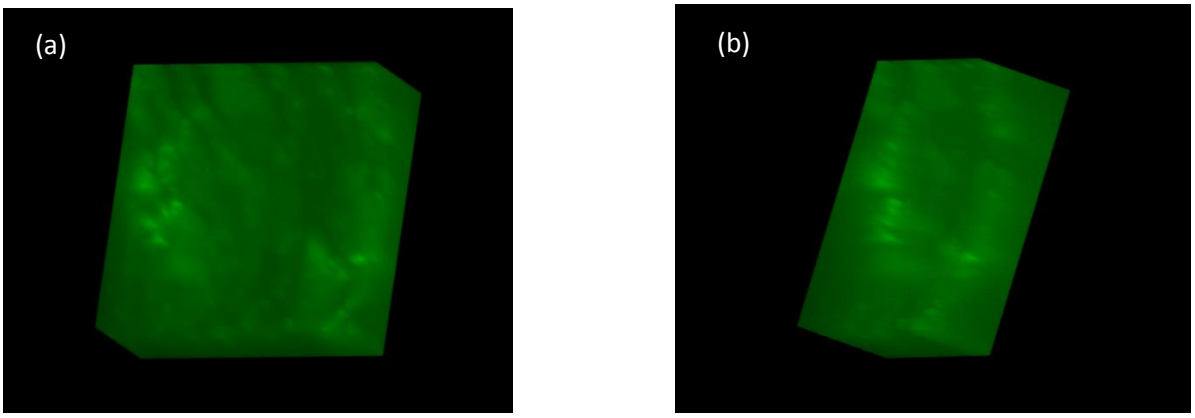

Figure 3.17 (a) and (b) represent the images of the scratch surface that were captured using ZEISS Confocal Microscope.

3.5 Near Field Scanning Optical Microscopy

Near-field scanning optical microscopy (NSOM/SNOM) is a technique for nanostructure investigation that breaks the far field resolution limit by exploiting the properties of evanescent

waves. This is done by placing the detector very close to the specimen surface. When the sample is scanned at a small distance below the aperture, the optical resolution of transmitted or reflected light which is limited only by the diameter of the aperture.

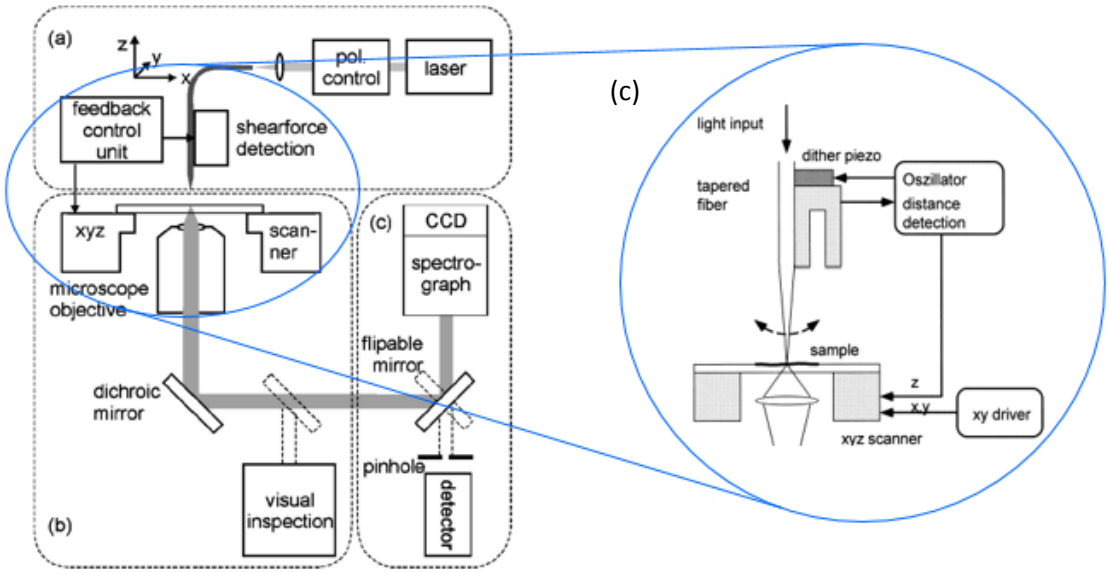

Figure 3.18 Excerpt showing the principle of the Near Field Scanning Electron Microscopy ((a) and (b) adapted from J.Chem. Phys., Vol 112, No. 18, 8 May 2000, (c) adapted from Current Opinion in Colloid & Interface Science 4(1999) 256-264).

NSOM is capable of attaining an optical resolution in the range of 60-100 nm. This allows for the surface inspection with high spatial, spectral and temporal resolving power. With this technique, the resolution of the image is limited by the size of the detector aperture and not by the wavelength of the illuminating light. As in optical microscopy, the contrast mechanism can be easily adapted to study different properties, such as refractive index, chemical structure and local

stress. Dynamic properties can also be studied at a sub-wavelength scale using this technique. NSOM/SNOM is thus a form of scanning probe microscopy.

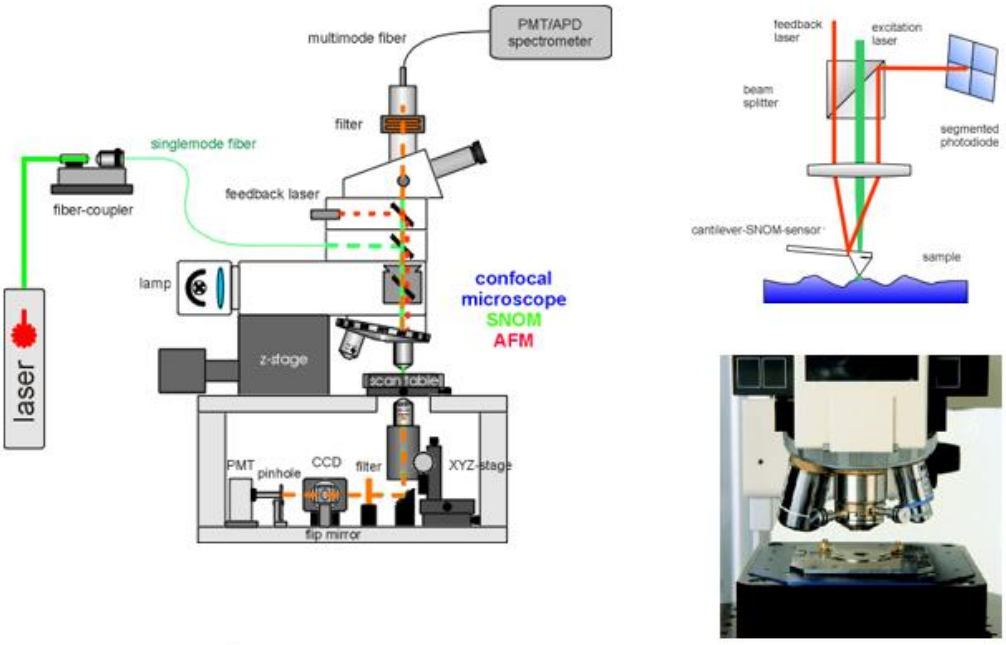

Figure 3.19 Witec Near Field Scanning Optical Microscope, Fredrick Seitz Material Research Laboratory (Source: http://www.witec.de//snom.html).

Frederick Seitz Material Research Laboratory at the University of Illinois at Urbana Champaign has the Witec Near Field Scanning Optical Microscopy at the disposal for the users. Witec NSOM enables compositional and topographical characterization of the materials. The spatial resolution is 100 nm in the lateral direction and the spatial range is 100 x 100 μm^2.

Typical applications are found in nanotechnology research and in particular the highly relevant fields of nano-photonics and nano-optics. In life science and materials research, SNOM allows the optical detection of the most miniscule surface structures of transparent as well as opaque samples. Using combinations with fluorescence techniques, even single-molecule detection can be easily achieved.

There were certain limitations as to why this method wasn't pursued further. First, it limited the working distance to very low range and at the same time, the depth of field was very shallow. Furthermore, the investigation was limited to just the surface characterization and thus deeper layers cannot be effectively probed into using this method. Later, for soft materials this is not a very ideal method, especially in the shear force mode. Last but not the least, the scan times for large sample areas are extremely long when there arises a need for high resolution imaging. Most importantly the training and using of this instrument turned out to be much more expensive when compared to using the confocal microscopes and scanning electron microscopes.

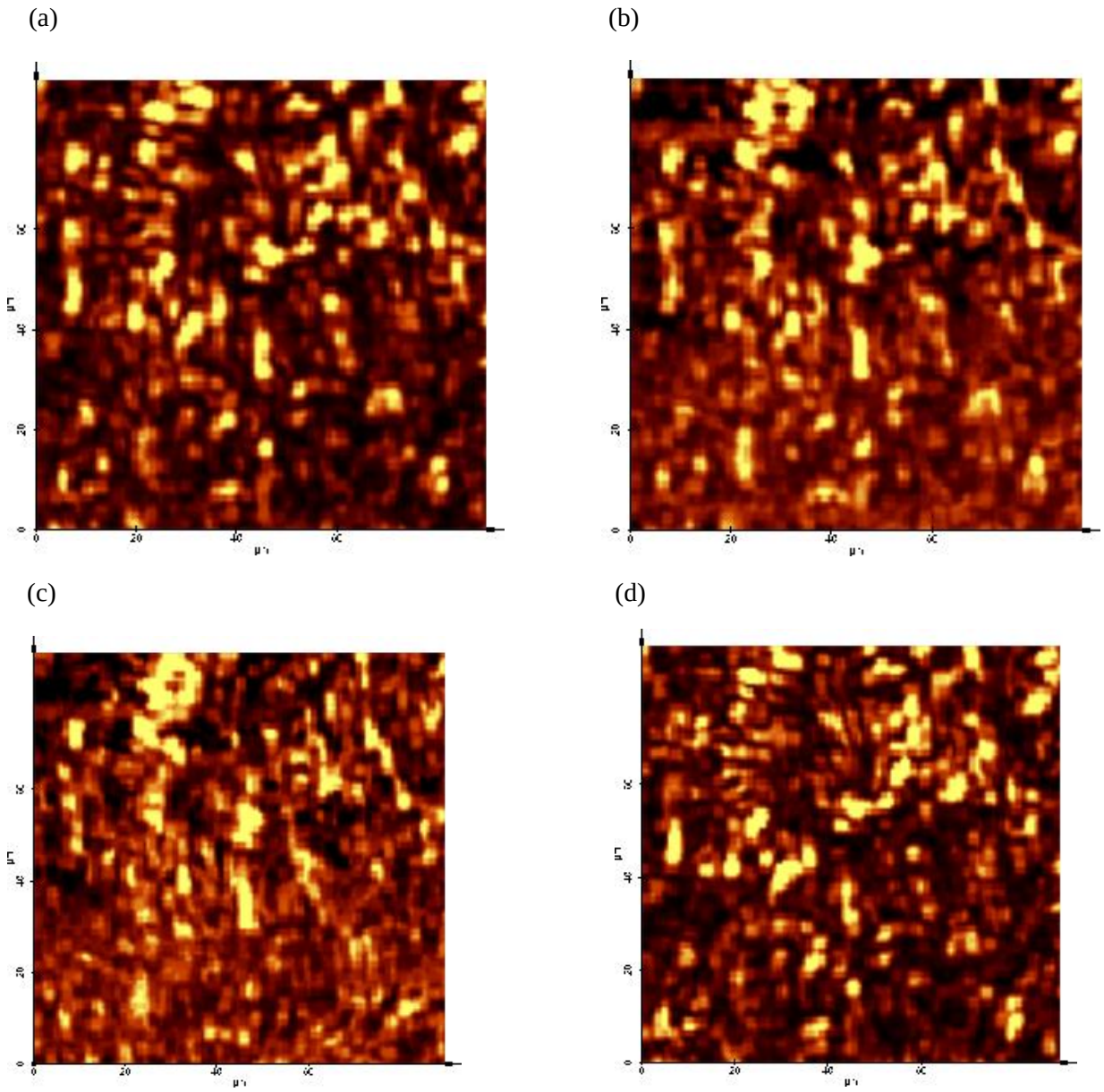

Figure 3.20 (a), (b), (c) and (d) represent the transverse cortical bone images taken using WITEC NSOM instrument available at Material Research Laboratory, UIUC.

3.6 Inverted Material Microscopy

The inverted material microscopy is carried out using the Axio Observer from Zeiss at the Frederick Seitz Material Research Laboratory at UIUC. Axio Observer combines the proven quality of Zeiss confocal microscopes with automated components. Its inverted design facilitates parallel alignment of the objective lens.

The instrument takes very little time in capturing images. There's no need to refocus, even when changing magnification or switching samples. This enables us to observe more samples in less time. Also provides for stable imaging when working with high magnifications as well. Even the specimen mounting procedure is quite simple. The specimen needs to be placed on the stage, focused once and this focus could be further used for all magnifications and samples as the instrument keeps a memory of the focus. Besides, the illumination across the entire field of view is homogeneous thus producing brilliant images.

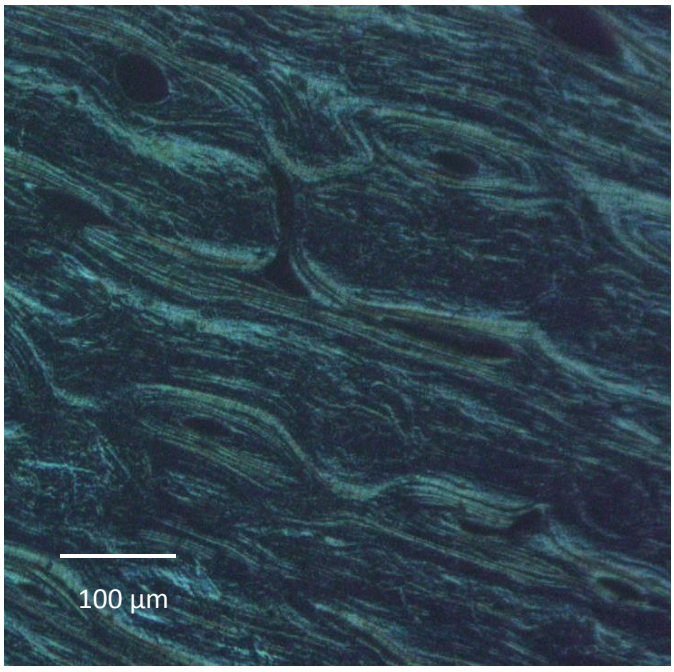

Figure 3.21 Inverted Microscopy Image of the Cortical Bone taken at 10x using white light.

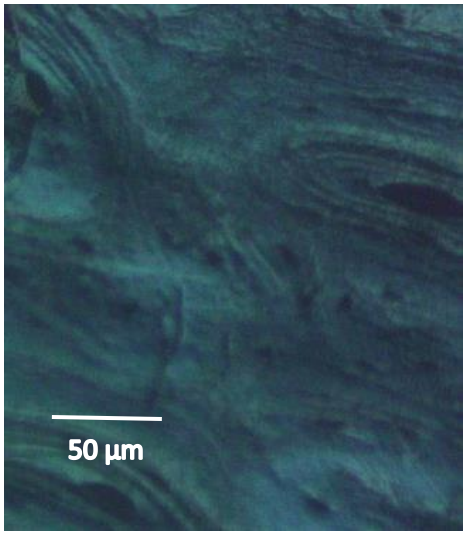

Figure 3.22 Inverted Microscopy Image of the Cortical Bone taken at 20x using white light.

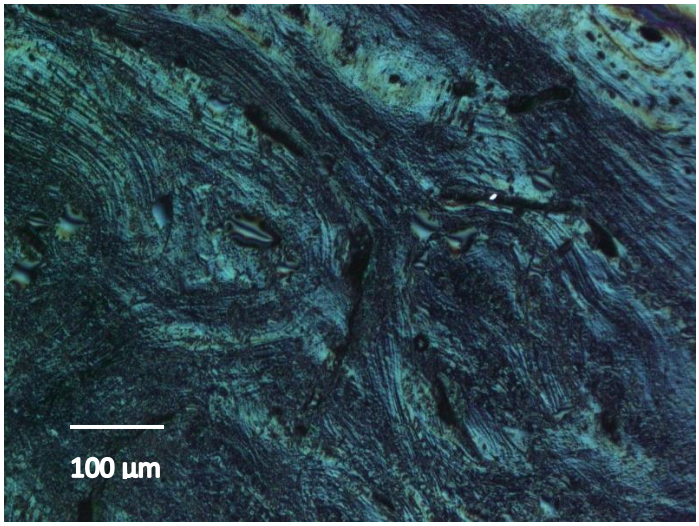

Figure 3.23 Inverted Microscopy Image of the Cortical Bone taken at 10x using yellow light.

3.7 Chapter Summary

This chapter provides a documentation of the several imaging techniques at the disposal of the research community and the several limitations that are faced during each of the methods, especially in the case of biological materials such as bone which is nonconductive. The chapter thus also shows the comparison of the several methods mentioned above and an elaborate study especially on the scanning electron microscopy which gave better images with much less effort

and effective usage of resources. Environmental Scanning Electron Microscope has an upper hand when exploring higher magnifications with a resolution that is satisfactory.

CHAPTER 4

X-RAY DIFFRACTION STUDIES

X-Ray Diffraction is a non-destructive technique used to analyze material properties like composition, structure and crystallographic orientations. It is a very versatile method which can be employed to test different states of material, solid, powder or liquid forms. X-Ray Diffraction studies are performed on the unknown material and the test data is analyzed based on the available reference database which is built up over the past decades. A major source of data is the database provided by the International Centre of Diffraction Data.

Also, the data analysis of the X-Ray Diffraction studies can be classified into the following groups. Firstly, the influence of temperature, humidity and pressure can be analyzed. Secondly, a quantitative and qualitative phase analysis can be performed. Lastly, microstructural parameters such as crystallite size, orientation effects and residual stress in the polycrystalline materials can be determined.

4.1 Principle

X-Rays are electromagnetic waves associated with wavelengths or beams of photons with their corresponding energies. Their wavelengths are in the range of 0.01 nm to 10 nm and the energies

correspond to 0.125 to 125 keV. The wavelength and energy are inversely proportional to each other.

$$E = hv = h\frac{c}{\lambda} \tag{4.1}$$

where, h is the Planck's constant, v is the frequency, c is the velocity of light and λ is the wavelength of the radiation (Moore, 2008). Since the atomic distances, wavelengths and lattice parameters are all measured in terms of the units of Angstroms ($A^o = 10^{-10}$ m), in the X-Ray Diffraction studies as well, Angstroms are the units that are generally used. X Rays with a wavelength λ and intensity I_o interact with the material and undergo phenomenon like attenuation, absorption and scattering. The transmitted Intensity are related to the incident intensity through certain coefficients which in turn depend on the crystallographic parameters.

$$I = I_o e^{-\mu d} \tag{4.2}$$

μ, the attenuation coefficient dependent upon atomic number (Z), density (ρ), packing fraction (p) and wavelength (λ).

$$\mu = p\rho Z^3 \lambda^3 \tag{4.3}$$

Also, the phenomenon of scattering which is an integral part of X-Ray Diffraction studies can be classified into mainly two types, namely Coherent and Incoherent Scattering. Coherent scattering

corresponds to the elastic scattering of the incoming photon upon collision with inner shell electrons. Since it is an elastic scattering, the wavelength remains the same and thus energy as well. Whereas, incoherent scattering corresponds to inelastic scattering of the incoming photon upon collision with the inner shell electrons. This corresponds to an increase in wavelength, and thus a decrease in the photon energy.

X-rays are generated in a sealed x-ray tube. Electrons are emitted by a hot filament, the cathode of the tube and they are accelerated due to the high voltage difference between the anode and the cathode. These accelerated electrons then interact with the target material at a high speed and result in the removal of the electrons from the inner shells of the atoms of the material. These changes in the atomistic configuration of the material lead to the emission of characteristic X-Ray radiation specific to that material and its composition (PANalytical X-Ray Diffraction documentation).

The X-Ray radiation which interacts with the crystalline system of the target material undergo interference. The interference patterns form the basis of the diffraction study. This phenomenon of interference is described using the Bragg's Law

$$n\lambda = 2d \sin\theta \tag{4.4}$$

Where, n is the order of the interference, a positive integer, d is the interplanar spacing between the atomic layers, θ is the Bragg's angle; 2θ is the angle between the incident and reflected beams and λ is the wavelength of the incident beam.

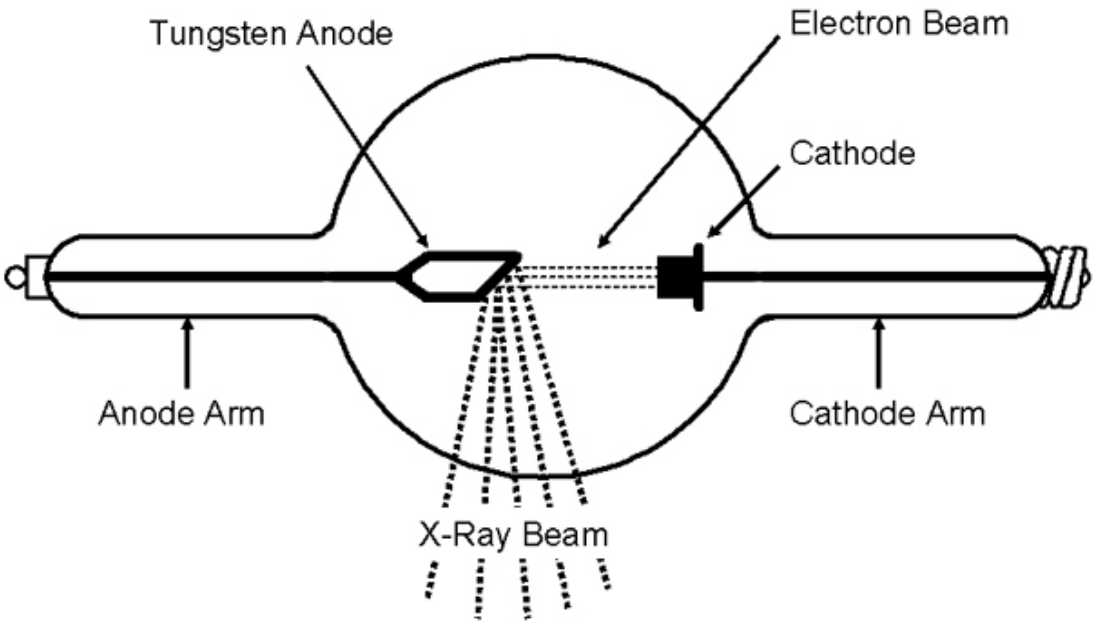

Figure 4.1 Basic schematic of the X-Ray Tube (Source:www.orau.org).

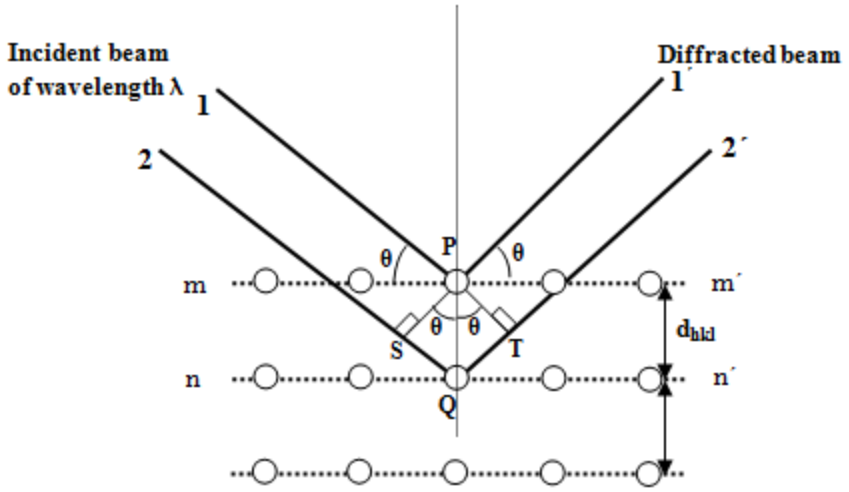

Figure 4.2 Schematic of the Bragg's Law (Source: www.nptel.ac.in).

4.1.1 Small Angle X-Ray Scattering Technique

Small angle X-ray Scattering is a special technique. In this method, instead of the atomic distances, it is the particle sizes or shapes which are measured, in order to facilitate the measurement and understanding of the structure of the particle systems. This technique helps in determining certain protein types and compositions in the target material, which can be only discovered at very small scattering angles.

4.2 Instruments

The principle of X-Ray Diffraction is used in the construction of X-Ray Diffractometer. The X-Ray tube is arranged on one end of the instrument, and the beam generated by the tube passes

through slits which regulate the beam intensity, amplitude and in turn the divergence that is directed on to the target sample. These X-rays, after interacting with the target material undergo interference, and the reflected rays are captured using a detector. This reflected beam which is received at the detector also passes through the slits in order to create convergence of the reflected X-Rays generated from the target material.

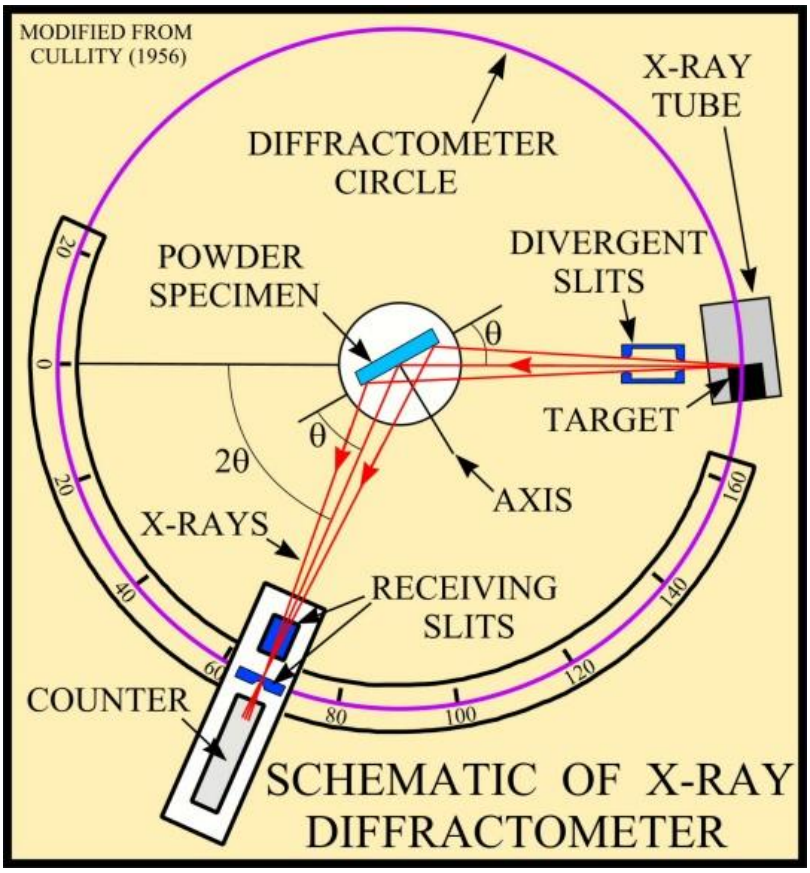

Figure 4.3 Schematic of the X-Ray Diffractometer (adopted from U. S. Geological Survey Open-File Report 01-041).

4.2.1 PANalytical / PHILIPS X'Pert MRD System #2

The Frederick Seitz Material Research Laboratory at the University of Illinois at Urbana Champaign is a hub of several X-ray diffractometers. One of the instrument used for the study was the PANalytical/Philips Xpert Material Research Diffractometer(MRD) System.

Figure 4.4 PANalytical Xpert 2 Material Research Diffrcatometer (Source: www.panalytical.com).

The PANalytical Xpert 2 MRD system uses a Cu K-alpha radiation with a wavelength of 0.15418nm. The instrument features a theta/2theta vertical four-circle system with phi, psi

rotations and enables the sample translation in the x, y and z directions. The instrument consists of a point focus beam generator. The generated beam passes through the primary optic component, namely, crossed-slit collimator with a Ni filter and a secondary optic component, x-ray lens followed by the 0.27^{o} parallel plate collimator. Collimator is a device which helps in isolating the direction which is required for the study from the other directions which behave more like a noise. The beam then hits the target material which is centered on to the mounting plate. The reflected beam after interfering with the target material passes through a flat graphite monochromator and then finally captured by proportional detector. The monochromator also a function similar to that of the collimator. It helps in removing the unnecessary wavelengths from the input signals, here from the reflected beam. The complete set up in inside a closed chamber which even enables a high temperature in situ analysis under air or vacuum (XRD Documentation, Frederick Seitz Material Research Laboratory).

4.2.2 SIEMENS/BRUKER D-5000

The Powder X-Ray Diffraction as well works with the same principles as mentioned in the sections 4.1 and 4.2. Powder X-Ray Diffraction study is one of the most common practices in the universities and research laboratories due to the ease of installation and usage involved in it.

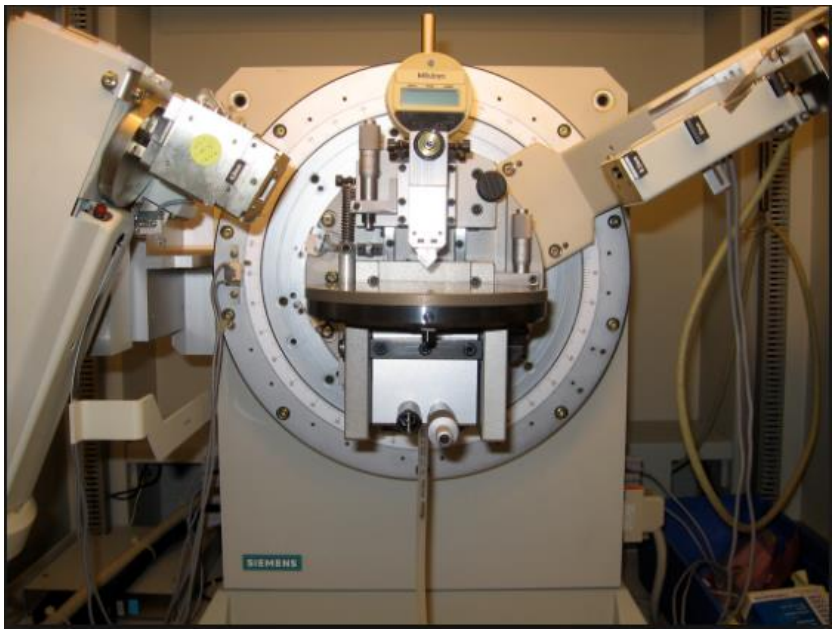

Figure 4.5 Powder X-Ray Diffractometer, SEIMENS/BRUKER D-5000.

Siemens/Bruker D-5000 Powder X-Ray Diffraction instrument uses the Cu K-alpha radiation with a corresponding wavelength of 0.15418 nm. The instrument consists of a Bragg Brentano Configuration of the theta/theta vertical goniometer system. It also encompasses the optical spinner (phi) rotation. The X-Ray generated from the X-Ray tube passes through the soller slit and divergence slit like that mentioned in the PANalytical Xpert 2 set up. This beam now interacts with the target material and it undergoes interference. The reflected passes through a complex system which consists of scatter slit, receiving slit, detector slit, a curve graphite monochromator and finally scintillation detector. This instrument is effective in the determination of amorphous

phase contents in the mixtures (Powder XRD Documentation, Frederick Seitz Material Research Laboratory).

4.3 Specimen Preparation

The cortical bone specimens used for the X-Ray Diffraction study are exclusively prepared based on the specimen requirements of each instrument to achieve the most desirable results.

4.3.1 PANalytical Xpert 2 MRD Specimens:

Porcine femurs were obtained from Meat Science Laboratory of University of Illinois at Urbana Champaign. Bones were obtained from 22-26 weeks old swine which were harvested for a duration of 24 hours after slaughter. The animals were corn fed and weighed about 275 pounds. The femurs thus obtained were kept frozen at -20^{o}C temperature in order to keep them fresh until the specimen preparation procedure commenced. Femurs stored at -20^{o}C were thawed and sections were cut from the mid-diaphysis region using a Table Top Diamond Band Saw. The trabecular bone region containing the tissue was then removed using a dissection kit as our interest is only in the Cortical Bone Region of the Femur. The band saw is again used to prepare specimens of smaller size, 15mm X 5 mm X 1.5mm, which are suitable to the Diffractometer System. A deeper cleaning of the specimens is done in a solution prepared using 1.5% Alconox and 5% Bleach and ultra-sonically cleaned for a duration of 20 minutes. The specimens are now kept dry at room temperature for a duration of 24 hours in order to remove the moisture from the bone samples. The PANalytical

Xpert 2 MRD System is suitable for thin film testing and bulk material testing in dry conditions. Thus, the moisture removal step is essential. This specimen is now mounted on to the specimen holder inside the PANalytical Xpert 2 MRD System using a tape on to the edges and is thus placed in the instrument as a target material.

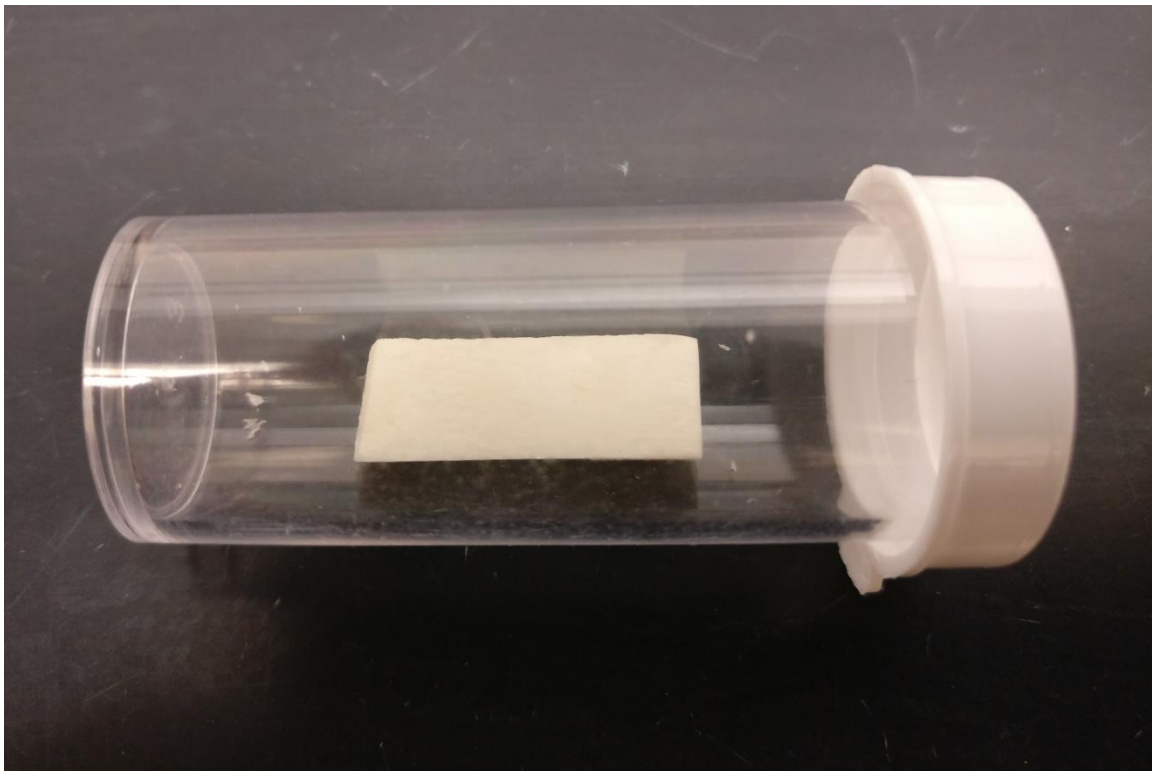

Figure 4.6 Cortical Bone Specimen prepared for the X-Ray Diffraction study on the PANalytical Xpert 2 Material Research Diffractometer System.

4.3.2 SIEMENS/BRUKER D-5000 Powder XRD Specimens

Powder X-Ray Diffractometer helps in identifying the material properties and characteristics of even amorphous materials. Materials like bone are indeed amorphous with a short range of order of atoms and broad peeks instead of sharp peaks as that of crystalline substances. For the Powder X-Ray Diffraction studies, the material is ideally made into a fine powder and arranged on the specimen holder in no particular order to ensure isotropy of the parameters measured.

On this note, cortical bone specimens were prepared into a powder form as well. The source of the swine bone specimens used for the entire study remained the same. Hence in a similar fashion as that of the specimens prepared for PANalytical Xpert 2 MRD system, the femurs which were obtained were kept frozen at -20^{o}C. The frozen femurs were then thawed and cut using Table Top Diamond Band Saw. The trabecular region was removed and a deeper cleaning was performed in a similar fashion as that mentioned in the PANalytical Xpert 2 section. Later the specimens are placed in the oven at 50^{o}C for a duration of 2-4 hours. This step is essential for the preparation of powdered bone specimens. The oven dried specimens are then ground to very fine powder using mortar and pestle. The grinding procedure takes up to 1-2 hours. This powder is then placed in the Powder X-Ray Diffraction specimen holder and then inserted onto the SIEMENS/BRUKER D-5000 as the target material.

4.4 Results

The prepared specimens were first tested using the PANalytical Xpert 2 XRD System and then the Powder X-Ray Diffractometer, SEIMENS/BRUKER D-5000. The data obtained from each is analyzed using JADE Software. The software uses the powder diffraction files database from the International Center for Diffraction Data and inorganic chemistry structure database from Fachinformationszentrum Karlsruhe (FIZ) and the National Institute of Standards and Technology (NIST). Material Data Inc., Jade plus software is used for pattern analysis, profile fitting and to search or match the profiles to the database. Crystallite/ grain size are thus obtained using this platform.

4.4.1 PANalytical Xpert 2 MRD System

Three cortical bone specimens prepared as mentioned in section 4.3.1 were tested using the PANalytical Xpert 2 MRD system. The data was obtained for a 2theta range of 10 degree to 75 degree using a slow scan mode. Slow scan was chosen as bone is a poor diffracting material, and might just give a lot of noise when a fast scan is performed. However, a fast scan mode can be chosen to get a glimpse of how the data looks qualitatively. The data thus obtained was analyzed using JADE software, as mentioned earlier.

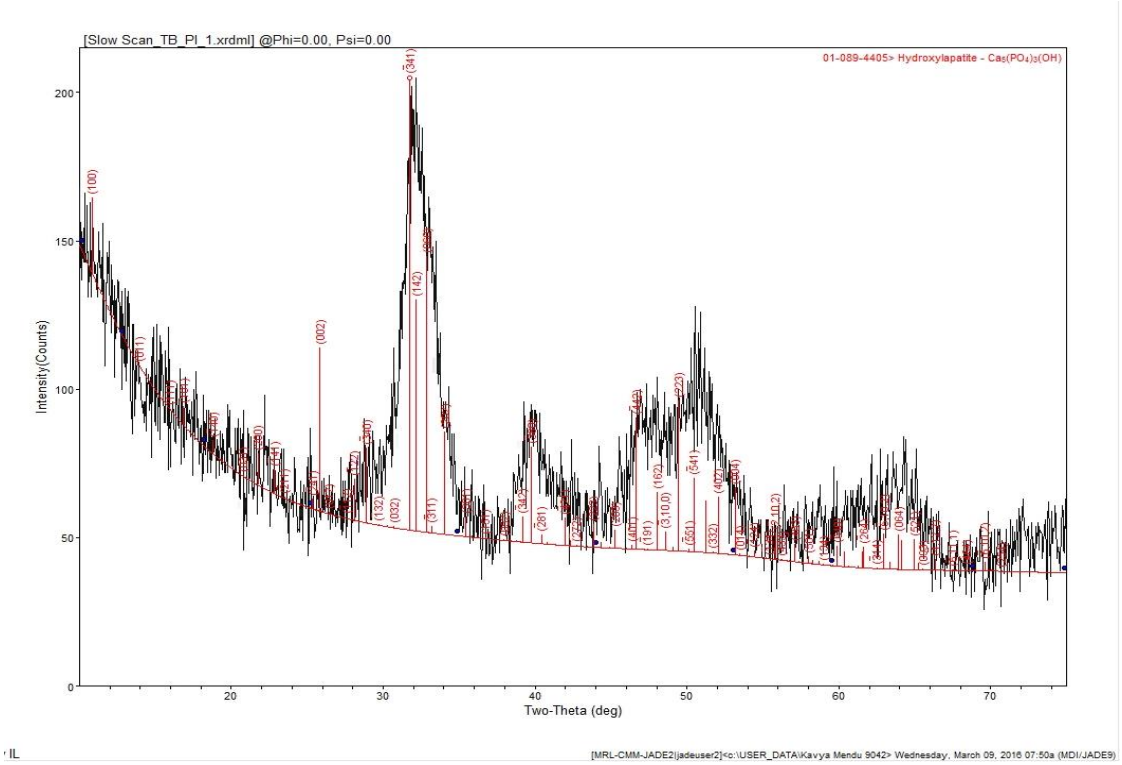

Figure 4.7 X-Ray Diffraction pattern of specimen 1 measured using PANalytical Xpert 2 MRD System and analyzed using JADE Software.

From the data, the locations of the peaks are determined and the corresponding crystallite sizes are calculated. Also, an average crystallite as well can be computed.

Table 4.1 Calculations related to the data obtained for specimen 1.

2-Theta	d(Angstrom)	Height	Area(a1)	Area %	FWHM	XS(nm)
32.316(0.036)	2.768(0.0060)	87.7(2.3)	5408.6(177.4)	100	2.408(0.080)	3(1)
40.092(0.104)	2.247(0.0112)	21.3(2.0)	1082.4(127.3)	20	2.385(0.197)	3(1)
49.065(0.577)	1.855(0.0409)	27.7(3.8)	4169.9(596.0)	77.1	7.093(0.432)	1(1)
51.069(0.199)	1.787(0.0130)	13.3(6.6)	534.3	9.9	1.886(0.405)	4(2)

XS is the crystallite size determined using the Scherer's equation. From table 4.1, the average crystallite size is 3.3nm. Similar calculations were performed for other specimens and the data along with the images are as shown below.

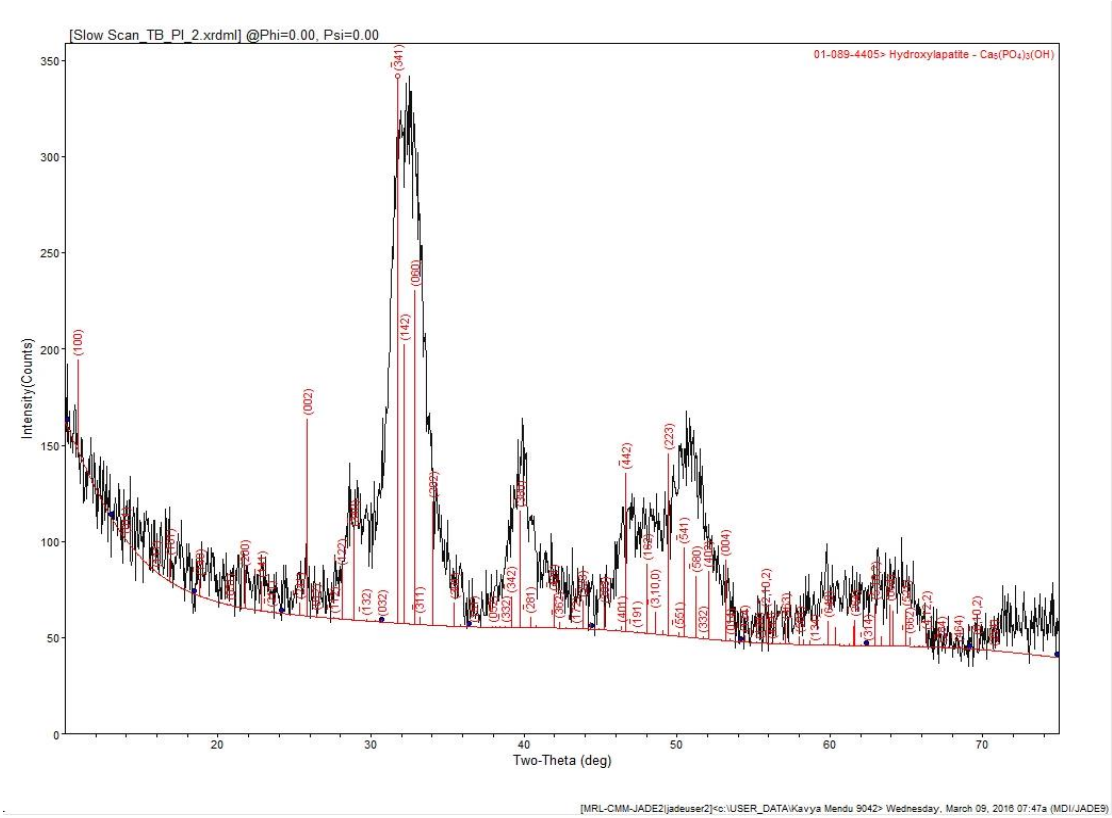

Figure 4.8 X-Ray Diffraction pattern of specimen 2 measured using PANalytical Xpert 2 MRD System and analyzed using JADE Software.

Table 4.2 Calculations related to the data obtained for specimen 2.

2-Theta	d(Angstrom)	Height	Area(a1)	Area %	FWHM	XS(nm)
32.316(0.036)	2.7680(0.0060)	87.7(2.3)	5408.6(177.4)	100	2.408(0.080)	3(1)
40.092(0.104)	2.2472(0.0112)	21.3(2.0)	1082.4(127.3)	20	2.385(0.197)	3(1)
49.065(0.577)	1.8552(0.0409)	27.7(3.8)	4169.9(596.0)	77.1	7.093(0.432)	1(1)
51.069(0.199)	1.7870(0.0130)	13.3(6.6)	534.3	9.9	1.886(0.405)	4(2)

From table 4.2, the average crystallite size is 3.7nm.

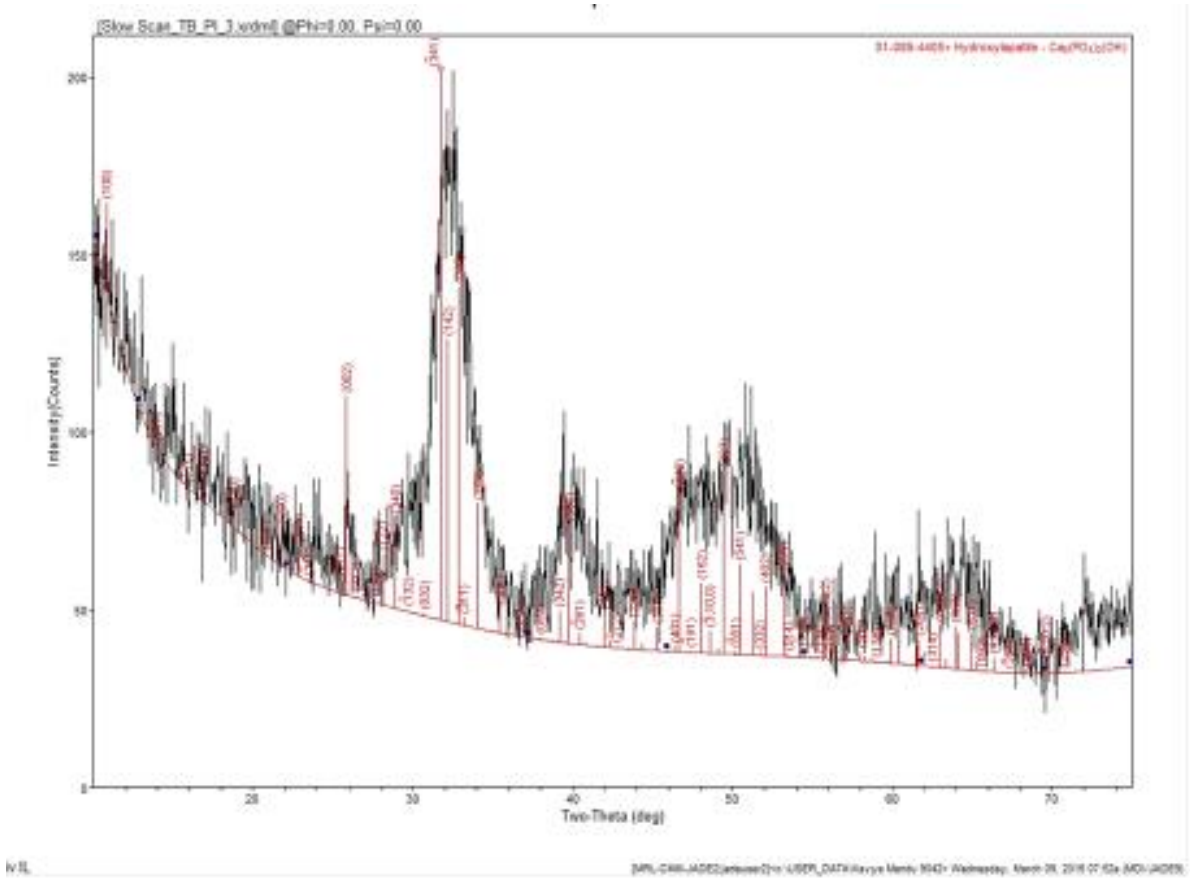

Figure 4.9 X-Ray Diffraction pattern of specimen 3 measured using PANalytical Xpert 2 MRD System and analyzed using JADE Software.

Table 4.3 Calculations related to the data obtained for specimen 3.

2-Theta	d(Angstrom)	Height	Area(a1)	Area %	FWHM	XS(nm)
32.316(0.036)	2.7680(0.0060)	87.7(2.3)	5408.6(177.4)	100	2.408(0.080)	3(1)
40.092(0.104)	2.2472(0.0112)	21.3(2.0)	1082.4(127.3)	20	2.385(0.197)	3(1)
49.065(0.577)	1.8552(0.0409)	27.7(3.8)	4169.9(596.0)	77.1	7.093(0.432)	1(1)
51.069(0.199)	1.7870(0.0130)	13.3(6.6)	534.3	9.9	1.886(0.405)	4(2)

From table 4.3, the average crystallite size is 3.3 nm.

A comparison between all three specimens could be obtained by overlaying the X-Ray Diffraction of the three specimens onto a single data file. Such an overlay is possible as the testing used for all the three specimens were consistent, slow scan rate and 2Theta range from 10^{o} to 75^{o}.

The results show that the samples showed weak diffraction peaks indicating low crystallinity. At the same time, these diffraction peaks were broad indicating small crystallite sizes as well. In this study, the average crystallite sizes were 3.3 nm for specimens 1 and 3, and 3.7nm for specimen 2.

Figure 4.10, shows that the specimens 1 and 3 were nearly identical, but sample 2 showed stronger diffraction peaks suggesting a higher crystallinity than the other two samples. With weak and broad

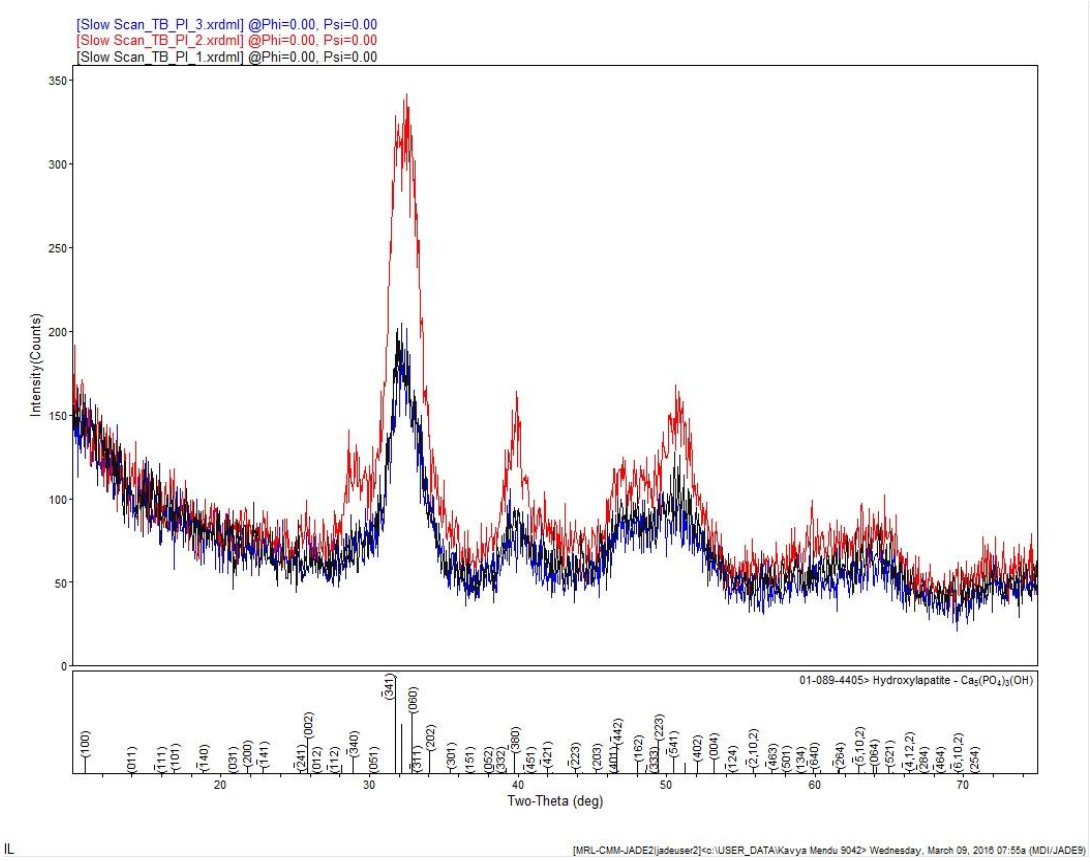

Figure 4.10 X-Ray Diffraction pattern of specimen 1,2 and 3 measured using PANalytical Xpert 2 MRD System and analyzed using JADE Software and overlapped on each other.

peaks, phase identification is always unruly. The three specimens used for this study showed a good peak match with Hydroxyapatite $Ca_5(PO_4)_3(OH)$, PDF (powder diffraction file) # 01-089-4405 from the ICDD database, with monoclinic crystalline structure. In this study using PANalytical Xpert 2 MRD System, angles smaller than 10^o were not explored and the material

bone was observed to have very weak crystallinity. Such a material can be easily tested using powder X-Ray Diffraction Technique.

4.4.2 Powder X-RAY Diffraction

The cortical bone specimen powder was prepared as mentioned in section 4.3.2 and was tested on the SIEMENS/BRUKER D-5000 instrument. The data was obtained for a 2theta range of 5 degrees to 90 degrees, a range greater than that of the one used in section 4.4.1. The data thus obtained was analyzed using JADE software, as mentioned earlier.

Figure 4.11, shows that the data that is obtained using Powder X-Ray Diffraction has shaper peaks when compared to the peaks shown in Figure 4.10. The data also shown an additional peak which had been constantly missing when using the PANalytical Xpert 2 MRD system. Thus it matches the peaks of Hydroxyapatite $Ca_5(PO_4)_3(OH)$, PDF (powder diffraction file) # 01-089-4405 from the ICDD database quite well.

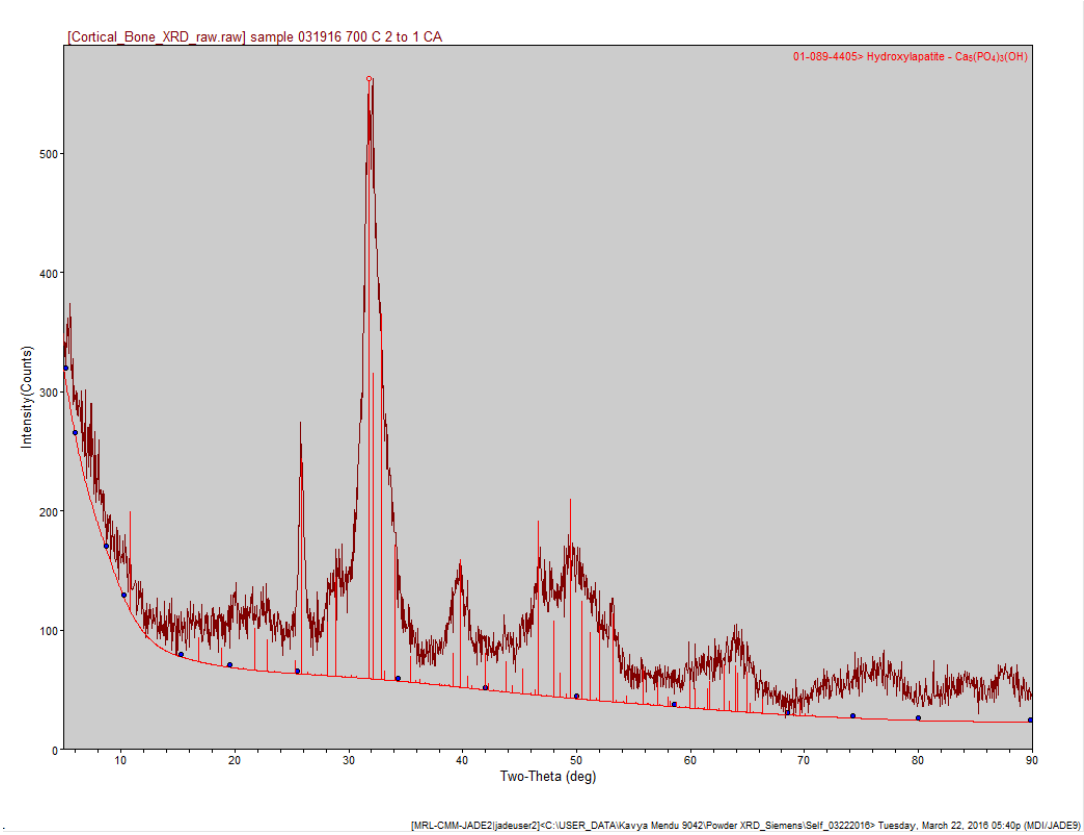

Figure 4.11 Powder X-Ray Diffraction on the cortical bone specimen.

In spite of all the above testing, though hydroxyapatite could be clearly distinguished using these studies, collagen, an integral part of bone structure could not be identified. This is due to the fact that collagen can be detected only at very small angles of the range 0.1 degree to 10 degrees (Piga et al, 2013; Fratzl et al., 2004; Rinnarthaler et al., 1999; Borah et al., 2005). Use of small angle x-ray scattering technique described in section 4.1.1 could be an extended study of the X-Ray diffraction on bone material.

4.5 Chapter Summary

In this chapter, we discuss the principle and working of the X-Ray Diffractometer used for the X-ray diffraction studies. These non-destructive studies are discussed in detail and the methods suitable for determining the composition of cortical bone specimens are explored. The PANalytical Xpert 2 MRD system, which enables slow scan modes and testing of specimens under air or vacuum gives us data without much noise within the range of 10 degrees to 75 degrees. For amorphous or weak crystalline materials like bone, Powder X-Ray Diffraction turns out to be a good alternative. The Powder X-Ray Diffraction data better matched with the peaks given in the database well. This can also be attributed to the fact that database is a result of testing the materials using Powder X-Ray Diffraction and then standardizing the results.

CHAPTER 5

INTRODUCTION TO MICRO SCRATCH TESTS

5.1 Scratch Test

The application of scratch test to determine the hardness of a material dates to the prehellanic era. In 1812, Carl Friedrich Christian Mohs formulated the Mohs scale of Hardness (Bowden and Tabor, 1964). This method characterizes the relative hardness of materials on a scale of 1 to 10 as shown in Figure 5.1. These materials of known hardness values are used to scratch the material of unknown hardness. The principle lies on the fact that a softer reference material will not be able to scratch the surface of the unknown material, whereas the harder material does. This method provides a quick qualitative assessment of the hardness of the material and its resistance to scratch. It also laid the foundation for idea of using scratch tests to characterize the mechanical properties of materials. This idea further garnered the interest of several researchers which led to the improvement of the technique over the centuries.

Further emphasis on the scratch test, led to the advancement of other hardness scales and tests. Early 1900s marked the development of Brinell Hardness (Tabor, 2000). It is a method to characterize the hardness of the material through the scale of penetration of the indenter into the material. The indenter is loaded with an external load as shown in Figure 5.2. A typical Brinell Hardness test uses a steel ball of diameter 10mm with 3000kgf load acting on it. Although, the

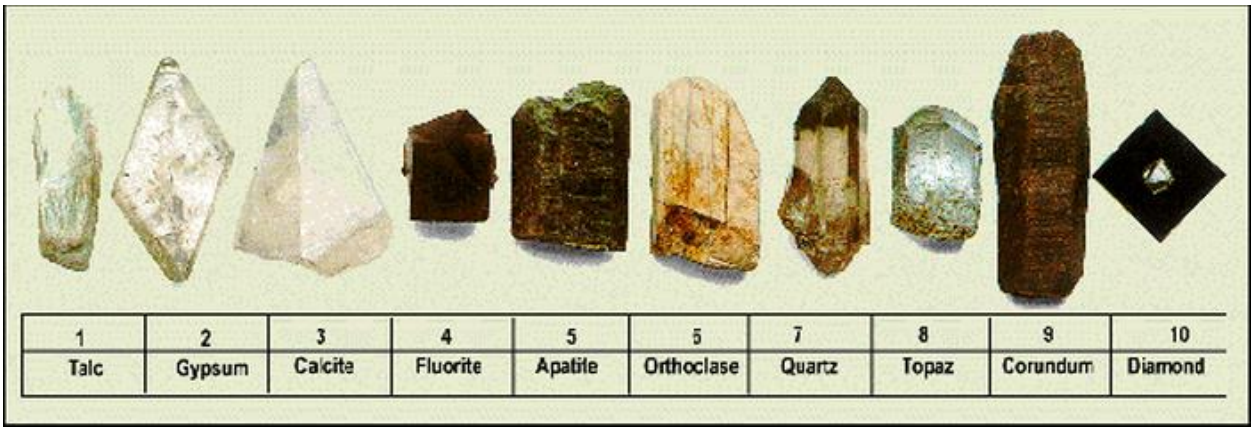

Figure 5.1 Mohs scale of hardness (Source: http://theprocessofrocks.weebly.com/mohs-scale-of-mineral-hardness.html).

applied force is subject to change depending on whether the material is soft or hard. Softer materials are subjected to smaller loads. In addition, a tungsten carbide ball replaces the steel ball for indentation of harder materials. The geometry of the indentation is as shown in Figure 5.2. A Brinell Hardness Number is calculated considering the dimensions of the indenter, applied load and dimensions of the indentation.

$$BHN = \frac{2P_0}{\Pi D(D-\sqrt{D^2-d^2}} \tag{5.1}$$

where BHN is Brinell Hardness Number (kgf/mm^2), P_0 is applied load in kilogram force (kgf), D is diameter of indenter (mm) and d is diameter of indentation (mm). The tests also establish a relation between the Brinell hardness and the ultimate tensile strength. Though Brinell hardness helped in advancement of the scratch technique to test the material properties, it turned out to be

slow and irreproducible for completely hardened steel. Besides, a typical Brinell hardness test was observed to make deep indents thus making it difficult to call it a non-destructive test.

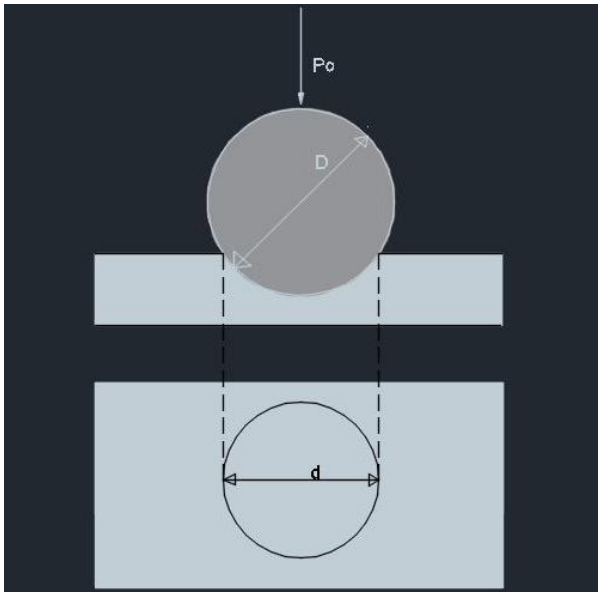

Figure 5.2 Schematic of the Brinell Hardness Test which uses a steel ball as an indenter.

The shortcomings in the Brinell Hardness test led to development in the Rockwell Hardness Scale (Rockwell and Rockwell, 1914). The method is based on the concept of differential depth hardness which accounts for the mechanical and surface imperfections of the materials and the instruments used (Ludwik, 1908). Firstly, an initial minor load is applied on to the material. This helps in determining the reference position or the zero position. Then, a major load along with the minor load is applied onto the material. This load application results in the indentation of the material. Further, the major load is now removed with the minor load still intact. A schematic of

the above discussion is shown in Figure 5.3. The depth of the penetration is measured and is inversely related to the hardness as shown in the equation below.

$$HR = N - \frac{d}{s} \tag{5.2}$$

where HR is the Rockwell Hardness, d is the depth of indentation from the zero-load point or the datum and N and s are scale parameters which are dependent on the test scale. This method is quick, reliable and robust with good resolution and small area of indent. Although precaution to be taken during the specimen preparation. The surfaces need to be flat else it would give lower values for the hardness. In addition, the specimen should be at least 10 times thicker than the depth of indentation.

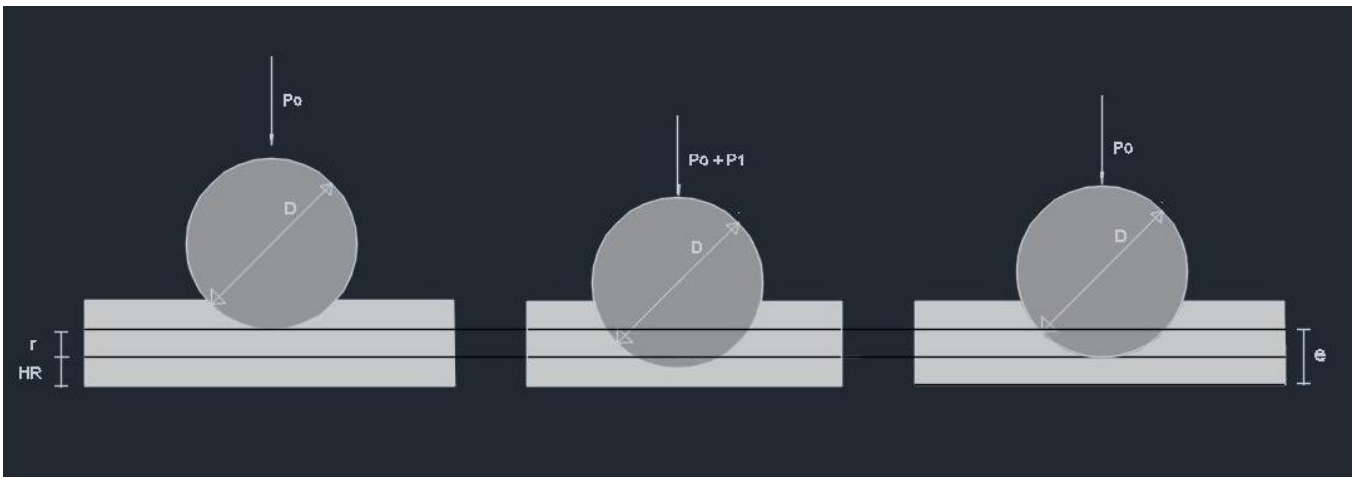

Figure 5.3 Force diagram of a Rockwell Hardness Test.

Vickers Hardness test was also developed as an alternative to Brinell Hardness test (Smith, 1921). This test works on the principle that a pyramid shaped diamond indenter is used to make indents on the material, to determine its resistance to plastic deformation. Vickers Pyramid number is determined independent of the size of the indenter. Further, it is defined as the ratio of the Force applied on the indenter to the area of the indentation. Vickers Hardness can be used on any material softer or harder, because we use the diamond indenter which is harder than most of the materials generally used for testing. The indenter has an intersection angle of 136^{o} and the area of indentation and thus the Vickers Hardness Number can be determined using the following equations.

$$A = \frac{d^2}{2\,sin(\frac{136}{2})}; \quad A \approx \frac{d^2}{1.8544}; \quad HV = \frac{F}{A} \approx \frac{1.8544F}{d^2} \tag{5.3}$$

where A is the Area of the indentation in mm^2, F is the applied force (P_o with respect to Figure 5.4) in kgf and d which is the average length of the diagonals of the indent is in millimeters. Sample thickness should be roughly 2.5 times the indent depth. Also, care needs to be taken regarding the interspacing of the indents to avoid interaction of the edges and work hardened regions. ISO 6507-1 and ASTM E384 standards are useful in this regard.

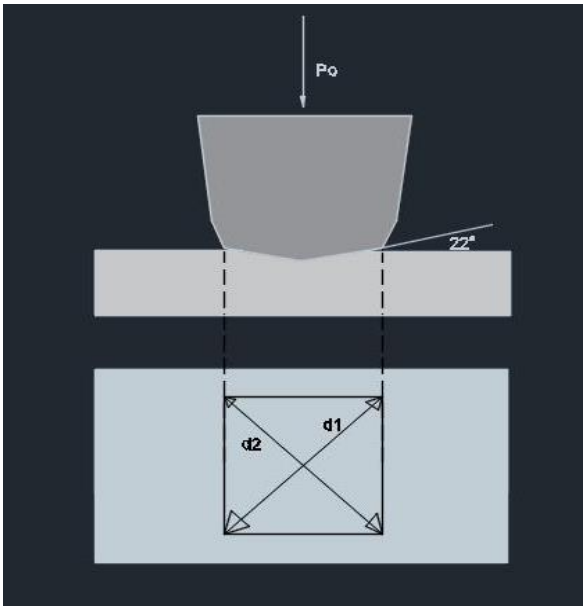

Figure 5.4 Geometry of the Vickers Hardness test. d1 and d2 are the diagonals of the projected area of the Vickers indenter.

All these methods form the basis of use of scratch testing for the measurement of material properties. Recent investigation on the scratch tests led to the development of the idea of using scratch tests as a measure to determine the fracture toughness of materials (Akono et al., 2011). Dimensional analysis, rigorous experimental investigations and complex theoretical models were thus introduced into the research community. The study was performed from the macroscopic to microscopic length scales and showed that scratch tests are fracture dominant processes. The macroscopic tests were conducted using a macro scratch tester designed for the study, whereas microscopic scratch tests were conducted using an axisymmetric conical Rockwell probe (Randall et al., 2001). The Rockwell conical indenter has a cone angle of 120^{o} and spherical tip radius of

200㎜m. The observations showed that the tests are highly scalable and the measured properties are dependent on the geometries of the indenters and indentation depths (Akono and Ulm, 2012; Akono et al., 2014).

5.2 Micro Scratch Test

5.2.1 Background

The use of scratch tests for the determination of fracture processes is based on the theory that during the process of scratching, the material undergoes fracture showing mechanisms like crack deflection, micro cracking, chipping and debris formation. However, the scratch groove is comprised of two phenomenon, plastic deformation and fracture process (Akono et al., 2011). Further as mentioned earlier, micro scratch tests further depend on the geometry of the indenter tip and scratch depths as well.

Prior to the determination of micro scratch tests as a means to calculate the fracture toughness, scratch adhesion tests were conducted on thin and hard ceramic coatings (Gonczy and Randall, 2005) using the Rockwell conical diamond indenter from the CSM Instruments Inc. The Rockwell indenter is used to scratch the coated surface to determine the wear or adhesion characteristics of the coating. The scratch parameters include a constant scratch speed, a defined normal force for a defined distance. The normal force could be either constant or increase progressively. During the process of the scratch, the failure events are determined and the

corresponding normal load is noted as well. ASTM Test Standard C1624-05 corresponds to the adhesion testing procedure. The test is designed for coatings in the range of 0.1 to 30㎜. The study suggests the use of a different indenter and force parameters for the coatings outside this range.

As shown in Figure 5.5, the test system used for the adhesion testing consisted of stylus and its mounting, mechanical stage and displacement control, test frame and force application system, force sensors, optical measurement and data acquisition. Although the study doesn't determine the fracture properties of the material, the study helps in understanding the schematic of the working of the Micro Scratch system which can be modified depending upon the requirements of the tests and the materials.

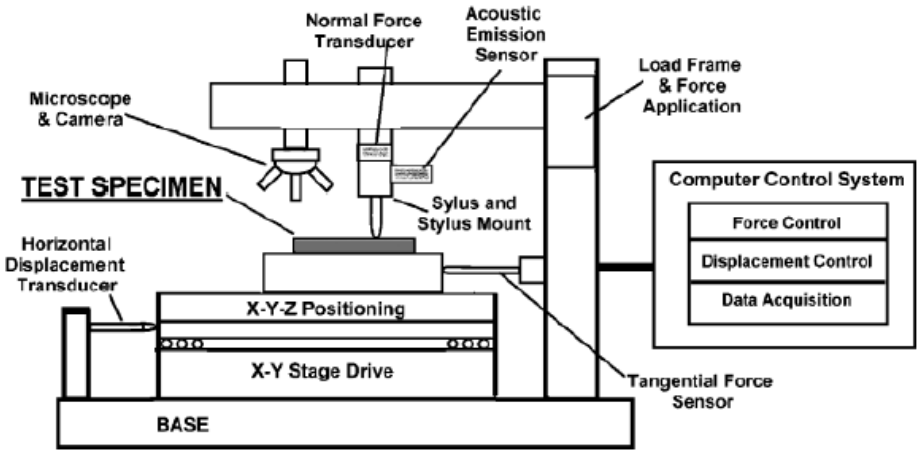

Figure 5.5 Schematic of scratch adhesion test with component subsystems (Source: ASTM C1624).

5.2.2 Equipment

Continuous stiffness measurement (CSM) Scratch testers available for the ranges nano, micro and macro are widely used in the research community. These instruments provide precise surface characterization measurements. As explained in the previous section, scratch testing can be employed for the characterization of thin films and coatings. Their mechanical properties such as adhesion, fracture and deformation can be measured using the CSM Scratch testers. The schematic of a CSM Scratch tester performing a scratch on the material whose properties are to be determined is as shown in Figure 5.6.

The CSM scratch tester performs a scratch on the target material for which the properties are to be determined under controlled testing conditions. The tip used for the scratch test is made of either diamond or a sharp metal. The diamond tip, though expensive, is mostly employed in the laboratories. Diamond being harder than most of the materials that are tested in the laboratories is the reason behind its wide application.

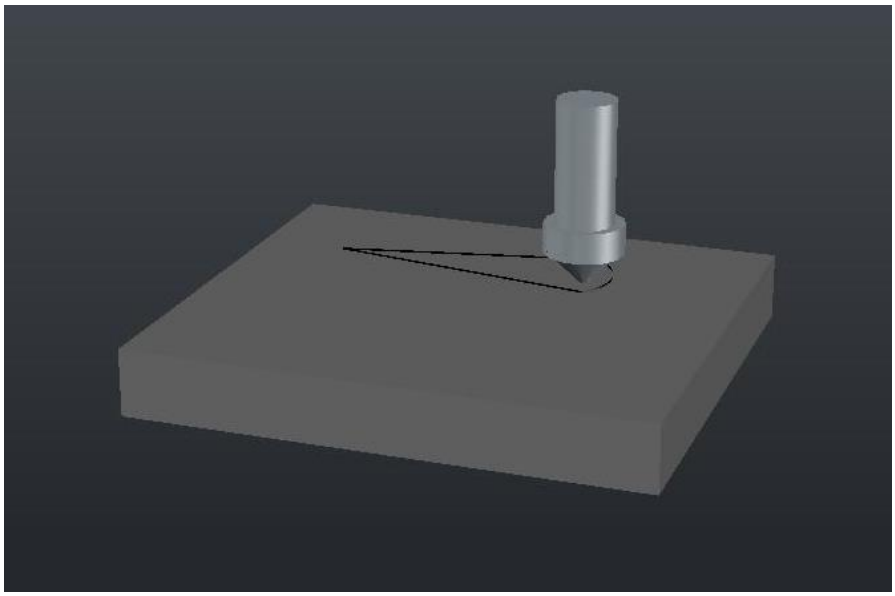

Figure 5.6 Schematic of the Scratch Test. A probe (in general, made of diamond for majority of the commercially available scratch testers) scratches the sample to determine the mechanical or fracture properties of the material.

The scratch testers support a wide range of indenters. For instance, spherical indenter, Rockwell indenter and Vickers indenter. Figure 5.7 shows the geometry of the spherical indentation. For spherical indenters, the contact stresses are initially small and are elastic. As the test progresses, further, a transition from the elastic to plastic deformation is observed. This can be used to study yielding, hardening and further to recreate the uniaxial tensile tests. Although the tests pose a difficulty when used at the microscopic scale, due to the difficulty to obtain high quality spherical indenters using hard materials.

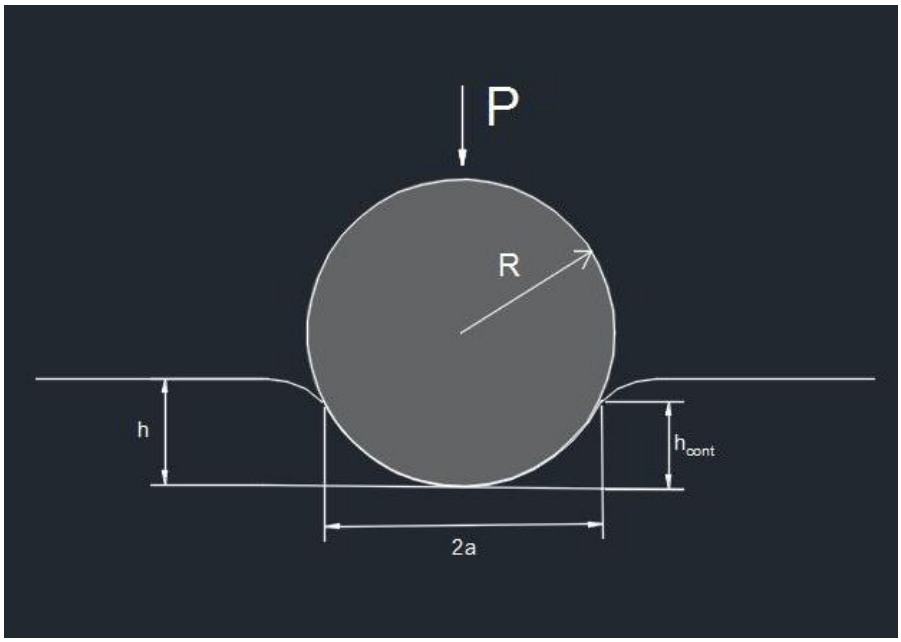

Figure 5.7 Schematic of the spherical indenter interaction with the material. A normal force of P is applied onto the sphere of radius R. This results in a contact radius of a and indent depth of h.

Furthermore, Vickers indenter has the geometry as discussed earlier in section 5.1. It is a four-sided pyramid shaped indenter with a 68^{o} angle between the center and the face of the pyramid. Figure 5.8 also the explained geometry of the Vickers diamond indenter. Rockwell conical

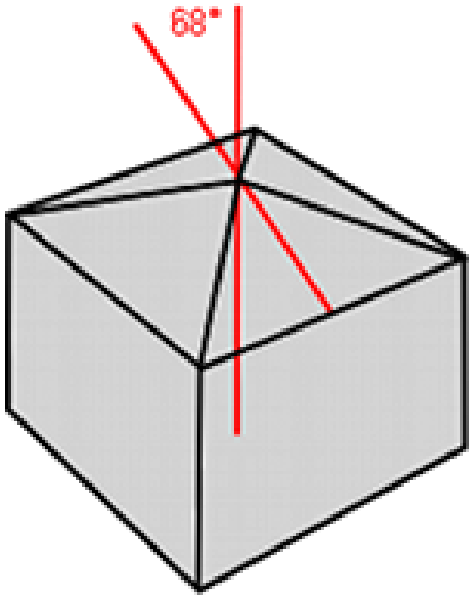

Figure 5.8 Vickers four-sided indenter tip with a center to face angle of 68^0 (Source: http://www.surface-tec.com/nanotips.php).

indenter has the geometry as described earlier as well. The cone apex angle is 120^o and with a radius of 200μm. The selection of the tip based on the study is an important step as the geometric properties have a say on the material parameters. An axisymmetric probe is observed to be suitable for the fracture toughness experiments (Akono and Ulm, 2012). Thus, a spheroconical Rockwell C indenter tip with the geometry as shown in Figure 5.9 is used in this study.

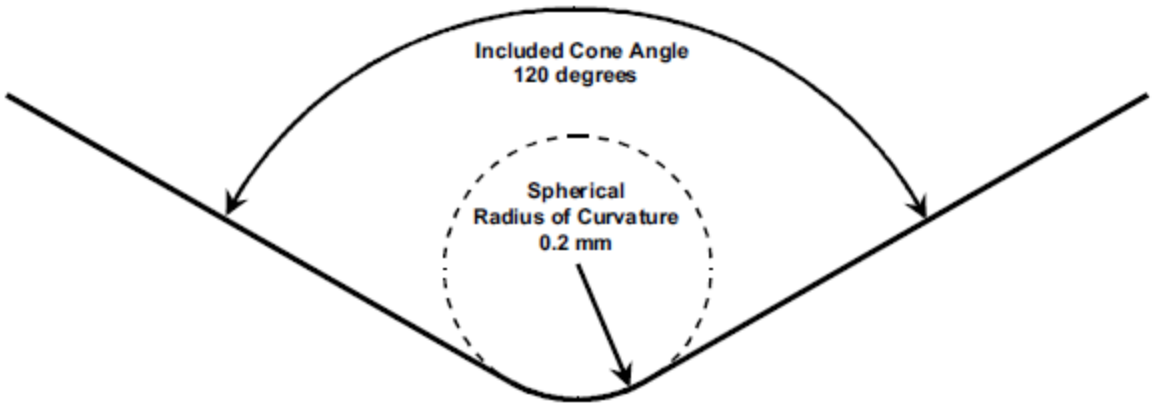

Figure 5.9 Sphero conical Rockwell C indenter.

The diamond indenter tip is drawn across the surface of the sample under the application of constant, progressive or incremental load modules available in the instrumental setup. This is shown in the Figure 5.10. The CSM Scratch tester offers a wide variety of features. One of its key features, is the constant surface referencing. This enables accurate coordination between the force and depth sensors. In addition, the electronically controlled active force feedback system unique to the Micro scratch tester developed by CSM Instruments Inc. enables higher precision. The normal force which is an important factor in the scratch tests is also perfectly controlled due to the above force sensor and active force feedback feature.

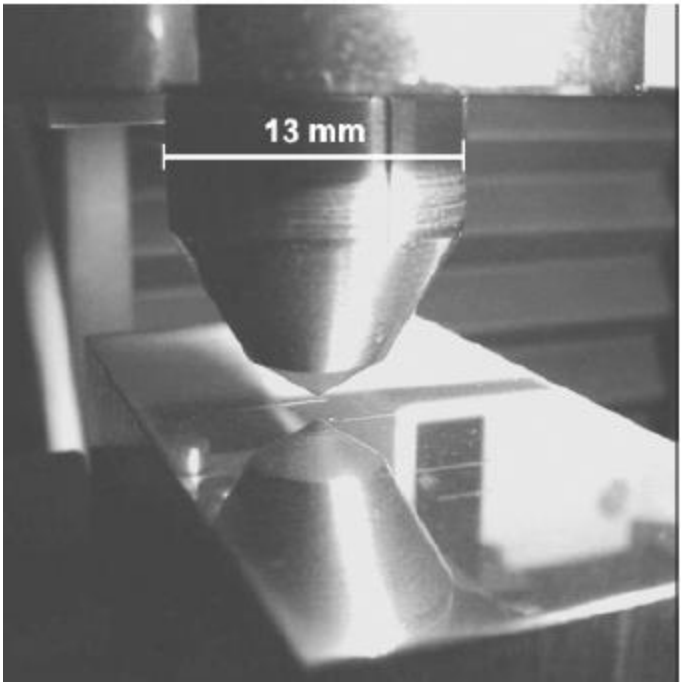

Figure 5.10 Micro scratch tester performing a scratch test on the test specimen (adopted from Gonczy and Randall, 2005).

The sample for scratch testing is mounted on a friction table. The transducer attached to this table measures the coefficient of friction. The selection of prescan mode in the scratch software enables the displacement sensor to examine the surface profile of sample before the scratch test. In addition, profiles are measured during and after the tests as well. The penetration depth, *Pd* is measured during the scratch test. Residual depth, *Rd* is measured after the scratch test. Elastic and viscoelastic properties of the material are determined after the comparison between the measured depths *Pd* and *Rd*. The pre-scan and post scan modules determine the surface profiles of the

material using low loads without deforming the material. This Prescan and Post scan modules are patented (US 6,520,004 B1) by the CSM Instruments Inc. Figure 5.11 adopted from CSM Micro Scratch Documentation shows the pre scan and post scan profiles of a coated material.

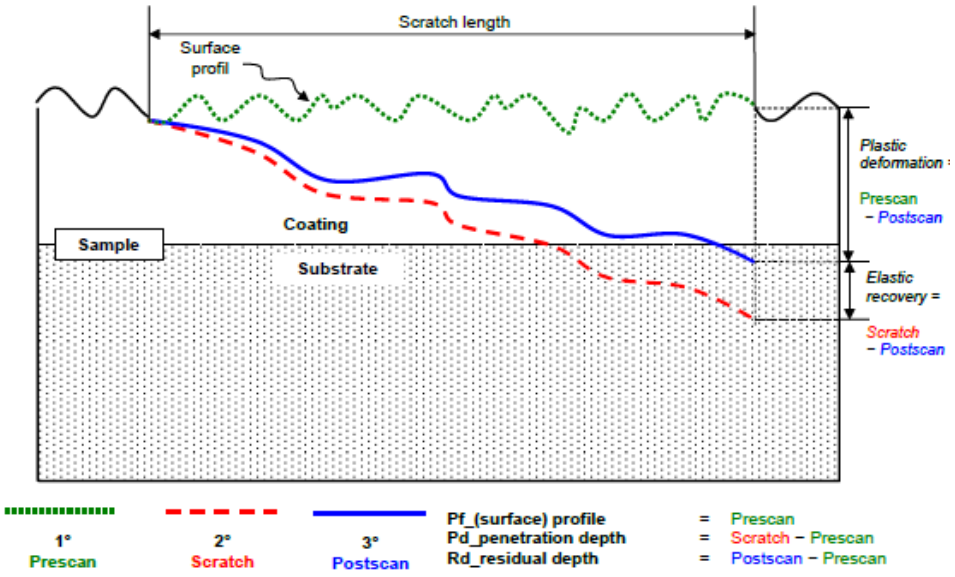

Figure 5.11 Patented Pre-scan and Post scan modes of the CSM Instruments Inc. measuring the surface profiles (CSM Micro scratch tester documentation).

Furthermore, optical microscope is synchronized with the scratch tester. This enables in the capture of optical microscopy images of the test site. The optical microscope is available at four levels of objectives x5, x20, x50 and x100. These correspond to magnifications from x200 to x4000. The objectives are high quality Olympus objectives and consists of USB 2.0 video camera.

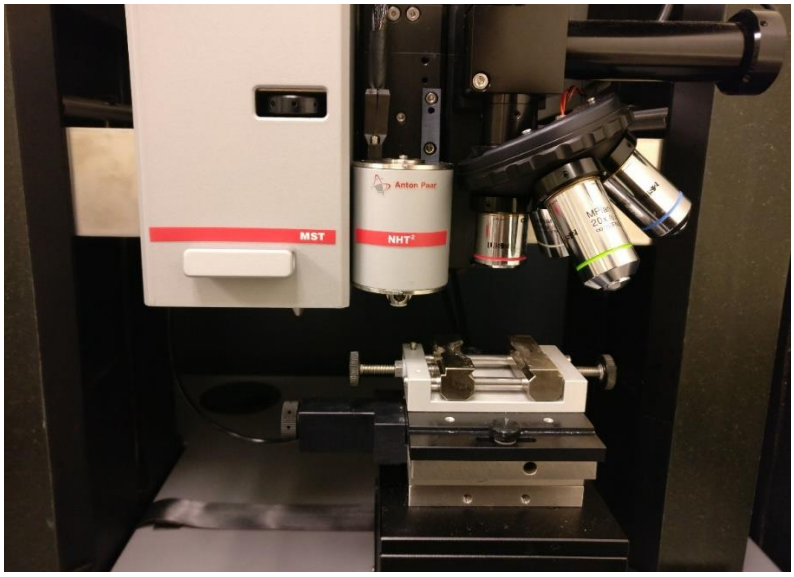

Figure 5.12 Image showing the sample stage, optical microscopy setup, micro scratch tester head and nano indentation tester head (Credits: Kavya Mendu, UIUC, 2017).

Micro scratch tester is also associated with a patented synchronized panorama mode. This feature enables us to capture the entire scratch groove and correlate it to the data after the scratch test is performed. It further enables us to correlate the data to the micromechanical features on the test specimen, a very valuable tool in the case of a material which has variable surface features and thus is highly heterogeneous. Figure 5.13 shows an image adopted from the CSM Instruments Inc Micro Scratch Tester Documentation. It shows the panorama of the scratch groove which is a result of several images being stitched together to form the complete scratch.

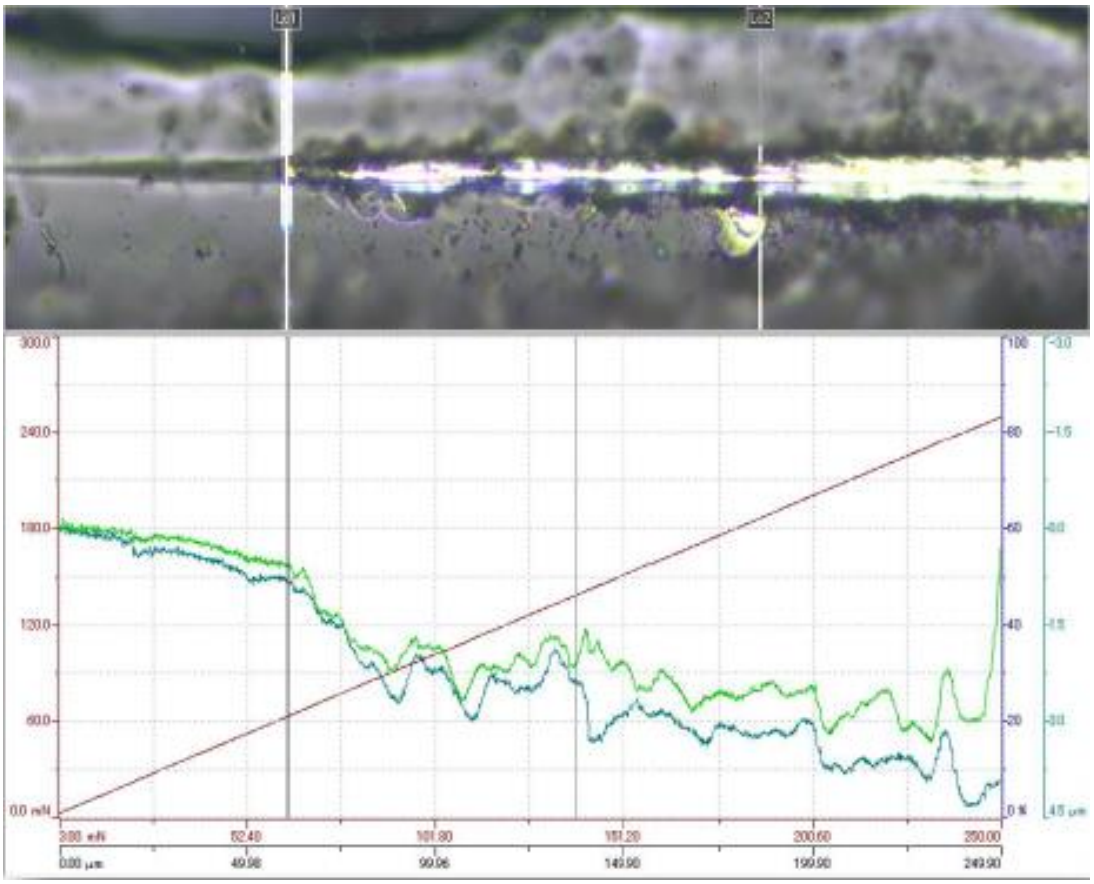

Figure 5.13 Image showing the panorama of the scratch groove and the data acquainted from the sensors (adopted from the documentation of CSM Micro scratch tester).

5.2.3 Typical Procedures

Section 5.2.1 gives a description of the various parts and key features of the micro scratch tester. The methodology involved in the measurements can be explained as follows. The specimen is placed on the friction table and then positioned under the optical microscope. Thus, the test site is now selected. In case, a series of tests need to be conducted on the specimen, surface of the

specimen can be explored under the optical microscope using vector move options. However, after the site selection, the scratch test can be launched. This moves the sample from under the microscope to that of the scratch tester. The indenter then lowers on to the specimen, runs a pre-scan surface profile measurement if selected. It then attains the low contact load as prescribed. Followed by this is the scratch test which is carried on the specimen.

The load cell monitors the applied load using the force sensors and active feedback system. Penetration depth is measured using Linear Variable Differential Tensor (LVDT) sensor. Frictional force is measured using an LVDT sensor as well attached to the friction table. Acoustic sensor attached to the Scratch head measures the acoustic emissions corresponding to the failure events occurring in the specimen. The testing should be in controlled environments with temperatures in the range of (23±5) ^{o}C and a relative humidity less than 50% as per the ISO standards (ISO 14577-1).

5.3 Technical Specifications

The instrument has very fine resolutions for the parameters discussed so far in the above sections. The different parameters and their ranges and resolutions are tabulated as below. Sustainability under the nano scope laboratory at University of Illinois at Urbana Champaign has the micro scratch tester with a compact platform and standard displacement table. All the other parameters, like

penetration depth, normal load, friction load, acoustic sensor parameters, scratch speed and the sample size are in agreement with Table 5.1.

Table 5.1 Parameters of the micro scratch tester formulated in the tabular form. Data as obtained from the manufacturer of the ANTON PAAR MST, CSM Instruments Inc.

Penetration Depth		
	Fine Range	Large Range
Maximum Depth (um)	100	1000
Depth Resolution (nm)	0.3	3
Normal Load		
	Fine Range	Large Range
Maximum Load (N)	10	30
Load Resolution (mN)	0.1	1
Friction Load		
	Fine Range	Large Range
Maximum Friction Load (N)	10	30
Resolution Friction Load (mN)	0.1	1
Acoustic Emission Sensor		
Central Frequency (KHz)	150	

Table 5.1 (cont.)

Dynamic range (dBae)	65	
Maximum amplification	200000x	
Scratch Speed		
	Fine Range	Large Range
Standard displacement table (mm/min)	0.4	600
High Resolution Displacement Tables(mm/min)	0.1	600
Maximum Sample Size		
Compact platform (mm)	200 x 200 x 100	
Open Platform (mm)	295 x 300 x 100	

5.4 Chapter Summary

This chapter documents the initial application of the scratch testing as a means to determine the material properties such as hardness. It describes the advancement of the different hardness measurements over the past few decades. Micro scratch testing and its applications such as determining the wear and adhesion characteristics of the coating were determined. The more recent approach of the use of scratch tests at various scales as a means to determine the fracture

toughness of the material was discussed. Finally, the micro scratch tester equipment was described in detail.

CHAPTER 6

APPLICATION OF MICRO SCRATCH TESTS TO CORTICAL BONE

The principle and applications of scratch tests to determine the material properties at various length scales were discussed earlier in section 5.1. The idea of using scratch tests as a tool to determine the fracture toughness of the material had been recently introduced into the research community (Akono, 2011). The method gained momentum due to the scalability and reproducibility offered by it.

Biomedical applications of micro scratch tests were previously explored by researchers (Liu et al., 2001; Groot et al., 1987; Freeman, 1992). Micromechanical properties of calcium phosphate coatings, adhesion properties of contact lens coatings, mechanical properties of teeth materials, scratch resistance of arterial implants, hardness of bone tissue and characterization of tin oxide coatings are numerous biomedical applications. However, use of micro scratch tests to determine the fracture toughness of cortical bone specimens is a novel experimental technique carried out as a part of this study.

6.1 Specimen Preparation

As discussed earlier, this chapter presents an overview of the fracture properties of cortical bone specimens. Swine and bovine cortical bones were tested for this study. As described in section 2.1

of literature review, hierarchical structure of swine and bovine cortical bone specimens is equivalent to that of the human bone specimens. The anatomy and physiology are considered to be comparable (Feng and Jasuik, 2011). This analogy enabled several researchers to conduct experiments on swine and bovine bone specimens to understand the mechanical properties of cortical bone.

Besides, certain limitations come in the way when we intend to test the human cortical bone specimens. That is, testing the human cortical bone not only requires the lab to be additionally certified for biological testing of the human specimens but also the number of specimens available for the study will be significantly low. For an extensive experimental study, there is a need for abundance of specimens which not only enables us to perform various parametric studies but also helps us in a complete understanding of the material that is being tested. All the above reasons support the study of the swine and bovine bone specimens. Most importantly, the swine and bovine bone specimens are readily available for testing in nearby slaughter houses and science laboratories, thereby reducing the effects due to the transportation of the specimens if any.

6.1.1 Specimen Procurement

Porcine or swine femurs were obtained from the Meat Science Laboratory of University of Illinois at Urbana Champaign. Bones were obtained from 22-26 weeks old swine which were harvested for a duration of 24 hours after slaughter. The animals were corn fed and weighed about 275

pounds. The femurs were transported from the Meat Science Laboratory in plastic air tight bags. The femurs thus obtained were kept frozen at -20^{o}C temperature in order to keep them fresh until the specimen preparation procedure commenced. Several studies used the temperature of -20^{o}C for the storage of the bone specimens (McAlden, 1993; Zioupous, 2006). Furthermore, a study on the various storage methods showed that freezing the specimens at -20^{o}C keeps the specimens relatively fresh (Linde and Christian, 1993).

Figure 6.1 Swine Femur obtained from the Meat Science Laboratory, UIUC, Urbana, IL. Credits: Amrita Kataruka, UIUC, 2017.

Further, bovine femurs were obtained from L&M slaughter house, Georgetown, Illinois. The animals were corn fed too. They weighed about 1000-1100 pounds and do not have a record of any disease or infection that occurred during their lifetime. Also, they were 24-30 months old and were aged for 8 days after slaughter. The femurs were then stored in a similar way as that of

the swine femurs, kept frozen at -20^{o}C temperature until the commencement of the specimen preparation.

6.1.2 Cutting and Cleaning

Femurs stored at -20^{o}C were thawed and sections were cut from the mid-diaphysis region using a Table Top Diamond Band Saw. The trabecular bone region containing the tissue was then removed using a dissection kit as our interest is only in the Cortical Bone Region of the Femur. As discussed earlier in chapter 3, the study pertains to two distinct orientations of the cortical bone. Longitudinal transverse and short longitudinal are the two directions. Longitudinal – Transverse (LT) specimens correspond to the fracture properties in the direction perpendicular to the longitudinal axis of the cortical bone specimens. Whereas, Short – Longitudinal (SL) specimens correspond to the fracture properties in a direction along the longitudinal axis of the specimens. These specimens are significantly different due to the anisotropy exhibited by bone, as mentioned in the bone histology.

The mid diaphysis region of the femurs were further cut using a diamond-wafering blade on the Buehler Isomet 5000 precision cutter (Buehler, Lakebuff, IL) to obtain smaller sizes. The Isomet 5000, has a 7in diameter diamond-wafering blade and 2-micron sample positioning system. This enables us to precisely section the specimens and efficiently cut the specimens without damage. Also, Isomet has a cutting capacity of up to 8 in. For the Porcine and Bovine Cortical

Bone Specimens, the parameters adopted were as described. A blade speed of 1500rpm, with a feed rate of 2.5-3mm/min.

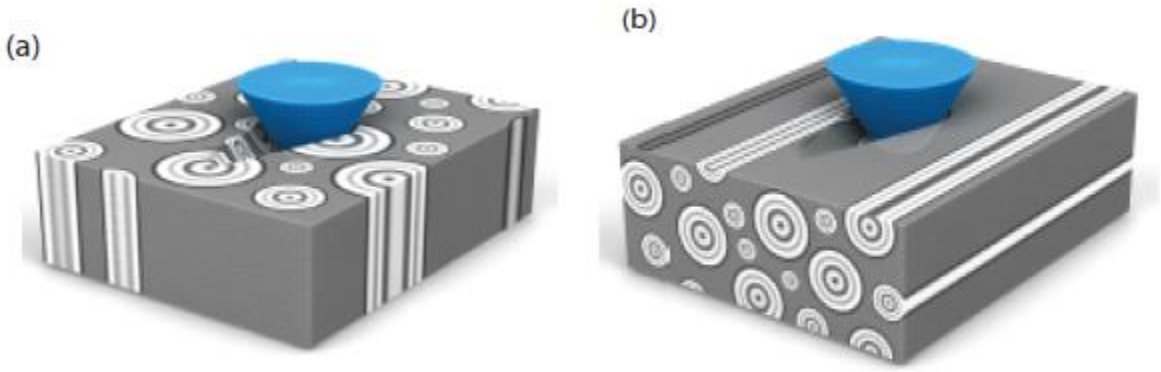

Figure 6.2 (a) Schematic of the scratch test on the Longitudinal Transverse specimen (b) Schematic of the scratch test on the Short-Longitudinal specimen (Credits: Beckman Institute Visualization Lab, UIUC, 2015).

Adopting a feed rate as low as 2.5mm/min increased the duration of the cutting process. In spite of that, the low speed is justified as it helps in the minimum amount of damage or manufacture artefacts that occur during specimen preparation leading to smooth and flat surfaces avoiding occurrence of wedging. The cutting procedure is a wet process where in the coolant used is a solution of Isocut Cool 3 with Distilled Water in a ratio of 1:25. After this procedure, the dissection kit is again employed to remove any unwanted flesh or tissue material on the bone specimens. A deeper cleaning of the specimens is done in a solution prepared using 1.5% Alconox and 5%

Bleach and ultra-sonically cleaned for a duration of 20 minutes. The specimens are now ready to be embedded into the resin.

6.1.3 Embedding, Grinding and Polishing

Each of these cortical bone specimens are now embedded in a casting resin in order to facilitate easy handling and enhance stability of the specimens during grinding, polishing and testing. Several protocols for embedding, grinding and polishing were tried and tested in the due course of obtaining a standard procedure for both porcine and bovine femurs. A complete account of the several protocols tested, the limitations and shortcomings faced in each of them, which led to the final preparation is described as follows.

As an initial procedure, the porcine cortical bone specimens were oven dried at a temperature of 50^{o}C for 24 hours (Yeni et al 2000; McAlden 1993) and later embedded in epoxy resin (Epothin, Buehler) at room temperature. The curing time was around 9 hours. Hardening of the resin was an exothermic reaction, thus leading to a rise in the temperature by about 3-4^{o}C. In order to avoid this heating of the specimens and to maintain in vivo conditions, certain changes were adopted in the procedure. The cleaned and wet specimens, instead of oven drying them were embedded in the epoxy resin as is, so that the specimens remain hydrated. As an advancement to this, even the Epoxy Resin was replaced with Polymethyl Methacrylate (PMMA) which has relatively shorter curing time of 4-5 hours. Also, the hardening of the acrylate is not as exothermic

as that of Epoxy Resin as well, thus leading to very slight variations in the temperature during the process of embedding the specimens. Embedded specimens were then cut into 5-mm thick discs using the Buehler Isomet 5000 Precision Cutter (Buehler, Lakebuff, IL). The specimens are then mounted on to metal (aluminum) discs using cyanoacrylate adhesive. Thus, the longitudinal specimens, longitudinal-transverse (LT) the femurs were made into semicircular sections as shown in Figure 6.3. Whereas for the transverse specimens, short-longitudinal (SL) they were made into approximately 1cm X 1.5cm X 5mm cuboidal shapes as shown in Figure 6.4.

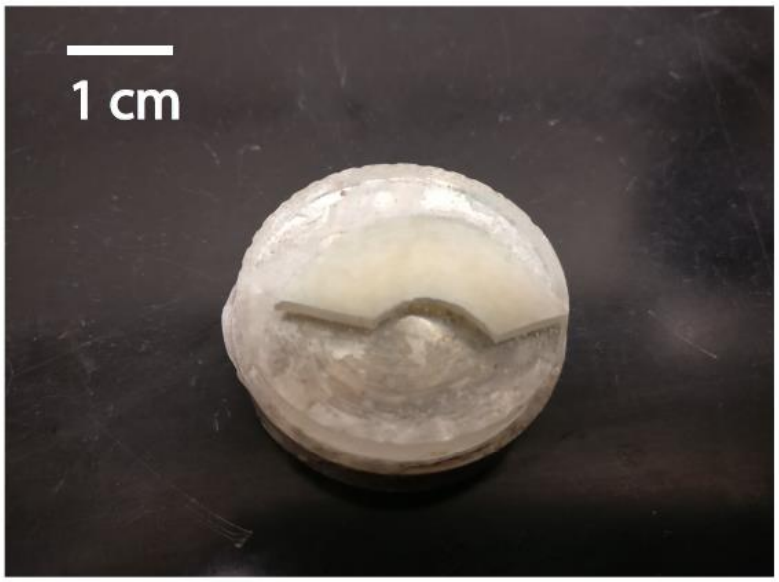

Figure 6.3 Longitudinal Transverse Bovine Cortical Bone Specimen (Credits: Kavya Mendu, UIUC, 2017).

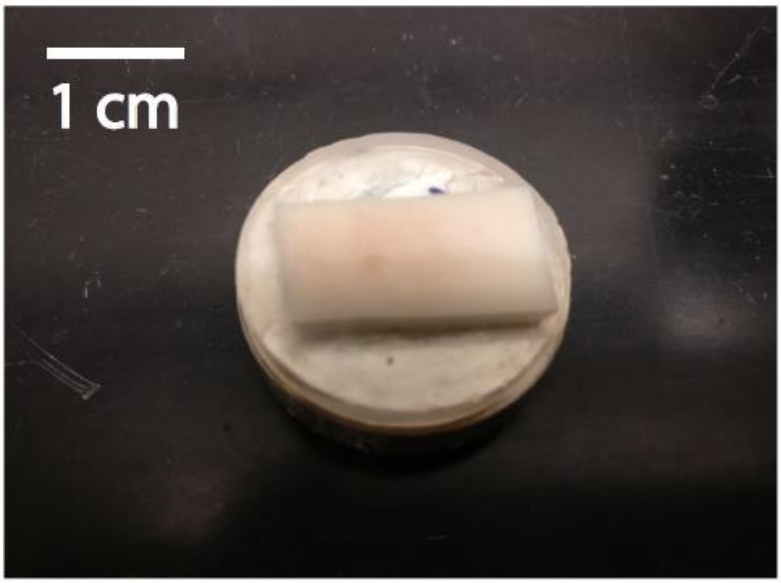

Figure 6.4 Short - Longitudinal Bovine Cortical Bone Specimen (Credits: Kavya Mendu, UIUC, 2017).

In order to obtain smooth and level surfaces, the specimens are to be ground and polished. The specimens were to be wrapped in a gauge soaked in Hanks Balanced Salt Solution or a Phosphate buffered Saline Solution and stored in the refrigerator set at 4^{o}C until further use, if they aren't used immediately. Soaking the specimens enables us to retain the hydration of the bovine and porcine specimens, especially of the exposed surfaces of the bone. Also, keeping the bones hydrated helps in mimicking the conditions that the bones located inside the human or animal body possess (Zioupos, 2001).

The epoxy embedded porcine cortical bone specimens were ground and polished using Buehler Ecomet 250 Grinder-Polisher. The final polishing protocol evolved as a result of several

trails and modifications were adopted for the polishing protocols in order to obtain a surface which is finely ground and polished. The different procedures adopted before the final protocol was formulated are described below, so that an account of various methods and their outcomes are available. In addition, different protocols had to be adopted for porcine and bovine bone specimens as well.

Protocol I

Firstly, the protocol had a procedure which involves grinding of the porcine cortical bone specimens using 400, 600, 800 and 1200 grit silicon carbide abrasive pads (Buehler, Lakebuff, IL). The duration of grinding was uniform for all the steps and was 2 minutes under a load of 2 lbs. Grinding is followed by polishing using 9 µm, 3µm, 1µm and 0.25µm diamond suspensions on Texmet P (Buehler, Lakebuff, IL). The duration adopted for each of the polishing steps were 15 minutes under a load of 3 lbs. All the above polishing and grinding steps operate at a base speed of 300 rpm and a head speed of 60 rpm on the Ecomet 250 (Buehler, Lakebuff, Illinois). The specimens are to be ultrasonically cleaned between each of these grinding and polishing steps to avoid cross contamination. A Branson 5800 Ultrasonic Cleaner was employed for the same and thus the specimens were cleaned for a duration of 2 minutes each after the intermediate steps of grinding and polishing.

Figure 6.5 Ecomet 250 Grinder and Polisher, Buehler, Lakebuff, IL (Credits: Kavya Mendu, UIUC, 2017).

A quick and easy way to observe the quality of polishing procedure is to examine the specimen under light and observe the extent of reflection of light from these surfaces. Finely polished surfaces possess smooth and shiny surfaces to facilitate the testing at the nano and micro scales. Advanced surface examination of the specimens can be performed using optical microscopy. Under the optical microscopy, we observe the osteons, haversian canals and interstitial regions of the cortical bone specimens. In addition, if the procedure is yielding good results then we do not observe a surface which is having several scratches due to the grinding and

polishing on the bone specimens. An additional comment on this initial procedure is that the specimens that were ground or polished were not immersed in the physiological solution namely PBS. As we can see from Figure 6.6, the bone features at the mesoscale were visible, but at the same time, several scratches were evident on the surface. This calls for a better polishing and grinding procedure.

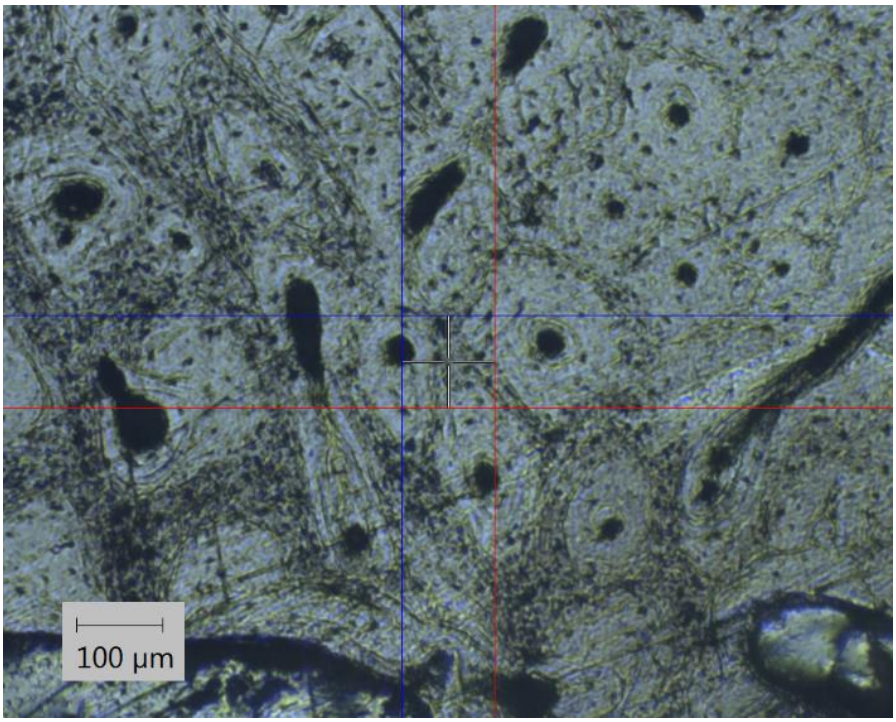

Figure 6.6 Image of the polished specimen using the protocol I.

Table 6.1 Summary of the Steps involved in polishing the porcine cortical bone specimens using Protocol I.

Grinding						
Step	Grit Size	Pad	Base Speed	Head Speed	Duration	Force
1	400 grit	Silicon Carbide	150 rpm	60 rpm	2 minutes	2 lbs
2	600 grit	Silicon Carbide	150 rpm	60 rpm	2 minutes	2 lbs
3	800 grit	Silicon Carbide	150 rpm	60 rpm	2 minutes	2 lbs
4	1200 grit	Silicon Carbide	150 rpm	60 rpm	2 minutes	2 lbs
Polishing						
1	9 microns	TexMet P	300 rpm	60 rpm	15 minutes	3 lbs
2	3 microns	TexMet P	300 rpm	60 rpm	15 minutes	3 lbs
3	1 microns	TexMet P	300 rpm	60 rpm	15 minutes	3 lbs
4	0.25 microns	Texmet P	300 rpm	60 rpm	15 minutes	3 lbs

Protocol II

The previous protocol was then modified by incorporating an additional step of immersing the specimens in phosphate buffer solution after embedding them. This was to avoid dehydration of the specimens. Followed by this modification came in the step which embraces the inclusion of

0.05µm alumina solution used to further polish the cortical bone specimens on the Pressure Sensitive Backed (PSA) backed 8 inch diameter MicroCloth (Buehler, Illinois). This step is assimilated in order to enhance the polishing procedure to a much finer step compared to the ones till 0.25µm (Xu et al 2003). The duration of this step was 4 minutes under a load of 3lbs. In this particular step, a small technical detail that is to be noted is that, the use of spacers, which are used to hold the specimens in place, on the microcloth is to be avoided, as it was observed that the use of spacers for the polishing procedure damages the microcloth unlike when they were used against the relatively robust Texmet P polishing cloth.

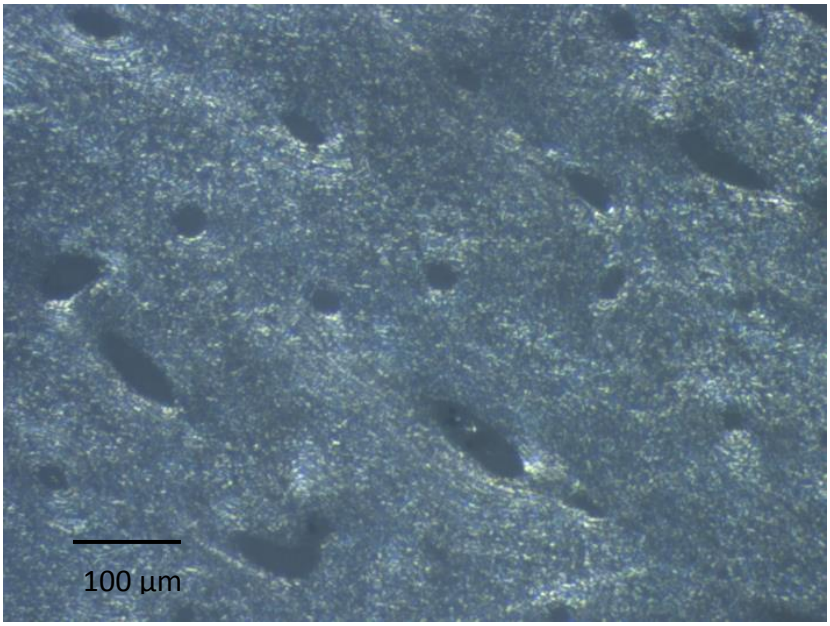

Figure 6.7 Polished specimen with the modifications made in the polishing procedure as described in Protocol II.

Table 6.2 Summary of the Steps involved in grinding and polishing the porcine cortical bone specimens using Protocol II.

Grinding						
Step	Grit Size	Pad	Base Speed	Head Speed	Duration	Force
1	400 grit	Silicon Carbide	150 rpm	60 rpm	2 minutes	2 lbs
2	600 grit	Silicon Carbide	150 rpm	60 rpm	2 minutes	2 lbs
3	800 grit	Silicon Carbide	150 rpm	60 rpm	2 minutes	2 lbs
4	1200 grit	Silicon Carbide	150 rpm	60 rpm	2 minutes	2 lbs
Polishing						
1	9 microns	TexMet P	300 rpm	60 rpm	15 minutes	3 lbs
2	3 microns	TexMet P	300 rpm	60 rpm	15 minutes	3 lbs
3	1 microns	TexMet P	300 rpm	60 rpm	15 minutes	3 lbs
4	0.25 microns	Texmet P	300 rpm	60 rpm	15 minutes	3 lbs

Protocol III

Besides the above two protocols, a polishing procedure which is quicker than the above-mentioned procedures were developed with the motivation from the literature. It can be described as follows. Grinding the cortical bone specimens using 400, 600, 800 and 1200 grit silicon carbide abrasive

pads with a duration of 2 minutes under a load of 2 lbs. Followed by a polishing procedure which directly uses 0.05µm alumina solution on a micro cloth for a duration of 4 minutes and 3 lbs. (Zioupus; 2007). This procedure, even though avoided a lot of steps in the polishing procedure gave specimens with finely polished surfaces. In spite of having finely polished surfaces, the optical microscopy images depicted scratches on the surface. The goal is to standardize a procedure for grinding and polishing bone specimens, for this we are looking for surfaces which are looking the best when using the above procedures and not how quicker the polishing procedure is, the quicker procedure which bypassed several polishing steps is eventually passed.

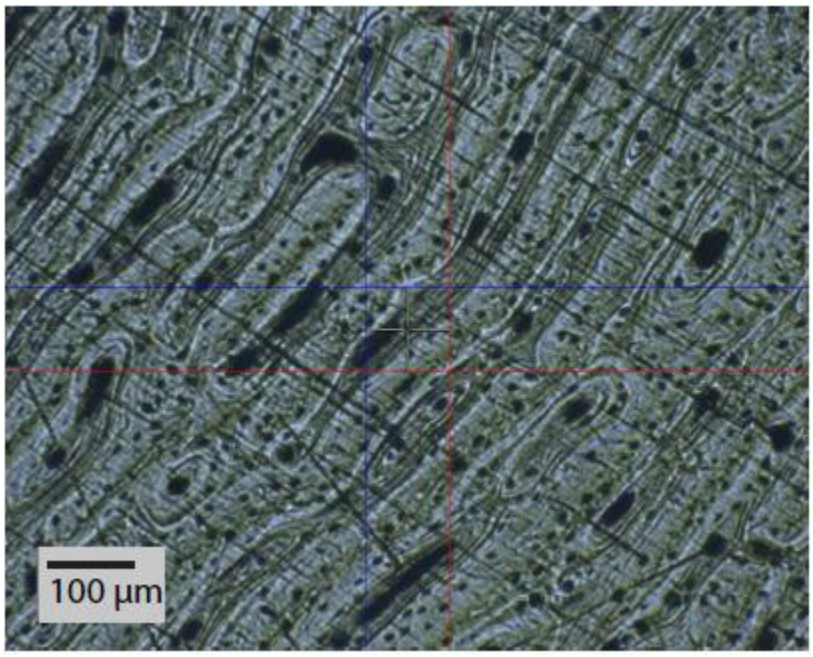

Figure 6.8 Image of the polished specimen using the protocol III.

Table 6.3 Summary of the Steps involved in polishing the porcine cortical bone specimens using Protocol III.

Grinding						
Step	Grit Size	Pad	Base Speed	Head Speed	Duration	Force
1	400 grit	Silicon Carbide	150 rpm	60 rpm	2 minutes	2 lbs
2	600 grit	Silicon Carbide	150 rpm	60 rpm	2 minutes	2 lbs
3	800 grit	Silicon Carbide	150 rpm	60 rpm	2 minutes	2 lbs
4	1200 grit	Silicon Carbide	150 rpm	60 rpm	2 minutes	2 lbs
Polishing						
1	0.05 microns	Microcloth	300 rpm	60 rpm	4 minutes	3 lbs

Protocol IV

Followed by the above three protocols, a modification to the Protocol 1 was again made. In this procedure, grinding of cortical bone specimens using 400, 600, 800 and 1200 grit silicon carbide abrasive pads were used with varying durations of 1 minute, 5 minutes, 15 minutes and 15 minutes respectively under a constant load of 2 lbs. Followed by the grinding procedures, in the polishing procedures 3µm, 1µm, 0.25µm diamond suspensions were used on Texmet P and 0.05µm alumina suspension on Microcloth, each step having a duration of 20 minutes each under a load of 2 lbs.

The specimens prepared using this procedure appeared to have very shiny and smooth surfaces. At this particular juncture, the issue of wedged specimens came into light.

Table 6.4 Summary of the Steps involved in polishing the porcine cortical bone specimens using Protocol IV.

Grinding						
Step	Grit Size	Pad	Base Speed	Head Speed	Duration	Force
1	400 grit	Silicon Carbide	150 rpm	60 rpm	1 minutes	2 lbs
2	600 grit	Silicon Carbide	150 rpm	60 rpm	5 minutes	2 lbs
3	800 grit	Silicon Carbide	150 rpm	60 rpm	15 minutes	2 lbs
4	1200 grit	Silicon Carbide	150 rpm	60 rpm	15 minutes	2 lbs
Polishing						
1	3 microns	TexMet P	300 rpm	60 rpm	20 minutes	2 lbs
2	1 microns	TexMet P	300 rpm	60 rpm	20 minutes	2 lbs
3	0.25 microns	TexMet P	300 rpm	60 rpm	20 minutes	2 lbs
4	0.05 microns	Texmet P	300 rpm	60 rpm	20 minutes	2 lbs

Protocol V

The grinding procedures using 400 grit and 600 grit were observed to be mainly contributing to this wedging of the cortical bone specimens as these grits are mostly responsible for the material

removal in the initial steps of grinding. Adopting a semi-regulated polishing procedure seemed to be the solution for the above problem. Thus the hand polishing technique was adopted for the 400 and 600 grit silicon carbide abrasive pads. The duration for which the hand polishing was carried out for these two steps were 1 minute and 5 minutes respectively with an Ecomet base speed of 100 rpm and 150 rpm respectively. Reducing the time step of the 400 grit grinding step to one minute is justifiable due to the fact that more than 75% of specimen removal occurs in the first 60 seconds of grinding itself. Followed by this, 800 grit and 1200 grit silicon carbide abrasive pads were used for machine polishing of the cortical bone specimens. These particular two steps had a duration of 15 minutes under a load of 1 lb. The base and the head speeds of the Ecomet 250 were maintained at 150rpm and 60rpm respectively. This particular grinding procedure gave flat specimens.

Following the grinding procedure adopted above, the polishing of the cortical bone specimens is adopted as below. 3µm, 1µm and 0.25 µm diamond suspension solutions used on a Texmet P for a duration of 20 minutes in each step under a load of 2lbs, with an Ecomet base and head speed at 300 rpm and 60 rpm respectively. Followed by these time steps, a final step using a 0.05µm alumina solution on microcloth under the same load, duration and speed conditions like that of the previous polishing steps were used. Branson 5800 Ultrasonic Cleaner was then employed to clean the specimens for a duration of 2 minutes each time after the specimens were ground and polished,

a procedure similar to the one adopted in all the above procedures. Last but not the least, a point to be noted is that, the 9µm polishing step is passed when it is realized that the 1200 grit silicon carbide paper is equivalent to 8µm polishing step. Thus this marks the final procedure adopted for polishing the porcine cortical bone specimens. The Figure 6.9, below represents the optical microscopy image of the Cortical Bovine Specimen thus obtained. As it can be seen, the surface is void of scratches and other polishing artefacts and the microstructure with osteons, cement lines haversian canals and lacunae can be clearly seen. Thus, as a result of the several advancements in the polishing procedures, an extensive procedure for polishing the porcine cortical bone specimens is formulated.

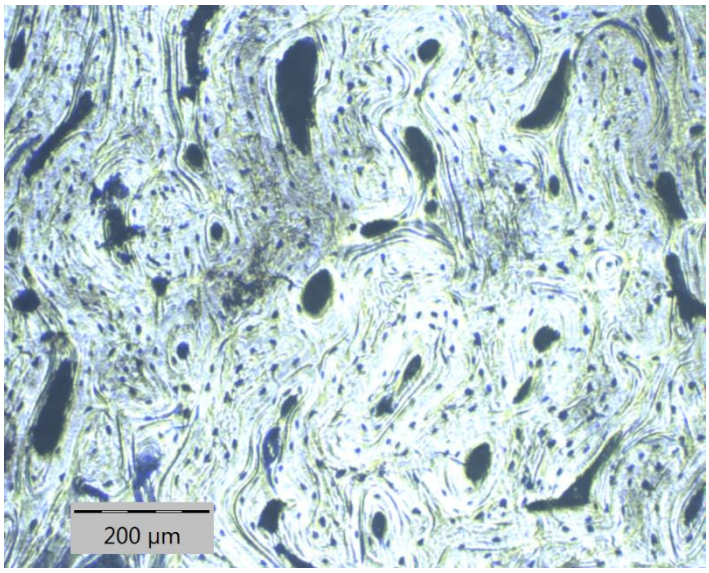

Figure 6.9 Image of the polished specimen using the protocol V.

The protocol V, which is the standardized polishing protocol for porcine bone specimens is summarized as follows in a tabular form.

Table 6.5 Summary of the Steps involved in polishing the porcine cortical bone specimens using Protocol V.

Grinding						
Step	Grit Size	Pad	Base Speed	Head Speed	Duration	Force
1	400 grit	Silicon Carbide	100 rpm	N/A	1 minutes	Hand Grinding
2	600 grit	Silicon Carbide	150 rpm	N/A	5 minutes	Hand Grinding
3	800 grit	Silicon Carbide	150 rpm	60 rpm	15 minutes	1 lb
4	1200 grit	Silicon Carbide	150 rpm	60 rpm	15 minutes	1 lb
Polishing						
1	3 microns	TexMet P	300 rpm	60 rpm	20 minutes	2 lbs
2	1 microns	TexMet P	300 rpm	60 rpm	20 minutes	2 lbs
3	0.25 microns	TexMet P	300 rpm	60 rpm	20 minutes	2 lbs
4	0.05 microns	Texmet P	300 rpm	60 rpm	20 minutes	2 lbs

The above discussed polishing procedure laid a starting step for polishing the bovine cortical bone specimens with relatively larger and pronounced microstructural features when compared to that

of the porcine cortical bone specimens. Adopting the above procedure as is resulted in bovine cortical bone specimens with surfaces possessing scratches and polishing artefacts showing the need to a further advancement of the procedure for these particular bovine bone specimens.

Protocol A

With the protocol V as the basis, certain changes were made for this protocol A. The Grinding steps remained as is, that is, hand grinding the specimens on the 400 grit and 600 grit Silicon Carbide papers for 1 minute and 5 minutes respectively with the Ecomet 250 base speed at 100 rpm and 150 rpm respectively. Followed by machine grinding of the specimens for 15 minutes at a load of 1 lb on the Micro cut S grit papers with the base and head speed of the Ecomet maintained at 150 rpm.

The polishing protocol witnessed changes in the loading and the duration. The specimens were polished using 3µm, 1µm and 0.25 µm diamond suspension solutions on Texmet P (Buehler, IL) for a duration of 60 minutes for each step at a load of 1lb with the base and head speeds of the Ecomet 250 at 300 rpm and 60 rpm respectively. Followed by a 0.05 µm alumina polishing on the Micro cloth for a duration of 60 minutes at 1lb and base and head speeds same as above. The surface thus obtained had shiny surfaces but the optical microscopy images and visualization using naked eye showed the surface needs to be polished even further to obtain relatively flat surfaces. This motivated for further improvements in the polishing procedure.

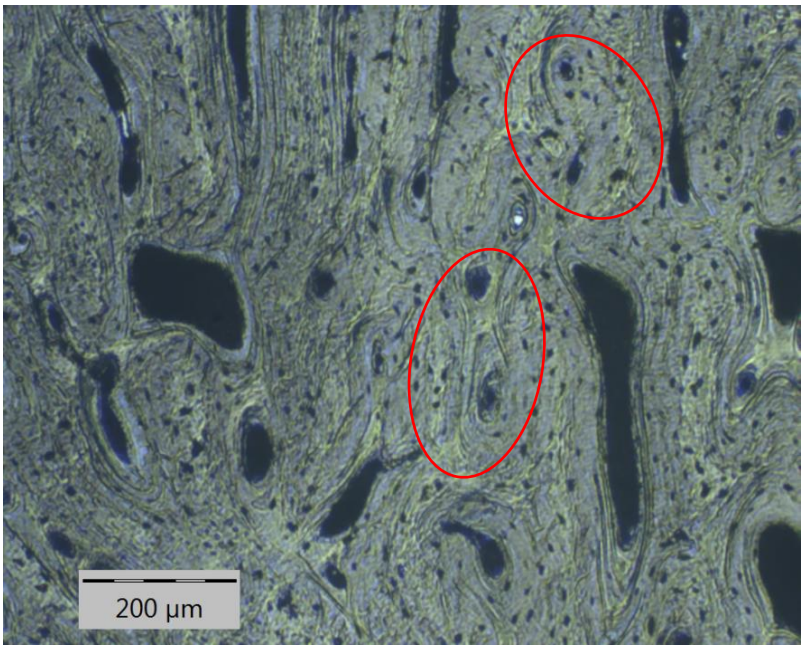

Figure 6.10 Bovine Cortical Bone polished using Protocol A. The shiny surfaces observed after polishing are marked in red.

Table 6.6 Summary of the Steps involved in polishing the porcine cortical bone specimens using Protocol A.

Grinding						
Step	Grit Size	Pad	Base Speed	Head Speed	Duration	Force
1	400 grit	Silicon Carbide	100 rpm	N/A	1 minutes	Hand Grinding
2	600 grit	Silicon Carbide	150 rpm	N/A	5 minutes	Hand Grinding
3	800 grit	Silicon Carbide	150 rpm	60 rpm	15 minutes	1 lb
4	1200 grit	Silicon Carbide	150 rpm	60 rpm	15 minutes	1 lb

Table 6.6 (cont.)

Polishing						
1	3 microns	TexMet P	300 rpm	60 rpm	60 minutes	1 lbs
2	1 microns	TexMet P	300 rpm	60 rpm	60 minutes	1 lbs
3	0.25 microns	TexMet P	300 rpm	60 rpm	60 minutes	1 lbs
4	0.05 microns	Texmet P	300 rpm	60 rpm	60 minutes	1 lbs

Protocol B

Protocol B is a slight variation of Protocol A. With the similar grinding steps as above, the step involving 0.05 µm polishing using a Micro cloth at 1 lb for a duration of 60 minutes encountered a change in the base speed from 300 rpm to 100 rpm with the head speed maintained at 60 rpm. This protocol resulted in the bovine cortical bone surface as shown in Figure 6.11. The surface still had certain polishing artefacts and darker areas which had to be removed by refining the procedure.

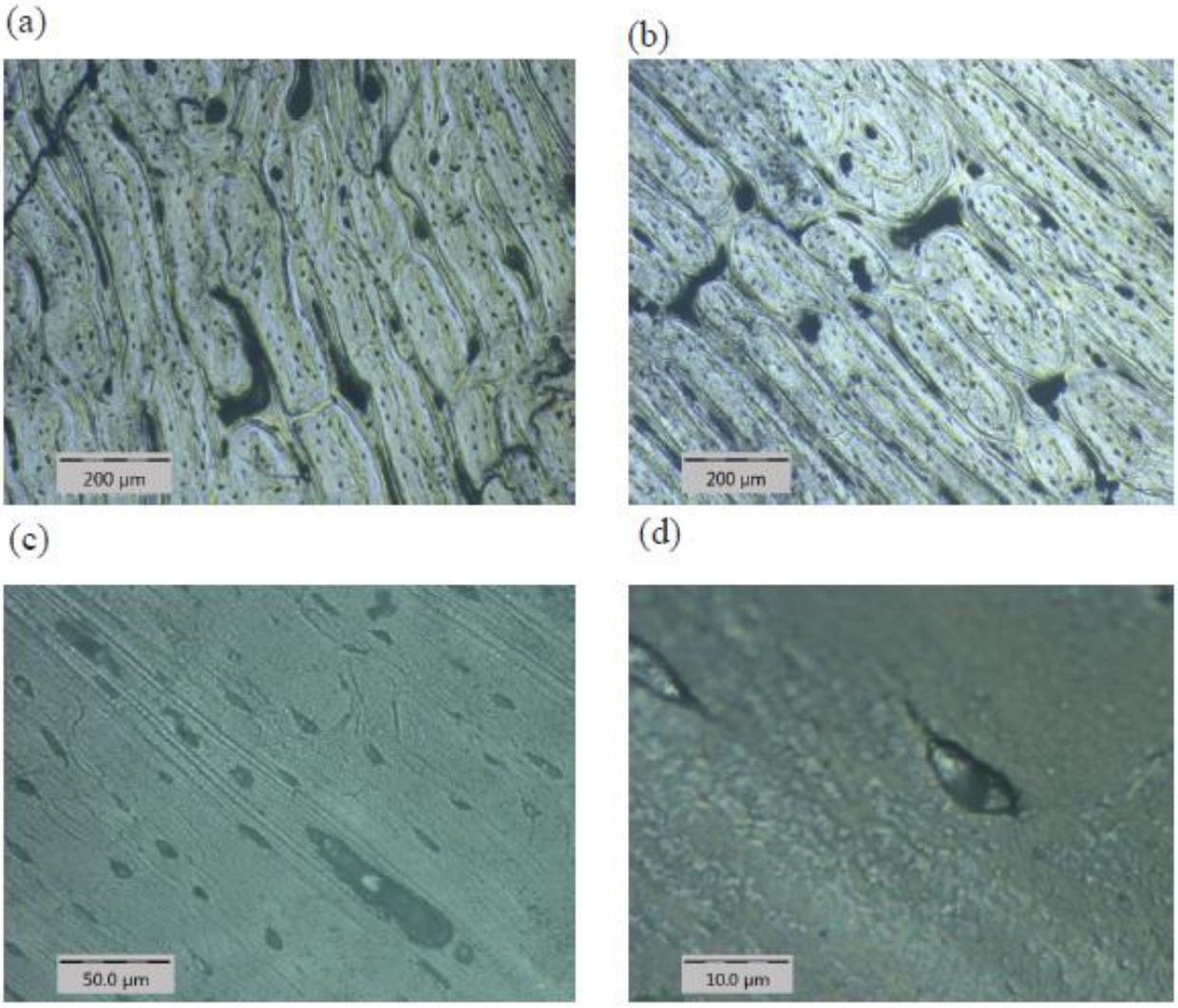

Figure 6.11 Optical Microscopy images of bovine cortical bone specimen polished using Protocol B (a) & (b) Optical micrograph at x5 zoom (c) Optical micrograph at x20 zoom (d) Optical micrograph at x100 zoom.

Table 6.7 Summary of the Steps involved in polishing the porcine cortical bone specimens using Protocol B.

Grinding						
Step	Grit Size	Pad	Base Speed	Head Speed	Duration	Force
1	400 grit	Silicon Carbide	100 rpm	N/A	1 minutes	Hand Grinding
2	600 grit	Silicon Carbide	150 rpm	N/A	5 minutes	Hand Grinding
3	800 grit	Silicon Carbide	150 rpm	60 rpm	15 minutes	1 lb
4	1200 grit	Silicon Carbide	150 rpm	60 rpm	15 minutes	1 lb
Polishing						
1	3 microns	TexMet P	300 rpm	60 rpm	60 minutes	1 lbs
2	1 microns	TexMet P	300 rpm	60 rpm	60 minutes	1 lbs
3	0.25 microns	TexMet P	300 rpm	60 rpm	60 minutes	1 lbs
4	0.05 microns	Texmet P	100 rpm	60 rpm	60 minutes	1 lbs

Protocol C

In several instances increasing grinding duration resulted in greater amount of material removal from the surface, but at the same time increasing the time for polishing procedure when conducted using optimum values of load, base and head speeds leads to better results. To explore this idea, a polishing procedure with increased time steps is adopted.

Grinding procedure remaining the same as that of the protocols A and B, the polishing procedure is now carried out for a duration of 90 minutes for each step at a load of 1 lb. with base and head speeds at 300 rpm and 60 rpm respectively for all the steps from 3 µm to 0.25 µm. The step involving the 0.05 µm alumina solution on the micro cloth was carried out for a duration of 120 minutes at a load value of 1 lb., with the base speed at 100 rpm and head speed at 60 rpm. This change in procedure encountered a problem with the step pertaining to micro cloth, as the removal of fibers from the cloth due to a prolonged polishing step lead to roughening of the material surface as shown in Figure 6.12.

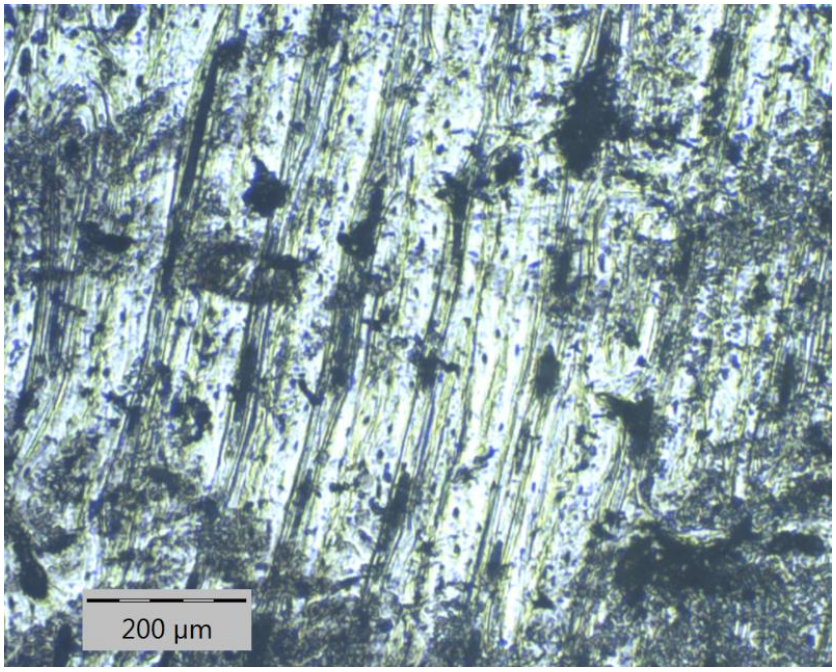

Figure 6.12 Bovine Cortical Bone polished using Protocol C.

The reason to conclude that it is the micro cloth step which created a problem was with the help of optical microscopy images captured at the end of each polishing step. For instance, Figure 6.13 shows an optical microscopy image of the bovine cortical bone specimen polished using protocol C upto 3 µm. The surface has expected number of scratches but didn't have any evident blackening of the surface.

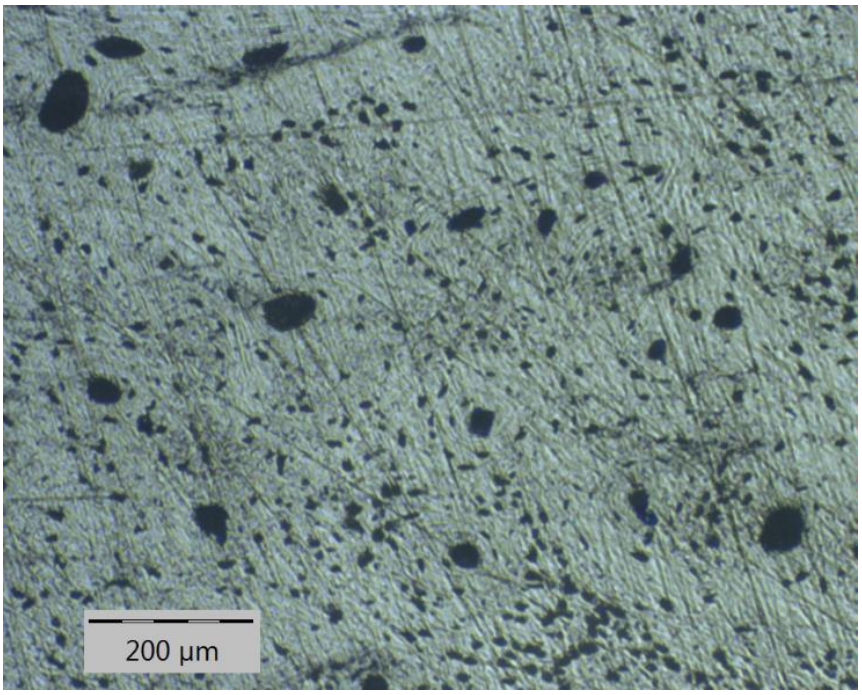

Figure 6.13 Bovine Cortical Bone polished up to 3 µm using Protocol C.

Table 6.8 Summary of the Steps involved in polishing the porcine cortical bone specimens using Protocol C.

Grinding						
Step	Grit Size	Pad	Base Speed	Head Speed	Duration	Force
1	400 grit	Silicon Carbide	100 rpm	N/A	1 minutes	Hand Grinding
2	600 grit	Silicon Carbide	150 rpm	N/A	5 minutes	Hand Grinding
3	800 grit	Silicon Carbide	150 rpm	60 rpm	15 minutes	1 lb
4	1200 grit	Silicon Carbide	150 rpm	60 rpm	15 minutes	1 lb
Polishing						
1	3 microns	TexMet P	300 rpm	60 rpm	90 minutes	1 lb
2	1 microns	TexMet P	300 rpm	60 rpm	90 minutes	1 lb
3	0.25 microns	TexMet P	300 rpm	60 rpm	90 minutes	1 lb
4	0.05 microns	Texmet P	100 rpm	60 rpm	120 minutes	1 lb

Protocol D

Thus, all the above protocols and their outcomes are used to develop this final polishing protocol. The final polishing procedure now consists of the same grinding steps as all the above protocols and polishing steps from 3 µm to 0.05 µm were carried out for a duration of 90 minutes each with

a load value of 1 lb having the base speeds of 300rpm for 3 µm to 0.25 µm polishing steps using the diamond suspension solution and 100rpm for the 0.05 µm alumina solution step.

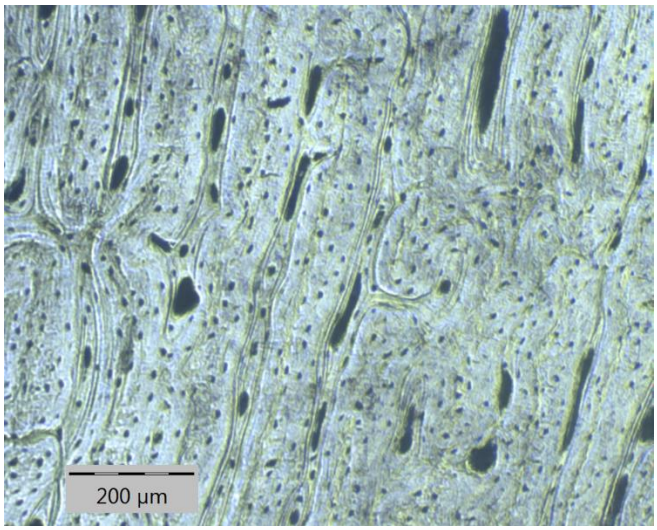

Figure 6.14 Bovine Cortical Bone polished using Protocol D.

The summary of the standardized polishing protocol for the bovine cortical bone is summarized in the following tabular form.

Table 6.9 Summary of the Steps involved in polishing the porcine cortical bone specimens using Protocol D.

Grinding						
Step	Grit Size	Pad	Base Speed	Head Speed	Duration	Force
1	400 grit	Silicon Carbide	100 rpm	N/A	1 minutes	Hand Grinding
2	600 grit	Silicon Carbide	150 rpm	N/A	5 minutes	Hand Grinding

Table 6.9 (cont.)

3	800 grit	Silicon Carbide	150 rpm	60 rpm	15 minutes	1 lb
4	1200 grit	Silicon Carbide	150 rpm	60 rpm	15 minutes	1 lb
Polishing						
1	3 microns	TexMet P	300 rpm	60 rpm	90 minutes	1 lb
2	1 microns	TexMet P	300 rpm	60 rpm	90 minutes	1 lb
3	0.25 microns	TexMet P	300 rpm	60 rpm	90 minutes	1 lb
4	0.05 microns	Texmet P	100 rpm	60 rpm	90 minutes	1 lb

The polished specimens were stored in the refrigerator at a temperature of -4^{o}C wrapped in a gauge soaked in HBSS until further testing.

6.2 Instrumented Micro Scratch Technique

Micro scratch technique, described in chapter 5, using the Anton Paar Micro scratch tester, CSM Instruments Inc., was adopted on the polished cortical bone specimens. A diamond Rockwell spheroconical indenter with a tip of radius 200 microns and apex angle of 136^{o} was used for the study. Specimen mounting procedure is the same as explained in section 5.2.2. The cortical bone specimen was placed on the friction table. Optical microscope was used to determine the scratch test locations. Followed by which, scratch tests were performed on the cortical bone specimens.

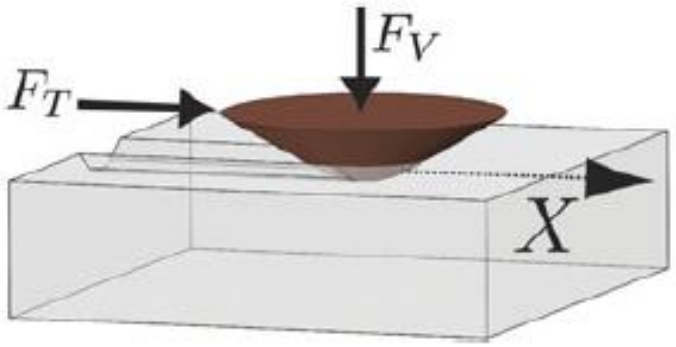

Figure 6.15 Schematic of the micro scratch technique performed using an axisymmetric probe. F_T and F_V represent the lateral and normal loads applied onto the probe (adopted from Akono et al., 2011).

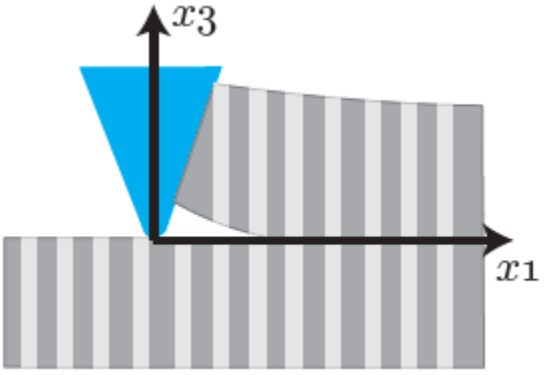

Figure 6.16 Schematic of scratch testing with the center of the axis coinciding with that of the probe center.

As discussed in chapter 5, CSM Micro scratch tester records the horizontal and vertical forces along with the corresponding penetration depth of the probe. The material that is tested is assumed to be linearly isotropic elastic and homogeneous. This enables the application of linear elastic fracture mechanics to determine the energy release rate (Akono et al., 2011).

In this model, the interface S, between the probe and the material is projected on a plane perpendicular to x_1 direction. This gives the area required in the fracture toughness measurements.

$$A = \int_s -n_x dS \tag{6.1}$$

where A is the area of the interface projected on the plane normal to x_1 and n_x is the direction cosine along the x_1 direction.

Further the perimeter of the probe, p, in contact with the material is noted as well. The non-linear fracture mechanics theory incorporates the idea that crack propagates when the energy release rate G equals that of the fracture energy release rate G_f (Akono and Randall, 2011; Akono and Ulm,2012; Akono et al., 2011). The energy release rate is computed using a path independent J- integral.

$$G = \frac{1}{p}\oint_s [\varphi n_x - T\frac{\partial \varepsilon}{\partial x}]dS \tag{6.2}$$

where p is the probe perimeter. ε is the linear elastic plane strain tensor. T is the stress vector at the blade material interface. Ψ is the elastic free energy density which is half of the stress tensor ahead of the probe. The stress tensor ahead of the probe can be given by:

$$\underline{\underline{\sigma}} = \frac{F_T}{A}\underline{e_x} \otimes \underline{e_x} + \sigma_{yy}\underline{e_y} \otimes \underline{e_y} \tag{6.3}$$

As discussed earlier scratch test results in a scratch groove which consists of plastic deformation and fracture process. In the model, inelastic plastic deformation though accounted for, is considered to be confined to the crack tip. Thus, at the probe tool interface the behavior is elastic and thus for the computation of the *J*-integral linear elastic fracture mechanics could be used (Akono and Ulm, 2011; Akono and Ulm, 2014). Using the above calculations, we determine the fracture toughness of the material given by the following expression,

$$K_c = \frac{F_T}{\sqrt{2pA}} \tag{6.4}$$

where $K_c = \sqrt{G_f E/(1-\vartheta^2)}$, the plane strain fracture toughness. Furthermore, this equation holds good if the dominant failure mechanism is a brittle fracture. To quantitatively assess the extent of brittle fracture and the ductile to brittle transition if any, the most popular size effect law, described below is used.

Size Effect Law

Classical elastic and plastic fracture mechanics theories describe that the nominal strength, σ_N is independent of the structure size, D when we consider the structures with similar geometry. Any deviation from the above occurrence is the Size Effect Law (Bazant, 1999).

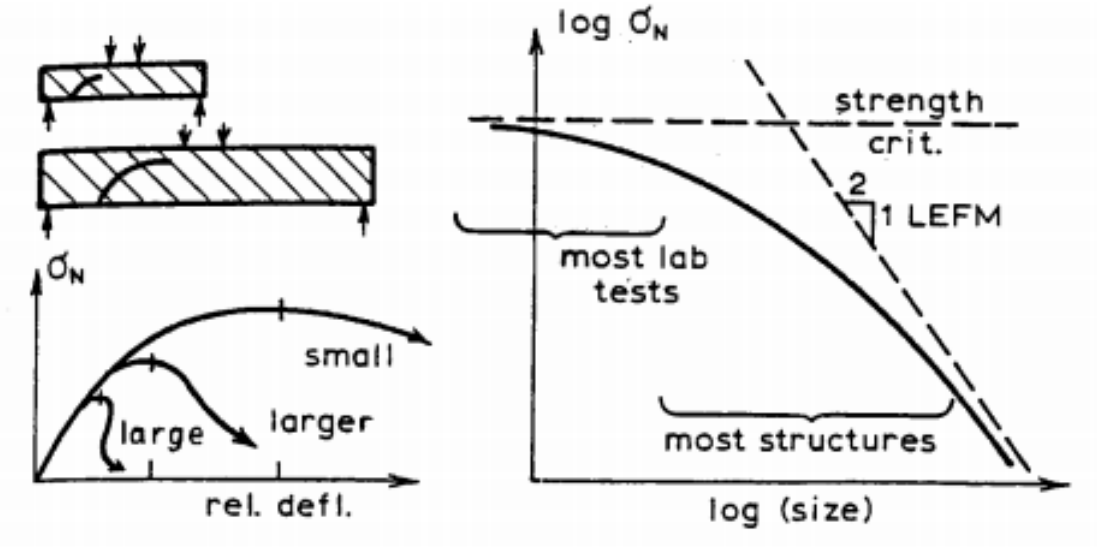

Figure 6.17 Fracture Mechanics Size Effect for different sizes of geometrically similar structures (adopted from ACI Committee 446 1992).

The conventional definition of strength is the nominal stress at the peak load. Further, nominal stress is defined proportional to the ratio of load to the cross-sectional area of the member (ACI Committee 446, 1992).

$$\sigma_N = c_N \frac{P}{bD} \quad \text{(2D similarity)} \tag{6.5}$$

$$\sigma_N = c_N \frac{P}{D^2} \quad \text{(3D similarity)} \tag{6.6}$$

where P is the applied load, b is the thickness of the two-dimensional structure, D is the characteristic dimension of the specimen and c_N is the coefficient for convenience. At the peak load, P_u the nominal strength is σ_{Nu} (Bazant and Planas, 1997).

Size effect consists of variation of the nominal strength σ_{Nu} with that of the dimension D. Figure 6.17 is the most widely used plot to describe the size effect. In this Figure, we see two asymptotes corresponding to strength criterion and Linear Elastic Fracture Mechanics (LEFM) and the variation of σ_{Nu} with D are shown. The equation of the simplest size effect law which best suits the plot is given in the equation below (Bazant, 1984).

$$\sigma_{N_u} = \frac{B f_t'}{\sqrt{1+D/D_0}} \tag{6.7}$$

where f_t is the tensile strength of the material, B is the dimensionless constant, D_o is the constant with the dimension of length. B and D depend on the fracture properties of the material, geometry (shape) of the structure, but not on the size of the structure.

Strength criterion would be sufficient to explain the crack initiation in the material, but the necessity to consider the energy absorbed for the crack formation signifies the importance of development of the energetic size effect law. The size effect law has been in practice for several decades and is widely accepted for the analysis of the failure behavior for several quasi brittle materials such as concrete, tough steels, rocks and bone. This size effect law is applied to the scratch tests as well (Akono, 2016; Akono et al, 2014).

Energetic size effect law extended to the micro scratch technique is applied on to the cortical bone specimens. As discussed in sections 5.2 and 6.2, the microscratch technique uses a

conical probe to perform the scratches on the material surface. A progressive load is applied on to the probe.

For a conical probe with progressive loading, the ultimate nominal strength (here s_N) is given by the equation,

$$\sigma_N = \frac{F_T}{d^2 \tan\theta} \tag{6.8}$$

where θ is the apex angle of the probe and d is the probe dimension. The nominal structural size is given by $D = \frac{d \sin\theta}{4}$ (Akono, 2016). Thus, accordingly for a failure which is dominated by fracture, $F_T \alpha d^{3/2}$ and for a failure dominated by plastic flow it is expected that, $F_T \alpha d^2$. K_c derived from the size effect law is given by,

$$K_c = B f_t' D_0 \tag{6.9}$$

6.2.1 Calibration

To calculate the fracture properties of cortical bone specimens, the theory suggests that the scratch probe dimensions are required. The scratch probe function 2pA is determined by performing the scratch tests on a reference material. In this study, Lexan 9034, a polycarbonate material of known properties is used as the standard reference material. Lexan 9034 specimens must be prepared with utmost care to obtain clean and dry surfaces without any impurities. The specimens were first

cleaned in a 1% Alconox solution for a duration of 5 minutes in the ultrasonic cleanser. Later, the lexan specimens are cleaned in deionized water for a duration of 5 minutes in the ultrasonic cleanser. The specimens are then exposed to jet of ionized water on all their faces. Followed by this, the lexan specimens were oven dried at 250^{o}F for a duration of 24 hours. The specimens removed from the oven are now cooled at room temperature for a duration of 24 hours (Akono and Ulm, 2014).

An advanced scratch map was selected for the testing procedure. A pre-scan was selected to perform the initial surface examination of the specimen. This initial scanning was performed at a scanning load of 30mN. Thus, panorama was enabled as well. In addition, a progressive normal load from 30mN to 30N was applied on to the specimens at a loading rate of 60N/min. A scratch speed of 6 mm/min and a scratch length of 3mm were adopted. Furthermore, as described in chapter 5, selection of the panorama mode as well enables in capturing the scratch grove post the scratch test. Figure 6.17 shows the scratch grove on Lexan 9034 and table 6.10 shows the parameters of the micro scratch test.

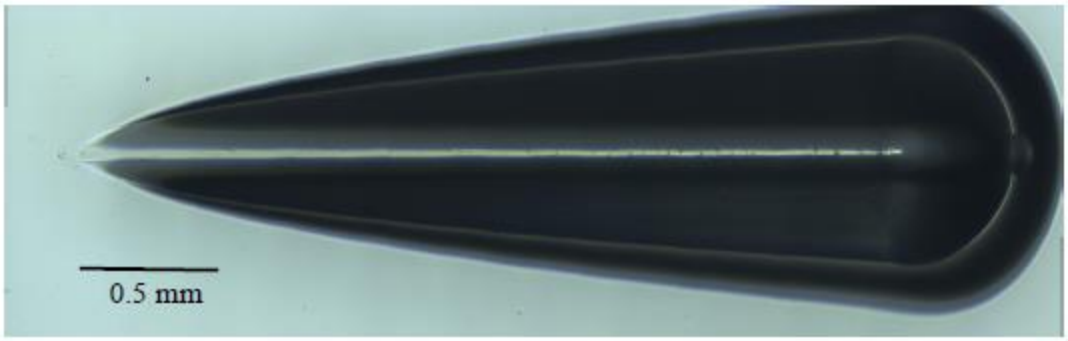

Figure 6.18 3 mm long scratch test carried out on Lexan at a loading rate of 60 N/min.

Table 6.10 Parameters for the scratch test carried out on Lexan.

Scratch Type	Linear Scratch
Start load (N)	0.03
End load (N)	30
Scanning Load (N)	0.03
Loading Rate (N/min)	60
Scratch speed (mm/min)	6
Scratch Length (mm)	3

The calibration data is analyzed using a MATLAB routine which gives the probe shape function as shown in Figure 6.18. The fit is a third order expression, with the first coefficient corresponding to the cone behavior, second corresponding to the sphere and the third to that of a flat punch.

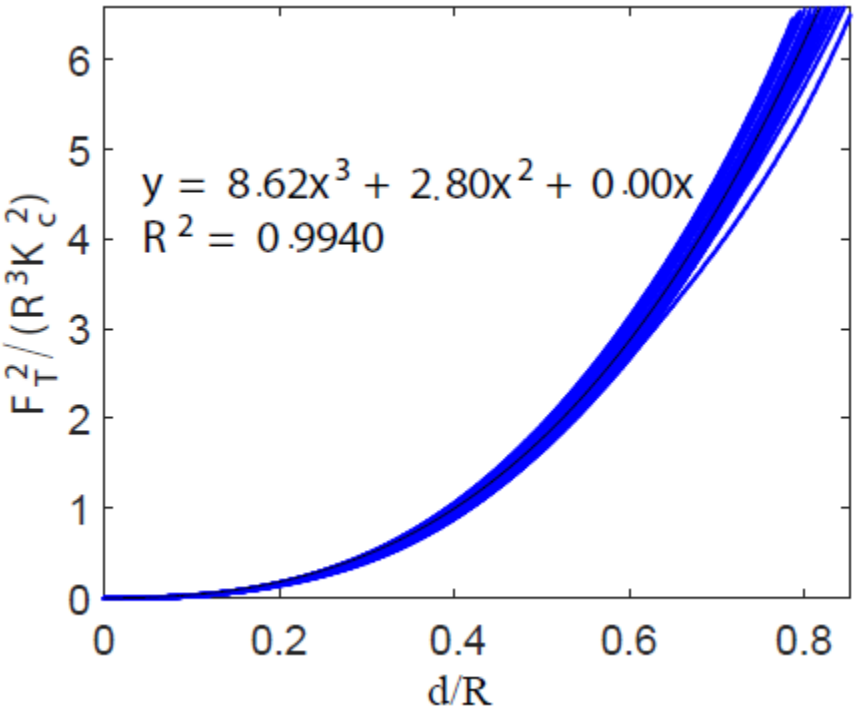

Figure 6.19 Calibration of the Lexan 9034 specimen.

6.2.2 Cortical Bone

The micro scratch tests are carried out on the polished and prepared cortical bone specimens. In this study, the porcine specimens are tested in the short longitudinal direction as shown in Figure 6.20. Whereas, the bovine cortical bone specimens were tested along the short longitudinal and longitudinal transverse directions.

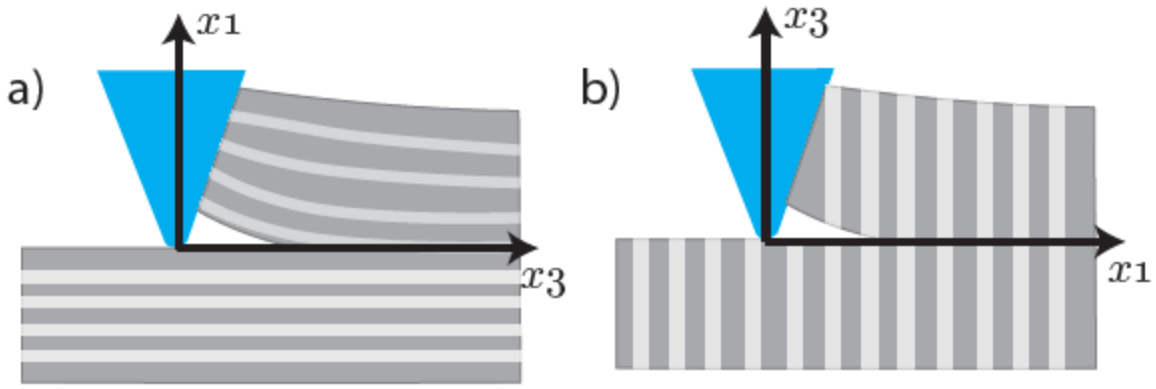

Figure 6.20 Schematic showing the two orientations of the micro scratch tests on the cortical bone specimens (a) Short longitudinal direction or the transversely cut specimens (b) Longitudinal transverse direction or the longitudinally cut specimens.

Furthermore, the scratch tests performed on the cortical bone specimens correspond to a linear progressive load from 30 mN to 30N. The loading rate was constant at 60 N/min. The scratch speed was 6 mm/min with a scratch length corresponding to 3 mm. Figures 6.22 to 6.27 show the representative scratch test for the porcine and bovine cortical bone specimens. The penetration depths for the scratch tests on the porcine transverse specimens were in the range of 90-120 µm. The penetration depths for the scratch tests on the bovine specimens were in the range of 80-130 µm. The penetration depths show us that we are probing the mesoscopic and microscopic features such as osteons, haversian canals and cement lines through the micro scratch tests.

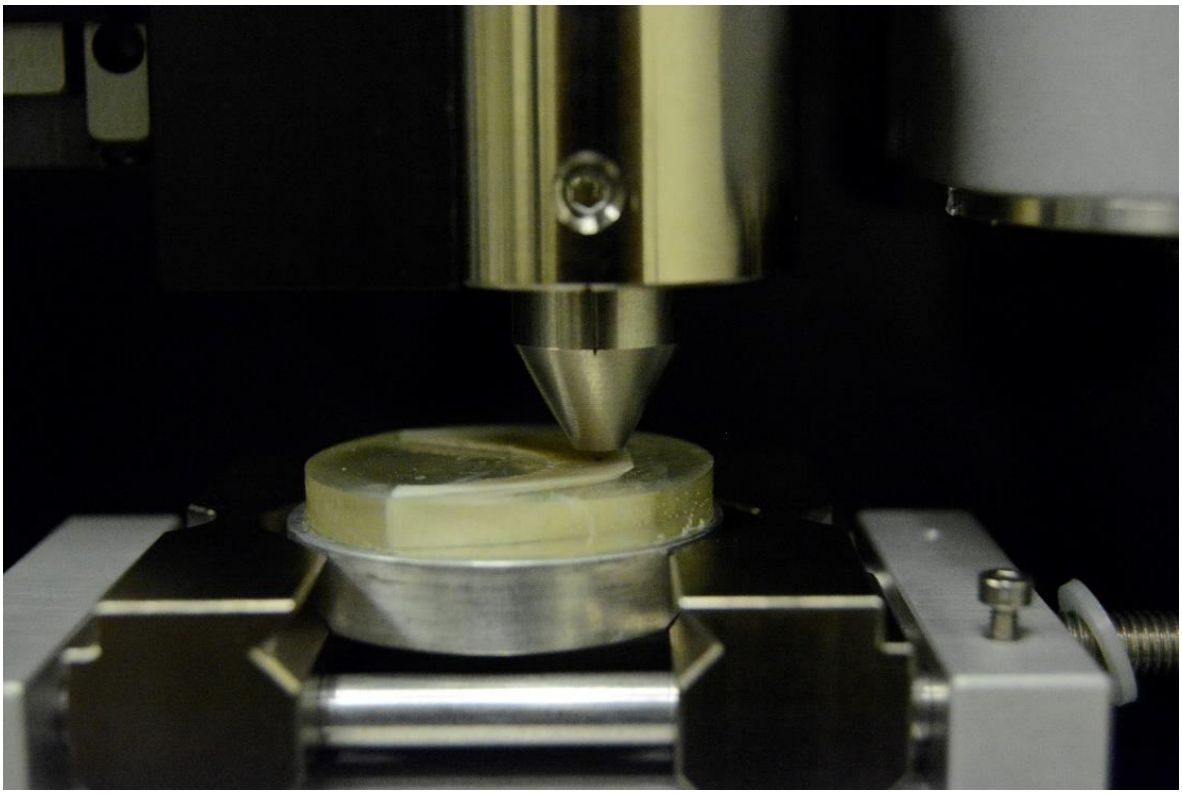

Figure 6.21 Micro scratch test performed on cortical bone specimens (Credits: Ange-Therese Akono, Amrita Kataruka and Kavya Mendu, UIUC, 2017).

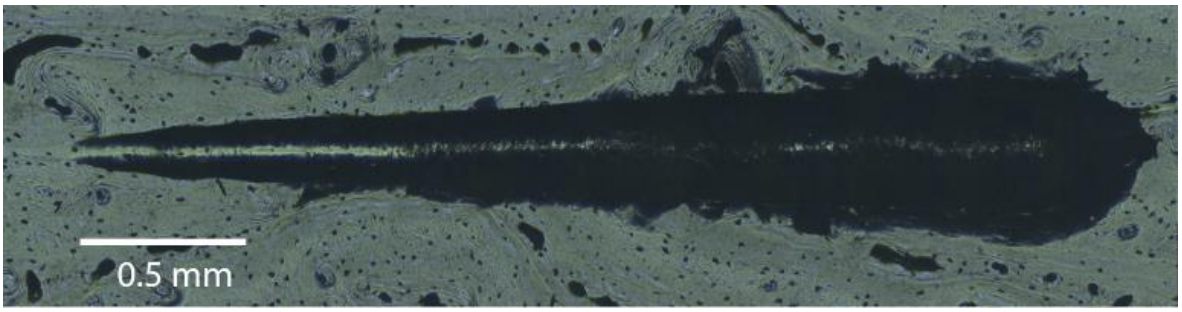

Figure 6.22 Panorama of the scratch test on the transverse (SL) porcine cortical bone specimen. The scratch groove is 3mm long and loading rate is 60 N/min.

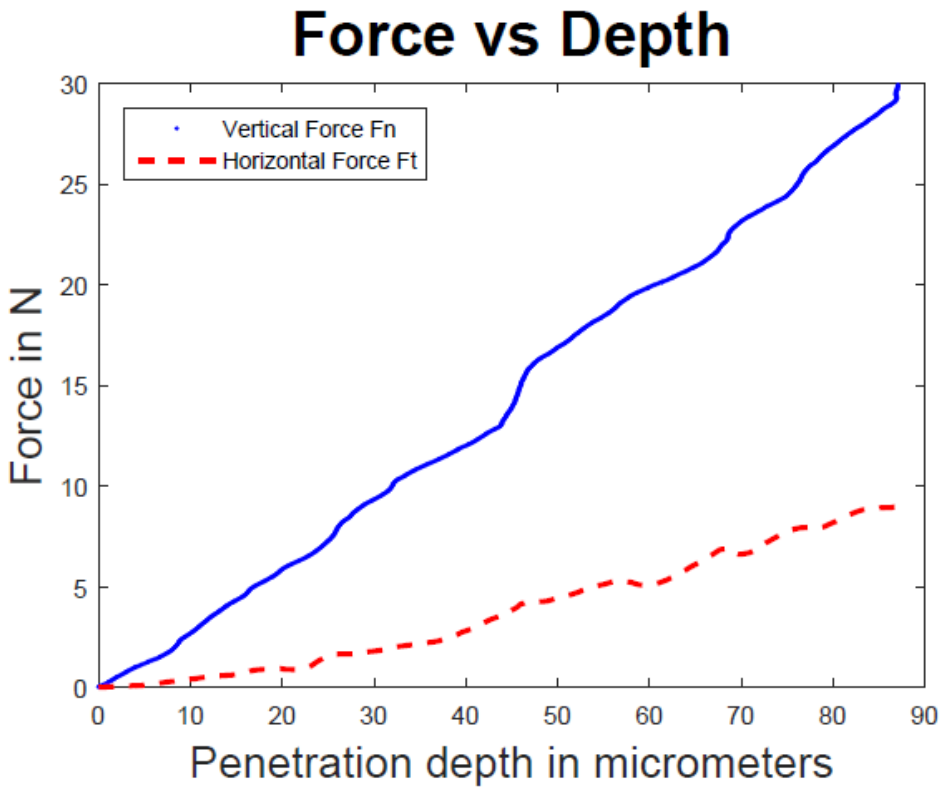

Figure 6.23 Force versus penetration depth of a representative scratch test on the transverse (SL) porcine cortical bone specimen.

Figure 6.24 Panorama of the scratch test on the transverse (SL) bovine cortical bone specimen. The scratch groove is 3mm long and loading rate is 60 N/min.

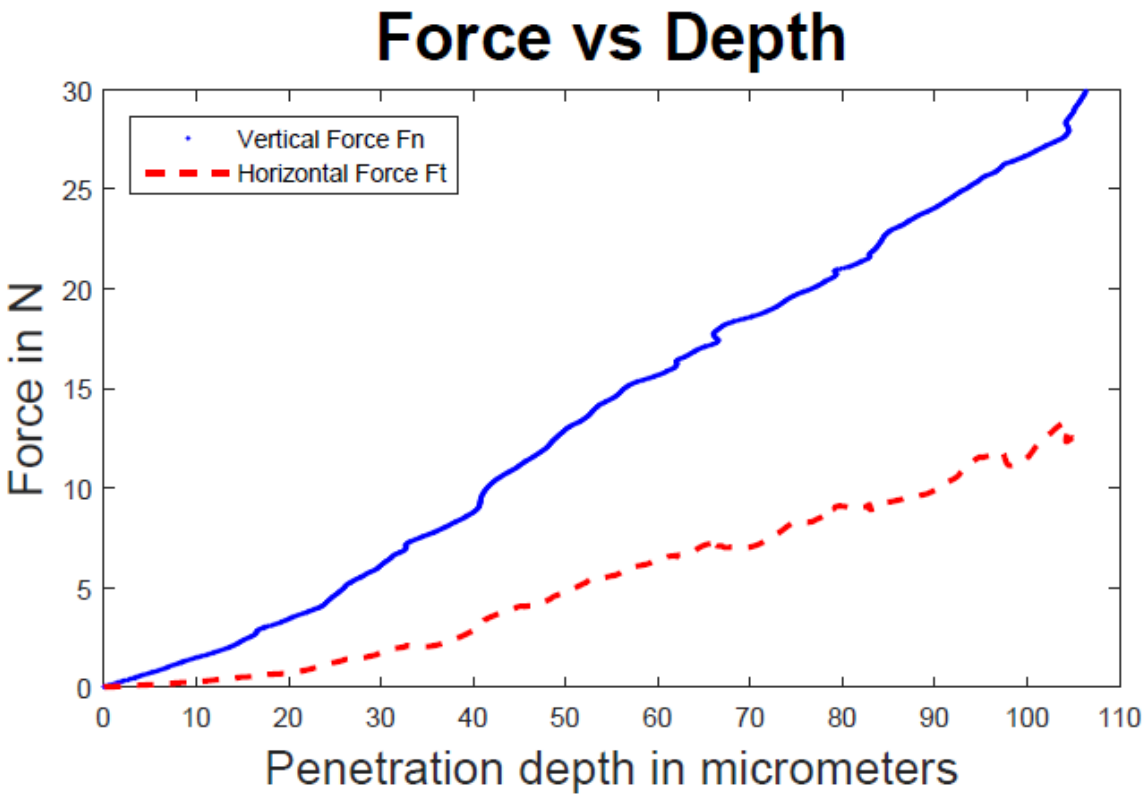

Figure 6.25 Force versus penetration depth of a representative scratch test on the transverse (SL) bovine cortical bone specimen.

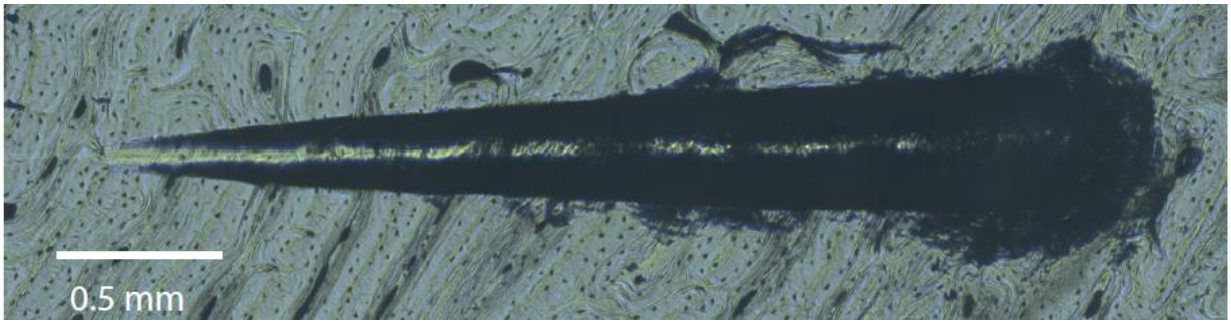

Figure 6.26 Panorama of the scratch test on the longitudinal (LT) bovine cortical bone specimen. The scratch groove is 3mm long and loading rate is 60 N/min.

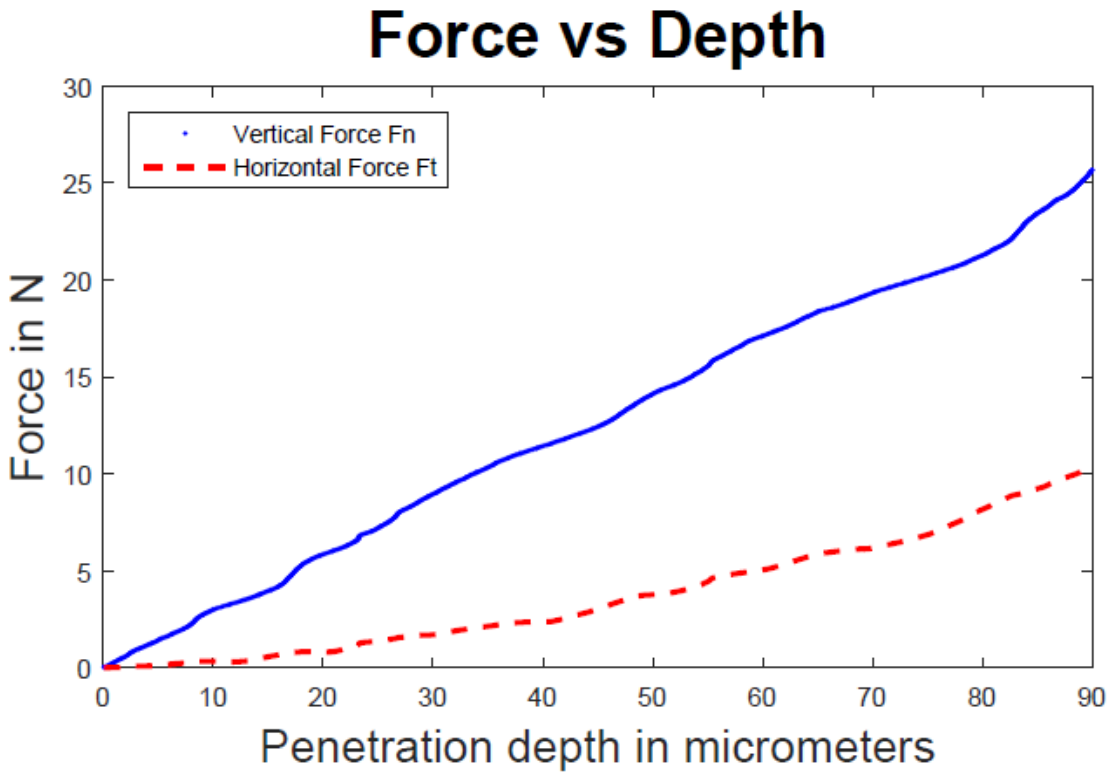

Figure 6.27 Force versus penetration depth of a representative scratch test on the longitudinal (LT) bovine cortical bone specimen.

6.3 Analysis

The force penetration depth curves obtained from the micro scratch tests were analyzed using the dimensional analysis and non-linear fracture mechanics theory discussed in section 6.2 (Akono and Ulm, 2011; Akono et al., 2011; Akono et al., 2012; Akono et al., 2014; Akono and Ulm, 2014). Based on the non-linear fracture mechanics model, MATLAB scripts were generated and the data from the experiments is introduced into these scripts.

Prior to the occurrence of fracture process, there would be plastic dissipation as discussed earlier in section 6.2 (Yan et al., 2007). As the penetration depth increases the fracture process commences. The plot corresponding to the *J*-integral force scaling of the calibration data on Lexan 9034 polycarbonate is shown in Figure 6.27. Figure 6.28 shows the force scaling plot of micro scratch tests performed on the transverse porcine cortical bone specimen.

The force scaling plots of the cortical bone specimens show a high initial Kc value due to the plastic dissipation. Further, the plots clearly show a ductile to brittle transition. The Kc value corresponding to the brittle fracture is reported on each of the force scaling plots.

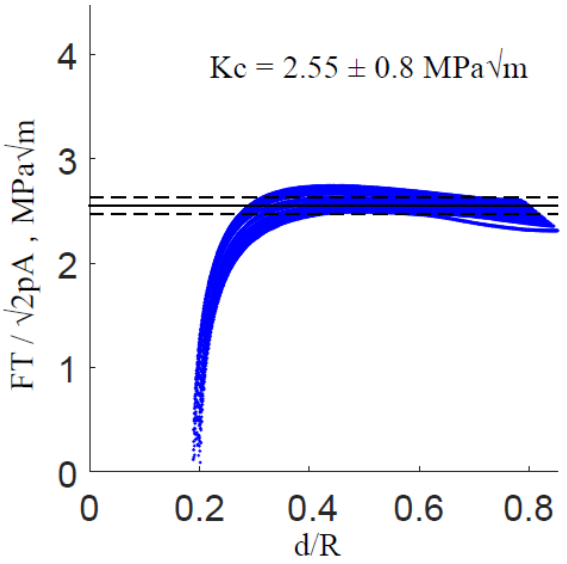

Figure 6.28 Force scaling plot of the calibration tests performed on Lexan 9034. 3mm long scratches performed at a loading rate of 60 N/min.

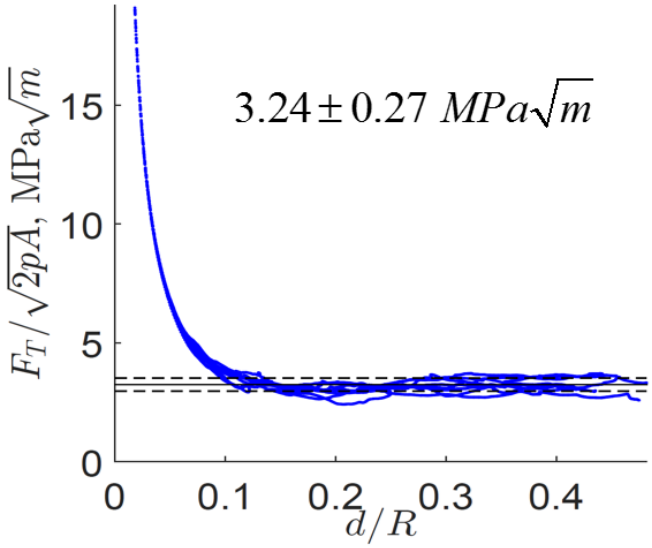

Figure 6.29 Force scaling plot of the micro scratch tests performed on transverse porcine cortical bone specimens. 3mm long scratches performed at a loading rate of 60 N/min.

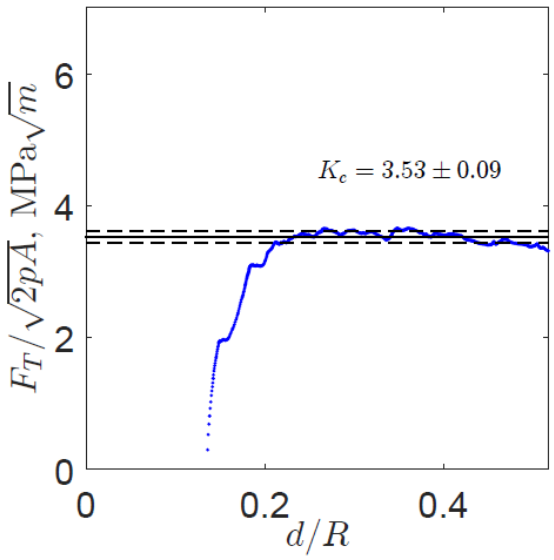

Figure 6.30 Representative *J*-integral force scaling plot of the micro scratch tests performed on transverse bovine cortical bone specimens. 3mm long scratches performed at a loading rate of 60 N/min.

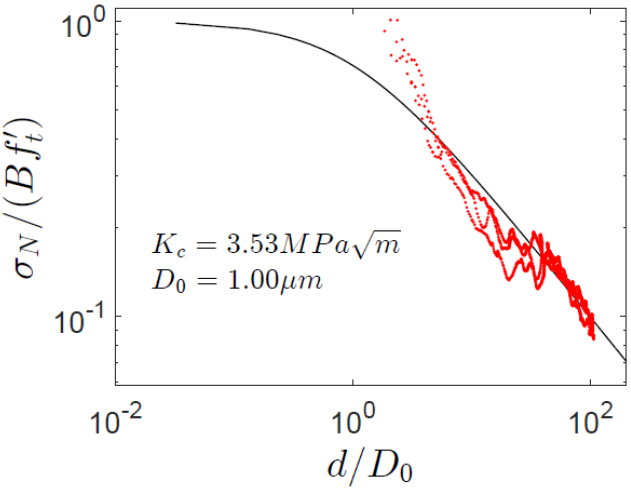

Figure 6.31 Fracture toughness obtained using size effect law. Plot corresponding to the micro scratch tests performed on transverse bovine cortical bone specimens. 3mm long scratches performed at a loading rate of 60 N/min.

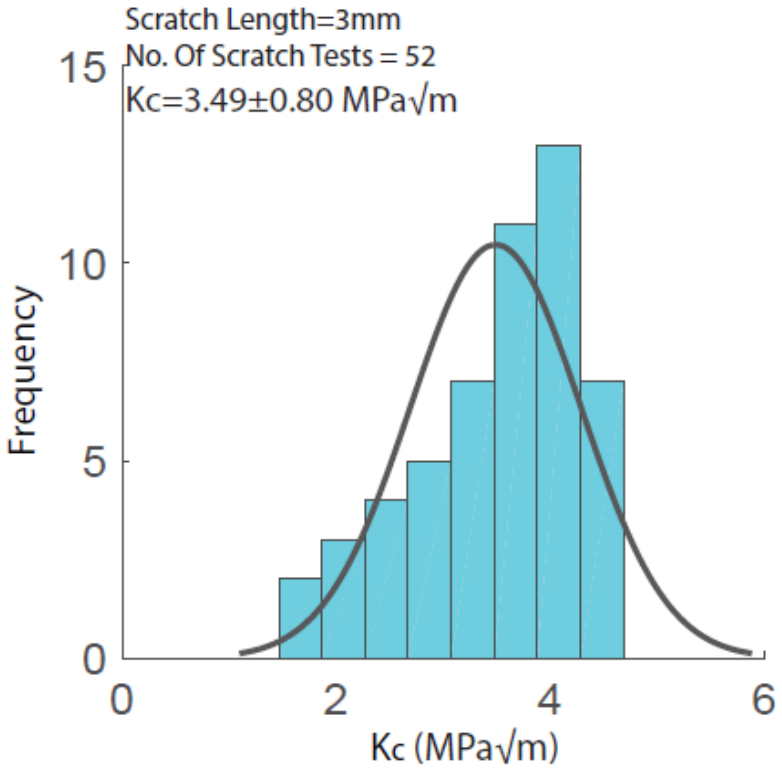

Figure 6.32 Histogram for the fracture toughness values obtained from the force scaling micro scratch tests on the transverse porcine cortical bone specimens. 3mm long scratches and a loading rate of 60N/min were used.

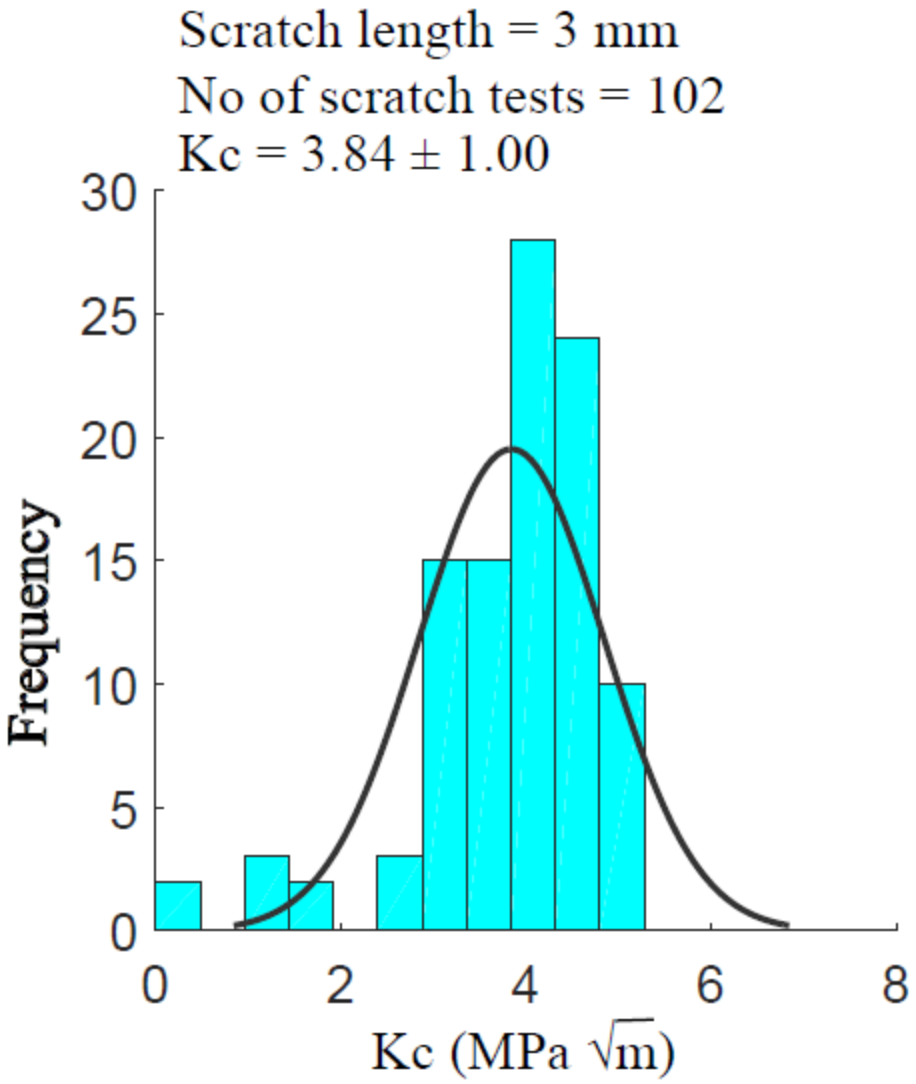

Figure 6.33 Histogram for the fracture toughness values obtained from the force scaling micro scratch tests on the transverse bovine cortical bone specimens. 3mm long scratches and a loading rate of 60N/min were used.

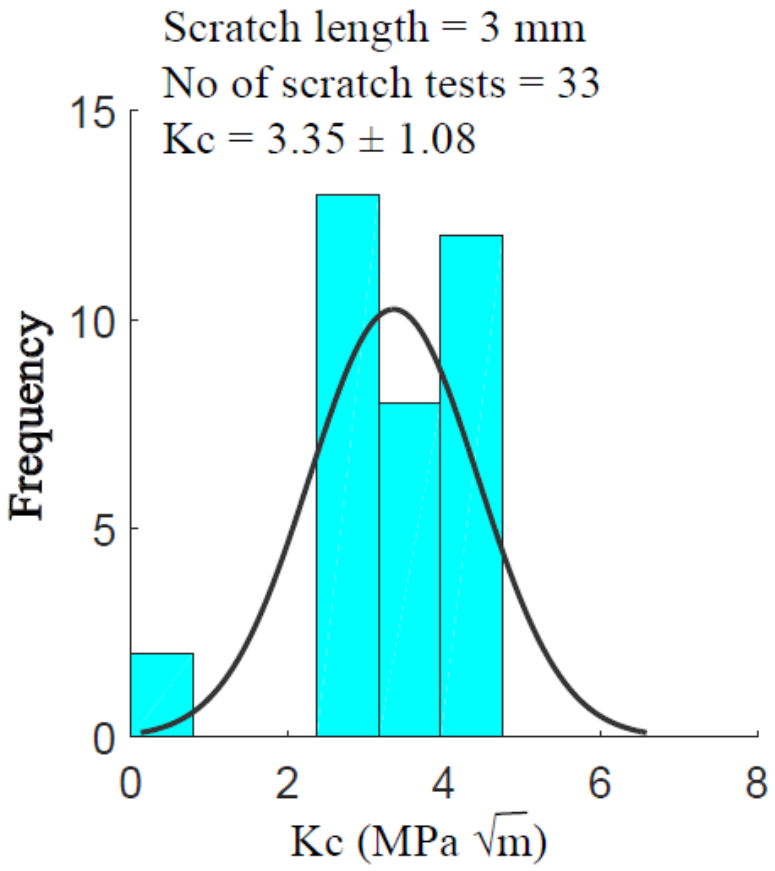

Figure 6.34 Histogram for the fracture toughness values obtained from the force scaling micro scratch tests on the longitudinal bovine cortical bone specimens. 3mm long scratches and a loading rate of 60N/min were used.

SEM Investigation of Fracture Micro Mechanisms

The cortical bone specimens with the scratch grooves were observed under the scanning electron microscopes JEOL 6060LV General Purpose Scanning Electron Microscope at the Frederick Seitz

Material Research Laboratory and Philips XL 30 ESEM FEG at the Beckman Institute at University of Illinois at Urbana Champaign. The specifications and the parameters used for the study are as described in chapter 3.

Uncoated cortical bone specimens were examined under the scanning electron microscopes and the Figures 6.35 to 6.37 show the scratch grooves. Semicircular cracks were observed as shown in the Figure 6.37. This is because of the crack development along the cement lines which are concentric. The micro mechanisms such as crack deflection, crack bridging, micro cracking, flaking and chipping were observed and marked on the images. Chipping and flaking of the material is observed in the scratch groove due to the fracture of the cortical bone specimens.

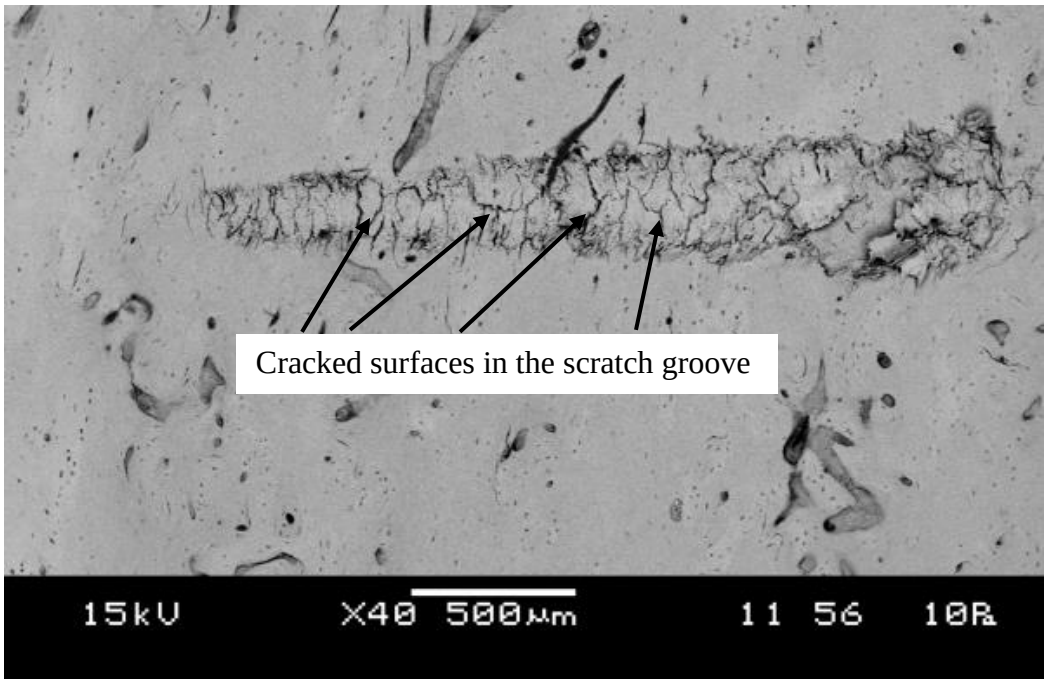

Figure 6.35 Scanning electron microscopy image of 3mm long scratch groove performed on the transverse bovine cortical bone specimen.

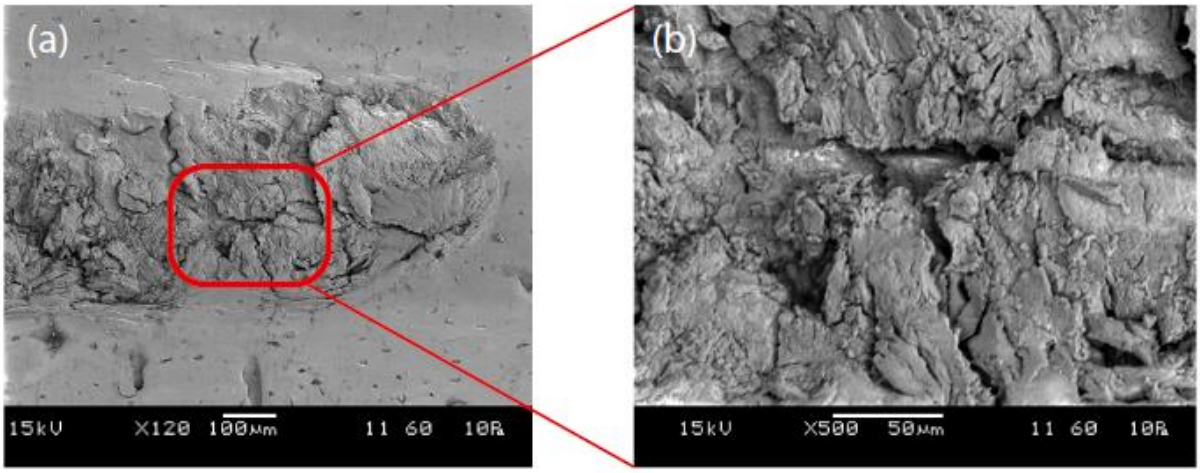

Figure 6.36 Scanning electron microscopy of the scratch groove in the transverse (SL) porcine specimen (a) magnification is 120x and (b) magnification is 500x which shows chipping of the material.

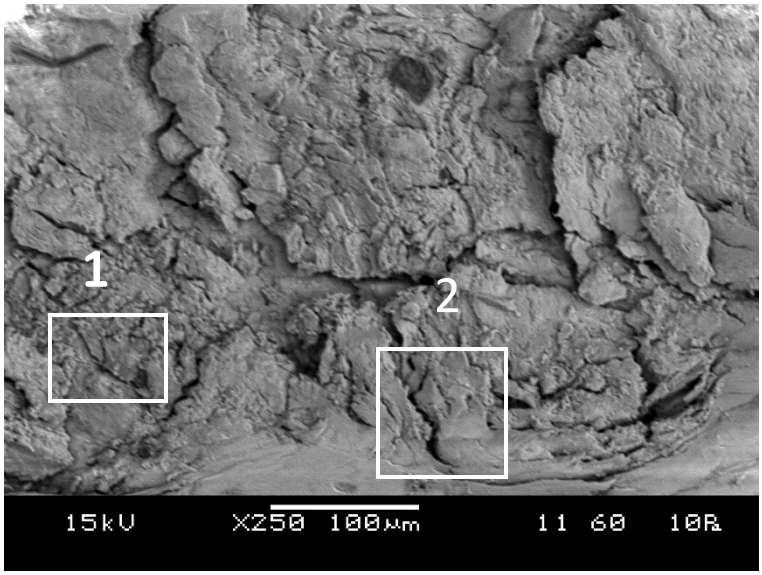

Figure 6.37 Scanning electron microscopy of the scratch groove in the transverse (SL) porcine specimen (1) crack bridging (b) crack deflection were the micro mechanisms besides micro cracking observed in this micrograph.

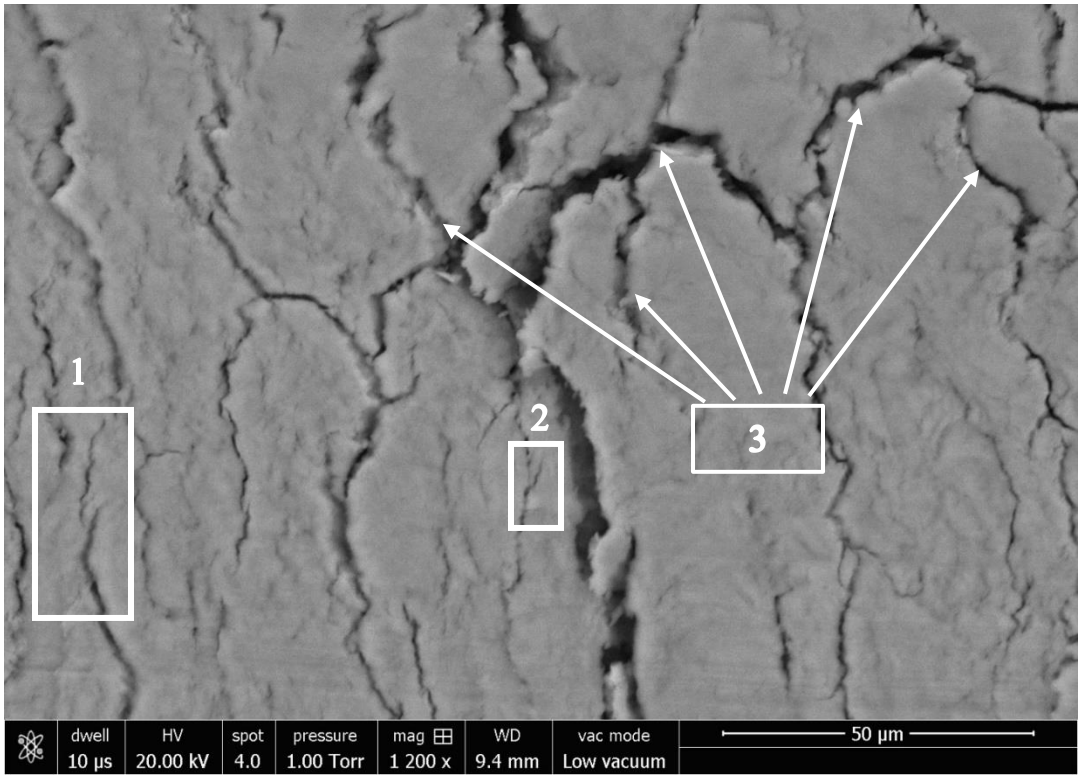

Figure 6.38 Environmental scanning electron microscope of transverse cortical bone (1) Crack bridging (2) Crack deflection and (3) micro cracking.

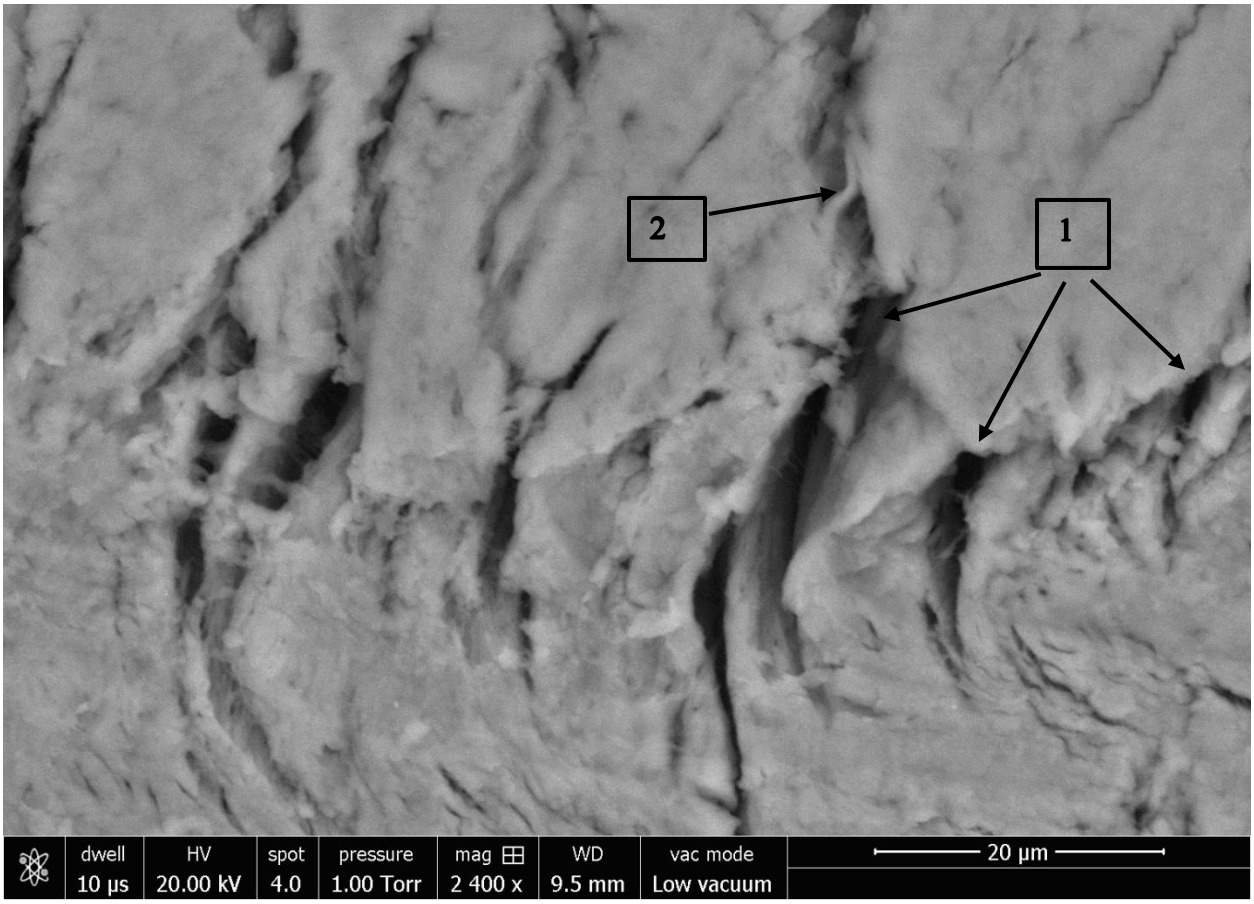

Figure 6.39 Environmental scanning electron microscopy on transverse (SL) swine cortical bone specimen showing the semicircular cracks of the scratch groove (1) Arc shaped cracked surfaces (2) fiber bridging.

6.4 Chapter Summary

This chapter describes the application of micro scratch technique to determine the fracture properties of the porcine and bovine cortical bone specimens. Thus, the fracture toughness of the

short longitudinal (transverse specimens) porcine cortical bone specimens and short longitudinal (SL) and longitudinal transverse (LT) bovine cortical bone specimens were reported based on the theory developed by Akono and Ulm (2011 and 2014). The average values of the tests reported through the histograms show anisotropy associated with the transverse and longitudinal directions. Furthermore, the fracture toughness values obtained through the micro scratch tests on the cortical bone specimens fall within the range of the values reported in the literature in chapter 2. In addition, the scanning electron microscopy images show the various intrinsic toughening mechanisms such as micro cracking, crack deflection and crack bridging as expected from the literature survey.

CHAPTER 7

INTRODUCTION TO NANO INDENTATION

7.1 Indentation Test

With the increase in need to understand material properties at smaller length scales, conventional uniaxial testing methods needed an upgrade as well. This led to the development of indentation technique. Hardness of the material quantifies its resistance to plastic deformation. As discussed in section 2.2 indentation methods help in the determination of this material property named hardness (Tabor, 1951; David and Augsburger, 1977; Hiestand and Smith, 1984). As discussed earlier in section 5.1, several scales such as Brinell Hardness scale, Rockwell Hardness scale and Vickers Hardness scale have been developed over the decades.

Indentation techniques require the surface of the material to be tested to have a surface roughness smaller than that of the indentation, so that the surface roughness effects can be eliminated. In addition, this enables the practical application of indentation tests on the materials which are not necessarily smooth by choosing suitable indenter dimensions. However, effect of strain hardening is observed when performing the indentation tests to determine the material properties. Strain hardening is the phenomenon of material strengthening due to plastic deformation. This occurs due to the dislocations within the crystal structure of the material.

However, strain hardening effect is said to reduce when performing smaller indentations (Tabor, 2000). Indentation techniques also can be classified into macro indentation, micro indentation and nanoindentation tests.

Macro indentation tests corresponds to higher loads applied onto the indenter. They can have the maximum force as high as 40 N and the indent has a length scale of up to few millimeters (Patel and Sun, 2016). Vickers hardness test which has a wide hardness scale quantifies hardness using Vickers hardness number (HV) and is one among the macro indentation tests. Other macro indentation tests include Brinell Hardness test which measures Brinell Hardness Number (HB), Rockwell Hardness test (HR), Knoop Hardness test for small areas, Meyer Hardness test, Janka Hardness test, Shore Hardness test and Barcol Hardness test. Vickers indentation test, Brinell indentation test and Rockwell hardness test have been explained in detail with schematics in section 5.1 of chapter 5.

Micro indentation tests operate at lower loads compared to that of the macro indentation tests. However, they have loads up to 2N. In the micro indentation tests, a diamond indenter of known geometry is applied onto the material whose properties are to be found out. Furthermore, the indents thus produced range up to few micrometers on the length scale, for example 50μm. The micro indentation tests require the surfaces to be polished prior to the testing. Vickers hardness test which quantifies hardness using HV and Knoop hardness test which measures HK are the most

commonly used micro hardness tests. Hardness number is the ratio of applied force to the surface area of the indent, thus having the units of pressure. Vickers micro indentation is similar to the macro indentation described in section 5.1. Vickers micro indentation uses the diamond pyramid tip as well and the hardness number is computed using the average of the two diagonals as well. On the other hand, Knoop test uses elongated pyramid shaped tip to create the indents.

Nanoindentation is a type of indentation test which enables the measurement of mechanical properties of materials at very small length scales (Willems et al., 1993). The tip used in the nanoindentation are small and precise. Furthermore, it provides the indentation area is very small and ranges only up to few square micrometers or nanometers. Previous indentation techniques used to measure the indentation area directly using light microscopy. Thus, for a given load the hardness used to be measured using the following formula. The underlying principle is that smaller indents corresponds to harder material and larger indents to softer material (Tabor, 2000). Although the spatial resolutions provided by the macro indentation and micro indentation is lower when compared to a nanoindentation.

$$H = \frac{P_{max}}{A_r} \tag{7.1}$$

where $Pmax$ corresponds to the peak indentation load, Ar is the area of the indent and H is the hardness.

Furthermore, during the initial developments of the nanoindentation technique, due to the small scales of indent, measurements pertaining to the area of indent were inaccurate. In order to address these issues, atomic force microscopy and scanning electron microscopy were used as well. However, the method became unwieldly. This led to the improvements in the technique of nanoindentation.

In the early 1990s, an improved technique for determining hardness and elastic modulus using load and displacement sensing indentation method was introduced into the research community (Oliver and Pharr, 1992; Lucas et al., 1998; Page et al., 1998; Gao and Wu, 1993). This technique is highly scalable and thus enables the determination of the mechanical properties of materials even at very small scales. The load displacement data corresponding to the indents, even though at a very small length scale, made way for such a break through (Oliver and Pharr, 2003).

The load displacement sensing technique helps in the measurement of two mechanical properties such as elastic modulus E and hardness H. The material is subjected to a cycle of loading and unloading and the curve corresponding to the unloading is analyzed. The unloading cycle corresponds to the deformation of the elastic half space. It also establishes the relation between the contact area at peak load and the elastic modulus. Furthermore, the technique incorporates plasticity, making the constitute relations nonlinear and thus demanding extensive experimentation

and simulations to understand it. The load displacement technique address the effects of non-rigid indenters on the load displacement behavior by formulating the reduced modulus, E_r (Tabor, 1948; Stillwell and Tabor, 1961).

$$\frac{1}{E_r} = \frac{1-\upsilon^2}{E} + \frac{1-\nu_i^2}{E_i} \tag{7.2}$$

where E is the Young's modulus and ν is the Poisson's ratio of the specimen or the material and E_i and ν_i are the corresponding parameters for the indenter.

The microhardness techniques later developed used the reduced modulus in the equations that were used to analyse the indentation data. The equation is given as follows

$$S = \frac{dP}{dh} = \frac{2}{\sqrt{\pi}} E_r \sqrt{A} \tag{7.3}$$

where, S is the experimentally measured stiffness of the upper portion of the unloading data, E_r is the reduced modulus and A is the projected area of elastic contact (Ternovskii et al., 1973; Bulychev et al., 1975; Bulychev et al., 1976; Shorshorov et al., 1982). This function though initially was developed for conical indenters, is useful for other indenter shapes as well (Bulychev et al., 1975). Besides, Figure 7.1 represents a typical schematic of the load displacement curve for which the above equation holds valid.

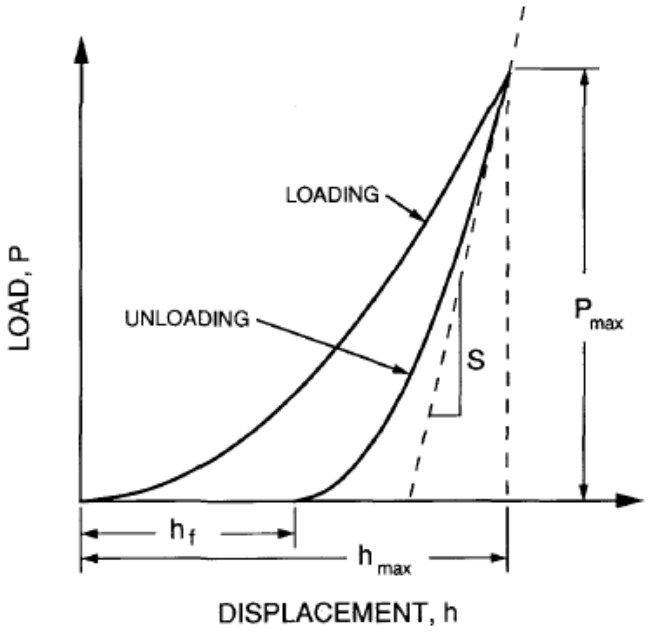

Figure 7.1 Load versus Displacement curve. Pmax corresponds to the peak indentation load, hmax corresponds to indenter displacement at the peak load, hf is the final depth of contact impression after the cycle of loading and unloading. S corresponds to the initial unloading stiffness (adopted from Oliver and Pharr, 1992).

The load displacement sensing technique thus developed used the principle that the material conforms to the indenter shape up to a certain depth on the application of peak load. This led to the importance of obtaining the depth at the peak load. Besides, the indenter shape function helps in obtaining the area of the indent by knowing the corresponding depth. As shown in figure 7.1, the indenter displacement at peak load and final depth of contact impression can be obtained from the load displacement curves. Further, hardness is obtained as the ratio of the peak load to the area of the indent thus obtained.

The load displacement nanoindentation technique which was developed used the Berkovich indenter tip (Oliver and Pharr, 2003). The Berkovich tip is a three-sided pyramid with the same area to depth relation as that of the Vickers indenter. The system used for the testing was a Nanoindenter (Nano instruments, Inc., Knoxville, TN) at the Oak Ridge National Laboratory with a load resolution of 0.3μN and displacement resolution of 0.16nm. In order to ensure reversibility of the deformations and for the unloading data to lie within the elastic regime, a series of loading and unloading cycles were performed and later the study had a loading kept constant for a duration of 100 s at 10% peak load. This data can be used to analyze the thermal fluctuations and creep characteristics of the material. All these experiments were thermally controlled. The experiments used peak loads over a range of 120 mN to 0.5 mN using a geometric progression ratio of 0.33. A similar ratio was used to determine the loading or unloading rates as well. A 5000μN/ s rate was used for the indentations which correspond to the peak load of 120 mN.

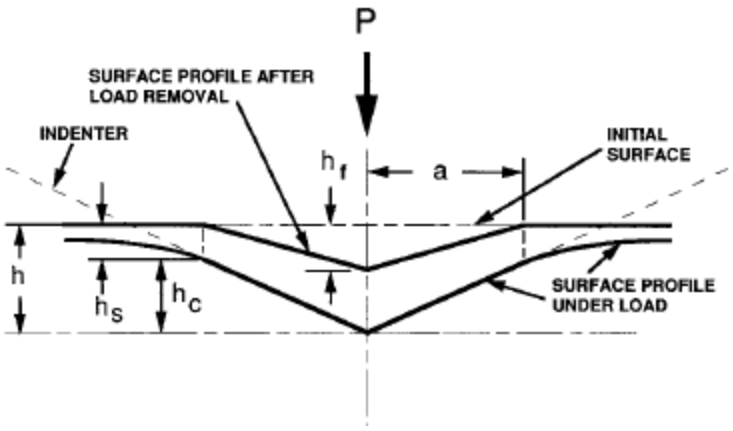

Figure 7.2 Schematic of the cross section of the indentation (adopted from Oliver and Pharr, 1992).

At any given instant of loading, the total displacement h, as shown in Figure 7.2, is the summation of h_c and h_s, the vertical distance along which contact is made and displacement of the surface at the perimeter of contact. P is the load applied on to the indenter which reaches a maximum of P_{max}. The displacement corresponding to this peak load is given by h_{max}. The radius of contact circle is given by a. h_f corresponds to final depth of residual hardness impression after the indenter is entirely recovered. The elastic displacements at the contact are recovered post the unloading part of the cycle. Initial unloading stiffness is determined at the peak load and is denoted by S_{max}. Thus, knowing the contact area, A, measured stiffness, S, reduced modulus Er can be computed using the relation given below.

$$E_r = \frac{\sqrt{\pi}}{2}\frac{S}{\sqrt{A}} \tag{7.4}$$

Area of contact at peak load is determined based on the depth of contact and indenter geometry. Area function is a functional of h, the distance from the bottom of the tip (Oliver and Pharr, 2003). These relations are represented using the following equations.

$$A = F(h_c) \tag{7.5}$$

where A is the area function and h_c is contact depth as shown in Figures 7.2 and 7.3. h_c is determined using the following relation.

$$h_c = h_{max} - h_s \tag{7.6}$$

where h_{max} is experimentally measured from the load displacement curve as shown in Figure 7.3 and h_s, the displacement of the surface at contact perimeter is determined using the following relation.

$$h_s = \frac{(\pi-2)}{\pi}(h - h_f) \tag{7.7}$$

where $(h\text{-}h_f)$ is the elastic component of the displacement. Sneddon's force displacement relation for conical indenter, whose analytical solution paves way for Berkovich tip indenter, is as follows,

$$\left(h - h_f\right) = 2\frac{P}{S} \tag{7.8}$$

where S is the stiffness. Plugging in the expression for $(h\text{-}h_f)$ in the equation for h_s gives the following relation,

$$h_s = \epsilon \frac{P_{max}}{S} \tag{7.9}$$

where ϵ is the geometric constant and is dependent on the type of indenter chosen for the study. For the paraboloid indenters ϵ is 0.75.

The unloading curves can be accurately described using the power law relation shown below, when using the Berkovich indenter tip.

$$P = A\left(h - h_f\right)^m \tag{7.10}$$

where P is load applied on the indenter, $(h\text{-}h_f)$ is elastic displacement and A and m are material constants. m varies in the range of 1.25 to 1.51 depending on the material. The area of contact changes continuously during unloading, this shows the importance of continuous dynamic stiffness measurements for the nanoindentation experiments. The continuous measurement is attained by applying a small oscillation on the force signal at a high frequency of 69.3 kHz. The amplitude is regulated to maintain a small value The equations pertaining to the load frame compliance and

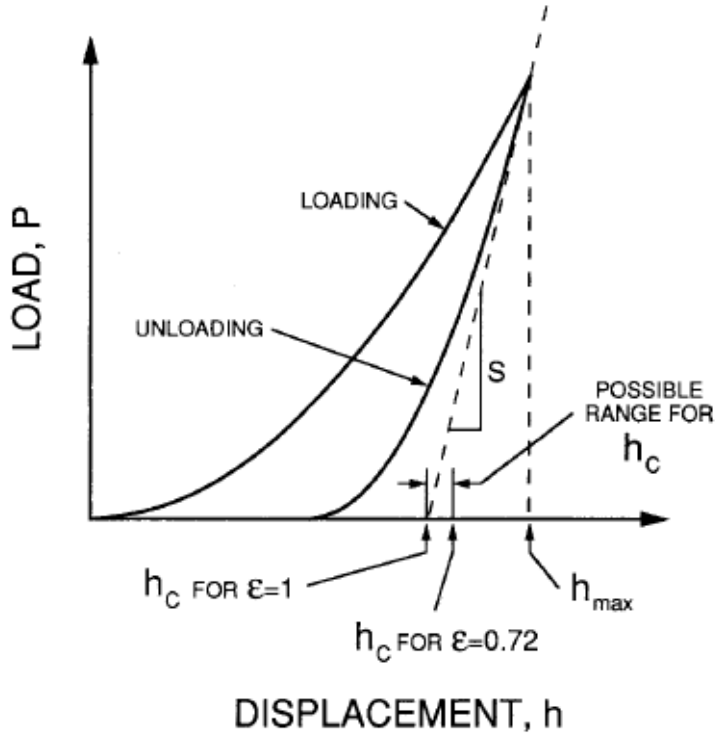

Figure 7.3 Schematic of the load displacement curve used to determine the contact depth (adopted from Oliver and Pharr, 1992).

diamond indenter area function are given below.

The load frame with a compliance C_f and specimen with a compliance C_s are in series as shown in the following equation.

$$C = C_s + C_f \tag{7.11}$$

C, the total compliance is now obtained as follows, by substituting the expression for specimen compliance.

$$C = C_f + \frac{\sqrt{\pi}}{2E_r}\frac{1}{\sqrt{A}} \tag{7.12}$$

Initial value of area function for a perfect Berkovich indenter is obtained using the following expression.

$$A(h_c) = 24.5h_c^2 \tag{7.13}$$

This is obtained from the expression

$$A(h_c) = 24.5h_c^2 + C_1h_c^1 + C_2h_c^{1/2} + C_3h_c^{1/4} + \ldots + C_8h_c^{1/128} \tag{7.14}$$

where C_1 to C_8 represent constants. The first term corresponds to a perfect Berkovich indenter and the higher order terms correspond to the deviations such as blunting of the tip. The value thus obtained can be used for the initial computation of C_f and E_r. These initial computations can now be used for the computations of area functions and the iterations can thus be performed until a convergence is attained.

7.2 Nanoindentation Test – Equipment

Continuous stiffness measurement (CSM) nanoindentation testers (NHT^2) are widely used in the research community. They provide high resolution data acquisition. They are designed for low

loads and thus depth measurements which are at the nanometer level on the length scale. Nanoindentation tester constitutes the top surface referencing technique. This is based on the fact that indenter tip is retracted inside a reference ring. This arrangement enables a quick approach towards the specimen surface, thus reducing the time consumed for each indentation. In addition, the reference protects the indenter tip from any sudden contact with the specimen surface.

Figure 7.4 Nanoindentation tester head (adopted from CSM NHT2 documentation).

The Nanoindentation tester comprises of a high frame with stiffness (~10^7 N/m) which provides a high stability to the instrument. Furthermore, the Nanoindentation tester supports a wide range of loads for the testing purposes (0.1 mN to 500 mN). The loads below 1 mN can be

considered to be in the nanoindentation range and the loads from 10 mN to 500 mN can be considered to be in the micro indentation range.

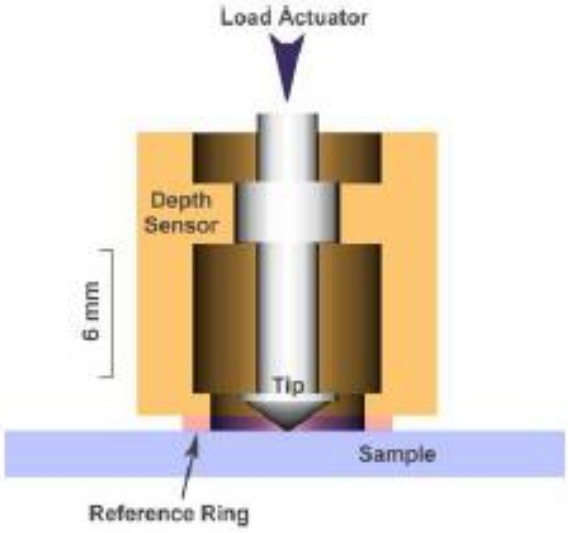

Figure 7.5 Cross section of the Nanoindentation head showcasing the depth sensor (adopted from Anton Paar, CSM, NHT^2 documentation).

The NHT^2 enables accurate depth measurements with an accuracy of less than a nanometer. This is achieved due to the depth sensor which is closely placed to the specimen. This provides a very low frame compliance and thus very high thermal stability. Similar to the discussion in section 5.2.2, the nanoindentation module as well is integrated with the optical microscope. The optical microscope is the same as that used for the micro scratch tester. This integration between the nanoindentation module and the optical microscope enables a position synchronization of up to 0.5 µm. The test location can thus be precisely measured. In addition, the Anton Paar

nanoindentation platform lies on an anti-vibration table which comprises of the air compressor. Thus the instrumental setup minimizes the external factors which might cause variations which might affect the nanoindentation data acquisition.

Figure 7.6 Anton Paar Nanoindentation Tester head and the integrated Optical microscope (Credits: Kavya Mendu, UIUC, 2017).

CSM Instruments Indentation software enables Adjust Depth offset measurement before conducting the series of indentation tests on the specimens. The tests can be performed in two modes, namely depth loop controlled mode or the force loop controlled mode at constant strain rates. All the parameters like loading or unloading rates, maximum load, pauses and modes can be

completely controlled by the user. Different load profiles such as user defined load pattern, single or multi cycle linear profile, square root loading ramps or unlimited hold time are available in the Anton Paar NHT2. A large area mapping is possible with the Anton Paar NHT2. Multi focus image of the indentation is available. This feature captures perfect depth of field. Figure 7.7, adopted from the Anton Paar, CSM documentation shows a series of images obtained using the Multi Focus feature.

In addition, CSM NHT2 offers a wide range of analysis methods namely Martens hardness, Tangent, Oliver & Pharr, Creep Analysis and Adhesion Analysis. Oliver & Pharr analysis method is the one explained in section 8.1. As discussed earlier, the Oliver & Pharr method is widely used for load displacement Nano indentation technique. Another popular method is the Martens hardness method. This corresponds to the indentation which uses the quadratic loading profile.

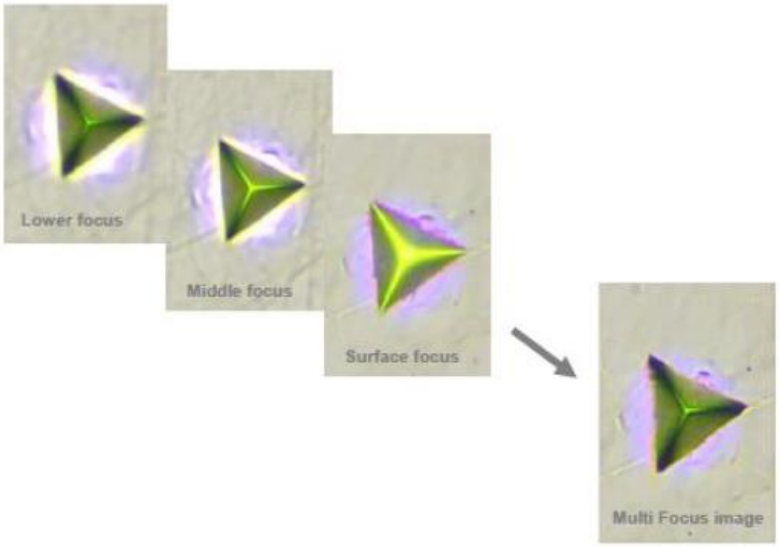

Figure 7.7 Multi Focus Image of the Indentation (adopted from CSM Instruments NHT2 Documentation).

The CSM NHT^2 tester computes the elastic modulus and hardness of the material based on the analysis method that is chosen for the analysis. In addition to the elastic modulus and hardness, the software also computes the work of the elastic and plastic deformations.

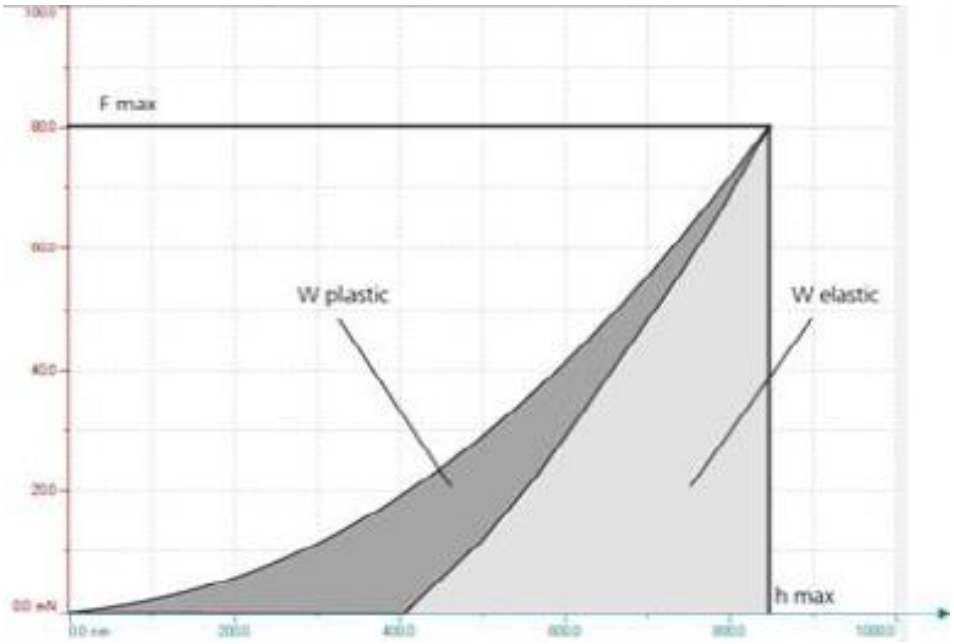

Figure 7.8 Schematic of the nanoindentation test which shows the elastic and plastic deformation works.

7.3 Technical Specifications

The CSM Nanoindentation tester offers fine resolutions of all the parameters discussed in section 7.2. Table 7.1 shows the indentation parameters and their ranges and resolutions. Sustainability under the Nano scope laboratory at the University of Illinois at Urbana Champaign uses the Nanoindentation tester with the parameters which are in accordance with the Table 7.1.

Table 7.1 Parameters of the nanoindentation tester formulated in the tabular form. Data as obtained from the manufacturer of the ANTON PAAR NHT, CSM Instruments Inc.

Penetration Depth		
	Fine Range	Large Range
Maximum Depth (um)	40	200
Depth Resolution (nm)	0.01	0.06
Noise Floor RMS value (nm)	0.3	
Maximum indenter travel range (µm)	200	
Normal Load		
	Fine Range	Large Range
Maximum Load (mN)	1	500
Minimum usable load Fmax (mN)	0.1	
Minimum contact force (µN)	Less than 1	
Loading rate (mN/min)	Up to 5000	
Contact Force Hold time	Unlimited	
Repositioning accuracy (µm)	±0.5	
Acquisition Rate (Hz)	60.0	
Stiffness threshold (µN/ µm)	500	

Table 7.1 (cont.)

Spring Compliance (mm/N)	0.95
Maximum Sample Size	
Compact platform (mm)	200 x 200 x 100
Open Platform (mm)	295 x 300 x 100

7.4 Chapter Summary

This chapter describes the indentation technique in general and provides a summary of the available indentation techniques. A detailed description of the Nanoindentation technique which is of specific interest for this study is provided in this chapter. A specific focus was laid on the most widely used analysis method, formulated by Oliver and Pharr (1992). This method is used for the computation of elastic modulus and hardness for this study. The equipment used for the study, CSM Nanoindentation tester, is described in detail and the very fine resolutions and ranges provided by the instrument are explained as well.

CHAPTER 8

APPLICATION OF NANOINDENTATION TO CORTICAL BONE

The principle and applications of nanoindentation were discussed earlier in section 8.1. Nanoindentation tests have been extensively used in the research community to understand the elastic properties of materials. Biomedical applications of the nanoindentations have been studied over the past years. Most of the biological samples have complex hierarchical structure. Thus, there arises the need to study the mechanical properties of each level of the hierarchy.

Cortical bone, as explained earlier in section 2.1 is a complex hierarchical biological specimen. As discussed in sections 2.2 and 6.2, indentation tests have been used to study the fracture toughness of the specimens (Mullins et al., 2007; Kruzic and Ritchie, 2003; Quinn and Bradt, 2007). There were limitations of using these tests for fracture toughness measurements as discussed earlier. However, nanoindentation have also been applied to study the mechanical properties of cortical bone (Rho and Pharr, 1999; Hengsberger et al., 2002; Furin et al., 2016). The mechanical properties such as elastic modulus and hardness are computed from the data acquainted from the nanoindentation tests using the Oliver and Pharr method, one of the most widely accepted methods for analysis.

8.1 Specimen Preparation

As discoursed earlier, this chapter presents an overview of the mechanical properties of cortical bone specimens. Swine cortical bone specimens were tested for this study. Section 2.1 presents the analogy between the hierarchical structures of swine and human cortical bones especially the femurs. Further, section 6.1 presents the reasons to test the swine cortical bone specimens instead of the human cortical bone specimens. For the conduction of nanoindentation tests at such small length scales, the specimens to be tested need to be very flat. Thus, the specimen preparation protocol is a very important step of the experimental procedure.

8.1.1 Specimen Procurement

Similar to the specimens obtained for micro scratch testing, porcine or swine femurs were obtained from the Meat Science Laboratory of University of Illinois at Urbana Champaign as well. The swine from which the femurs were obtained were 22-26 weeks old. The swine were harvested for a duration of 24 hours after slaughter. The animals were corn fed and weighed about 275 pounds.

As per the animal facts mentioned by the British Columbia Society for the prevention of cruelty to animals, it takes up to 5-6 months to rise a swine from birth to that of the market weight. This is approximately 22-26 weeks old. The market weight of the pigs or swine is given as 255-275 lb. Thus, the femurs are obtained from fully grown swine.

The femurs were transported from the Meat Science Laboratory in plastic air tight bags. The femurs thus obtained were kept frozen at -20^{o}C temperature to keep them fresh until the specimen preparation procedure begun. As discussed earlier in section 6.1.1, storing the specimens at a temperature of -20^{o}C keeps the specimens relatively fresh compared to other storage techniques (Linde and Christian, 1993).

8.1.2 Cutting and Cleaning

Swine Femurs which were stored at -20^{o}C were thawed and 80 mm long sections were cut from the mid-diaphysis region using a Table Top Diamond Band Saw (Gryphon Corporation, Sylmar, CA). The specimens were then stored in physiological conditions in the Hanks Balanced Saline Solution for a duration of 48 hours on an average. The trabecular or cancellous bone region containing the tissue was then removed using a dissection kit.

As discussed earlier in chapter 3 and 6, due to the anisotropy in the bone specimens, the exists two distinct orientations of the cortical bone. Longitudinal transverse and short longitudinal are the two directions. Longitudinal – Transverse (LT) specimens correspond to the mechanical properties in the direction perpendicular to the longitudinal axis of the cortical bone specimens. Whereas, Short – Longitudinal (SL) specimens correspond to the mechanical properties in a direction along the longitudinal axis of the specimens.

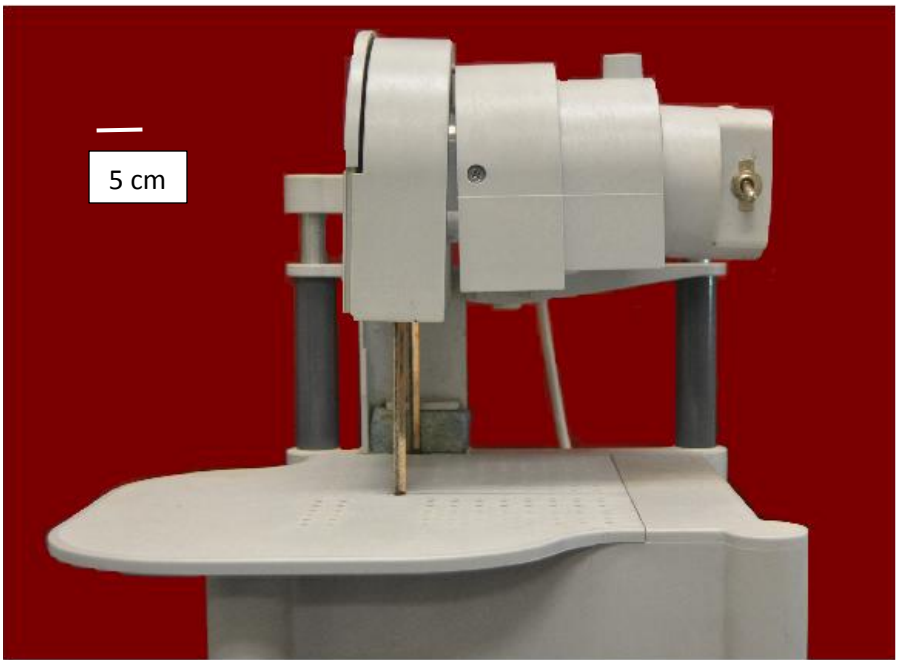

Figure 8.1 Table top diamond band saw (Credits: Kavya Mendu, UIUC, 2017).

The 80 mm long mid diaphysis region of the femurs were further cut using a diamond-wafering blade on the Buehler Isomet 5000 precision cutter to obtain smaller sizes. A blade speed of 1500rpm, with a feed rate of 2.5-3mm/min. The cutting procedure is a wet process where in the coolant used is a solution of Isocut Cool 3 with Distilled Water in a ratio of 1:25. After this procedure, the dissection kit is again employed to remove any unwanted flesh or tissue material on the bone specimens. A deeper cleaning of the specimens is done in a solution prepared using 1.5% Alconox and 5% Bleach and ultra-sonically cleaned for a duration of 20 minutes. The

specimens were then dried at 50ºC for a duration of 24 hours (Yeni et al 2000; McAlden 1993). This step was to remove the effects of hydration on the organic content of the specimens. The specimens thus obtained were placed in the Hanks Balanced Saline Solution until further process.

8.1.3 Embedding, Grinding and Polishing

The porcine cortical bone specimens are now embedded in a casting resin to facilitate easy handling and enhance stability of the specimens during grinding, polishing and testing. Like the micro scratch testing specimen preparation, several protocols for embedding, grinding and polishing were tried and tested in the due course of obtaining a standard procedure for porcine cortical bone specimens. A complete account of the several protocols tested, the limitations and shortcomings faced in each of them, which led to the final preparation is described as follows.

As an initial procedure, the porcine cortical bone specimens which were oven dried were embedded in epoxy resin (Epothin, Buehler, Lakebuff, IL) at room temperature. The curing time was around 9 hours. Hardening of the resin was an exothermic reaction, thus leading to a rise in the temperature by about 3-4ºC. Thus to reduce the effects of heat released due to the resin hardening at a later stage Polymethyl Methacrylate (PMMA) resin replaced epoxy resin.

Embedded specimens were then cut into 5-mm thick discs using the Buehler Isomet 5000 Precision Cutter (Buehler, Lakebuff, IL) . The specimens are then mounted on to metal (aluminum)

discs using cyanoacrylate adhesive. Thus, the longitudinal specimens, longitudinal-transverse (LT) the femurs were made into semicircular sections. Whereas for the transverse specimens, short-longitudinal (SL) they were made into approximately 2cm X 1.5cm X 5mm cuboidal shapes. This study consists of the nanoindentations performed on the short-longitudinal specimens. The specimens similar to that mentioned in section 6.1.3. In order to obtain smooth flat surfaces, the specimens were ground and polished. The epoxy embedded porcine cortical bone specimens were ground and polished using Buehler Ecomet 250 Grinder-Polisher (Buehler, Lakebuff, IL) as shown in Figure 8.2.

Figure 8.2 Buehler Ecomet 250 Grinder and Polisher, Buehler, Lakebuff, IL. (Credits: Kavya Mendu, UIUC, 2017).

Protocol I

The swine or porcine cortical bone specimens were ground using 400, 600, 800 and 1200 grit silicon carbide abrasive pads for a duration of 2 minutes under a load of 2 lbs. Followed by this, the specimens were polished using 9 µm, 3µm, 1µm and 0.25µm diamond suspensions on Texmet P (Buehler, Illinois). Each of the polishing step lasted for 15 minutes under a load of 3 lbs. The base and head speeds of the Ecomet 250 (Buehler, Illinois) were maintained at 300rpm and 60 rpm respectively. A Branson 5800 Ultrasonic Cleaner was used to ultrasonically clean the specimens after every intermediate step to avoid cross contamination. The ultrasonic cleaning lasted for a duration of 2 minutes.

Under the optical microscopy, we observe the osteons, haversian canals and interstitial regions of the cortical bone specimens. In addition, if the procedure is yielding good results then we do not observe a surface which is having several scratches due to the grinding and polishing on the bone specimens. As we can see from Figure 8.3, the bone features such as osteons, lamellae were clearly visible. However, several scratches were evident on the surface as well.

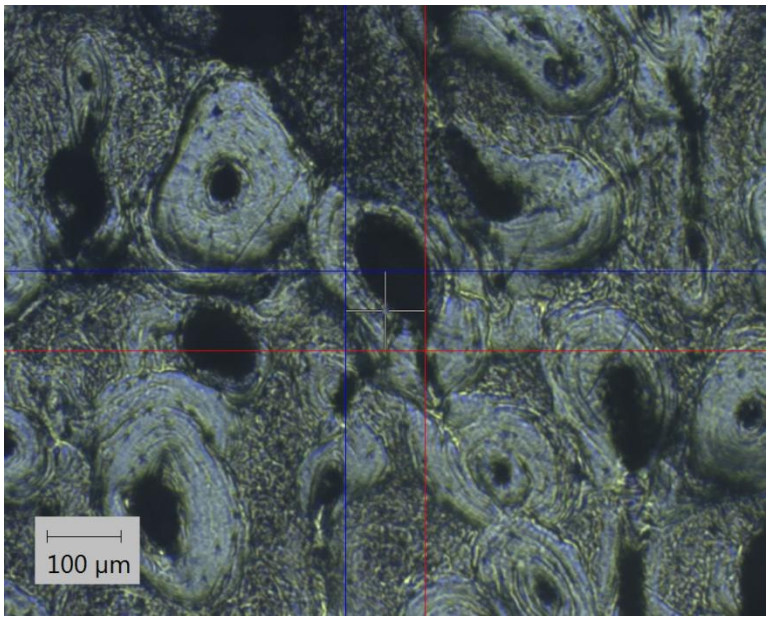

Figure 8.3 Image of the polished porcine specimen using protocol 1.

Table 8.1 Summary of the Steps involved in grinding and polishing the porcine cortical bone specimens using Protocol I.

Grinding						
Step	Grit Size	Pad	Base Speed	Head Speed	Duration	Force
1	400 grit	Silicon Carbide	150 rpm	60 rpm	2 minutes	2 lbs
2	600 grit	Silicon Carbide	150 rpm	60 rpm	2 minutes	2 lbs
3	800 grit	Silicon Carbide	150 rpm	60 rpm	2 minutes	2 lbs
4	1200 grit	Silicon Carbide	150 rpm	60 rpm	2 minutes	2 lbs

Table 8.1 (cont.)

Polishing						
1	9 microns	TexMet P	300 rpm	60 rpm	15 minutes	3 lbs
2	3 microns	TexMet P	300 rpm	60 rpm	15 minutes	3 lbs
3	1 microns	TexMet P	300 rpm	60 rpm	15 minutes	3 lbs
4	0.25 microns	Texmet P	300 rpm	60 rpm	15 minutes	3 lbs

Protocol II

This protocol consists of wrapping the embedded specimens in the gauge soaked with phosphate buffer solution. The specimens were then ground using 400, 600, 800 and 1200 grit silicon carbide abrasive pads with the parameters similar to that of the protocol 1. An additional polishing step corresponding to 0.05µm alumina solution on the Pressure Sensitive Backed (PSA) backed 8 inch diameter Micro Cloth (Buehler, Illinois) (Xu et al 2003) was incorporated. The duration of this step was 4 minutes under a load of 3lbs. The table given below summarizes the protocol.

Table 8.2 Summary of the Steps involved in grinding and polishing the porcine cortical bone specimens using Protocol II

Grinding						
Step	Grit Size	Pad	Base Speed	Head Speed	Duration	Force

Table 8.2 (cont.)

1	400 grit	Silicon Carbide	150 rpm	60 rpm	2 minutes	2 lbs
2	600 grit	Silicon Carbide	150 rpm	60 rpm	2 minutes	2 lbs
3	800 grit	Silicon Carbide	150 rpm	60 rpm	2 minutes	2 lbs
4	1200 grit	Silicon Carbide	150 rpm	60 rpm	2 minutes	2 lbs
Polishing						
1	9 microns	TexMet P	300 rpm	60 rpm	15 minutes	3 lbs
2	3 microns	TexMet P	300 rpm	60 rpm	15 minutes	3 lbs
3	1 microns	TexMet P	300 rpm	60 rpm	15 minutes	3 lbs
4	0.25 microns	Texmet P	300 rpm	60 rpm	15 minutes	3 lbs
5	0.05 microns	Micro cloth	300 rpm	60 rpm	4 minutes	3 lbs

Protocol III

The cortical bone specimens were ground using 400, 600, 800 and 1200 grit silicon carbide abrasive pads with a duration of 2 minutes under a load of 2 lbs. Followed by a polishing procedure which passes other intermediate steps and uses 0.05μm alumina solution on a micro cloth for a duration of 4 minutes and 3 lbs. (Zioupus; 2007). This procedure even though is quick, resulted in optical microscopy images with scratches on the surface.

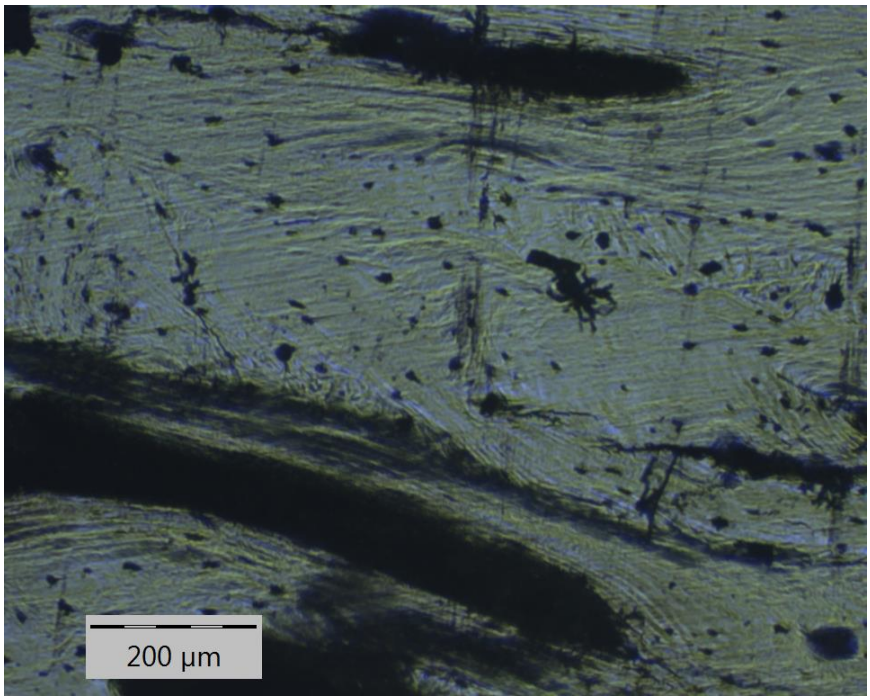

Figure 8.4 Image of the polished specimen using the protocol III.

Table 8.3 Summary of the Steps involved in polishing the porcine cortical bone specimens using Protocol III.

Grinding						
Step	Grit Size	Pad	Base Speed	Head Speed	Duration	Force
1	400 grit	Silicon Carbide	150 rpm	60 rpm	2 minutes	2 lbs
2	600 grit	Silicon Carbide	150 rpm	60 rpm	2 minutes	2 lbs
3	800 grit	Silicon Carbide	150 rpm	60 rpm	2 minutes	2 lbs

Table 8.3 (cont.)

4	1200 grit	Silicon Carbide	150 rpm	60 rpm	2 minutes	2 lbs
Polishing						
1	0.05 microns	Micro cloth	300 rpm	60 rpm	4 minutes	3 lbs

Protocol IV

To have more control on the steps 400 and 600 grit grinding, hand grinding was adopted. Further the 9 µm diamond suspension polishing step was avoided as it was causing a redundance of the grinding or polishing steps. 1200 grit grinding step corresponds to a roughness of 8 µm. Hence, performing the 9µm polishing post 1200 grit grinding induces more roughness rather than flattening and polishing the specimens. In addition, the durations for each of the steps are increased and the summary is tabulated below. Figure 8.5 shows the image of the final polished swine cortical bone specimen.

Table 8.4 Summary of the Steps involved in polishing the porcine cortical bone specimens using Protocol IV.

Grinding						
Step	Grit Size	Pad	Base Speed	Head Speed	Duration	Force
1	400 grit	Silicon Carbide	100 rpm	N/A	1 minutes	Hand Grinding

Table 8.4 (cont.)

2	600 grit	Silicon Carbide	150 rpm	N/A	5 minutes	Hand Grinding
3	800 grit	Silicon Carbide	150 rpm	60 rpm	15 minutes	1 lb
4	1200 grit	Silicon Carbide	150 rpm	60 rpm	15 minutes	1 lb
Polishing						
1	3 microns	TexMet P	300 rpm	60 rpm	20 minutes	2 lbs
2	1 microns	TexMet P	300 rpm	60 rpm	20 minutes	2 lbs
3	0.25 microns	TexMet P	300 rpm	60 rpm	20 minutes	2 lbs
4	0.05 microns	Texmet P	300 rpm	60 rpm	20 minutes	2 lbs

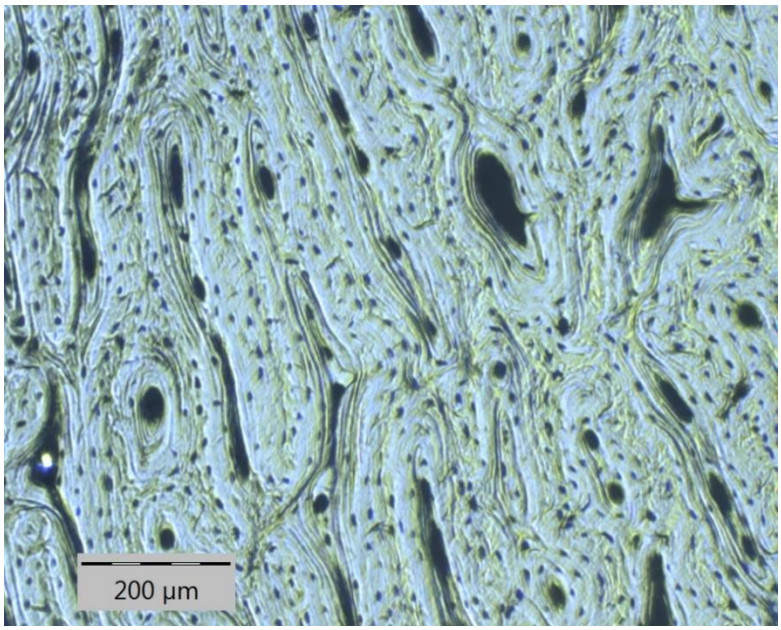

Figure 8.5 Image of the polished specimen using the protocol IV.

8.2 Instrumented Indentation Techniques

Nanoindentation technique, described in chapter 7, using the Anton Paar Nanoindentation tester, CSM Instruments Inc., was now adopted on the polished cortical bone specimens. A diamond Berkovich indenter tip, three-sided pyramid with a half angle of 65.27^{o} was used to perform the nanoindentation tests. A description of the area function of the Berkovich indenter tip was discussed earlier in section 7.1. The instrument is calibrated to have a spring compliance of 0.95 mm/N and stiffness threshold of 500 µN/ µm. The other technical specifications and resolutions of the instrument were described in the table 7.1.

8.2.1 Statistical Nanoindentation

Statistical nanoindentation, also known as the grid indentation technique is well suited for heterogeneous materials like cortical bone (Ulm et al., 2007; Sorelli et al., 2008; Ulm et al., 2010; Vandamme et al.,2010). This technique accounts for the variability of the material properties over the microscopic and nanoscopic length scales. The statistical nanoindentation technique is performed over a large area which is a statistical representation of the distinctive phases existing in the material. Based on the length scale of interest, the indentation depth is to be chosen. Each indent in the grid of indents represent a statistical event. All the indentations are now analyzed using statistical deconvolution methods to determine the material properties of the individual phases. The statistical deconvolution technique developed by Ulm et al., (2007) considers the existence of two distinct phases in the material.

The deconvolution is applied for the corresponding material property which is to be analyzed. Thus, for the material property x, the experimentally obtained values $P(x)$ corresponding to the grid of n indents is given by the following equation,

$$\min P(x) = \sum_{i=1}^{m} \sum_{x} \left(\sum_{j=1}^{n} f_j p_j(x_i, \mu_j, s_j) - P(x_i) \right)^2 \qquad (8.1)$$

Where μ_j, is the mean of x, s_j is the standard deviation of x, f_j is the volume fraction of each phase. m corresponds to the discretization interval and p_j corresponds to the probability density function of each phase, a normal distribution (Sorelli et al., 2008).

$$p_j = \frac{2}{\sqrt{2\pi s_j^2}} \exp\left(\frac{-(x-\mu_j)^2}{2s_j^2}\right) \tag{8.2}$$

Thus, for the tests conducted on bone a series of grid indents were performed to determine the properties. On the polished swine cortical bone specimens, linear loading with a maximum indentation load of 0.5 mN and 2mN were used. The indents were performed as square grids of 3x3, 5x5, 10x10 and 20x20 thus giving rise to 9, 25, 100 and 400 indents respectively. The spacing was maintained at 10µm. The test locations were chosen such that there occurs no large features like the haversian canals in the matrix that was tested.

The loading rate is chosen such that it is six times the maximum indentation load numerically. The approach distance was 2500 nm and the indenter approach speed was 1500 nm/min. The holding time between the loading and unloading cycles was prescribed at 5 seconds. The indenter retract speed was 2500 nm/min and the retract time was 3 seconds. Figure 8.7 shows the optical microscopy image of the portion of the 20x20 grid indentations that were performed on the swine cortical bone specimen – short longitudinal specimen.

8.3 Nanoindentation Test Analysis

As discussed in chapter 8, the Anton Paar NHT^2 generates a load displacement curve for every indentation test. An example of the load displacement curve as generated by the software when a nanoindentation test was conducted on the porcine cortical bone specimens is shown in Figure 8.6.

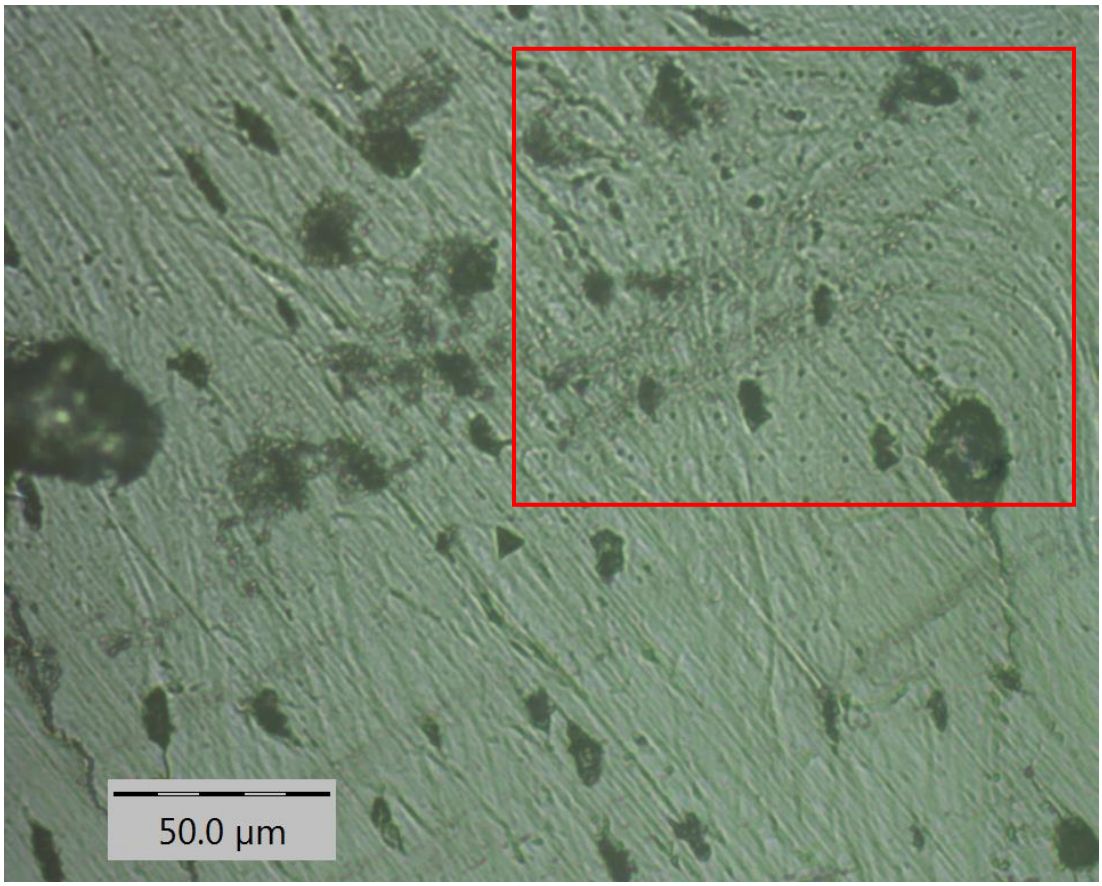

Figure 8.6 Image showing a portion of the 400 indentations performed on the swine cortical bone specimen – short longitudinal.

A typical indentation resulted in a penetration depth in the ranges of 70 nm to 180 nm for a maximum load of 0.5 mN and 200 nm to 400 nm for a maximum load of 2mN. As mentioned earlier, Oliver and Pharr method was used as the analysis method for this study. Based on this method, the indentation software computes the elastic modulus and hardness.

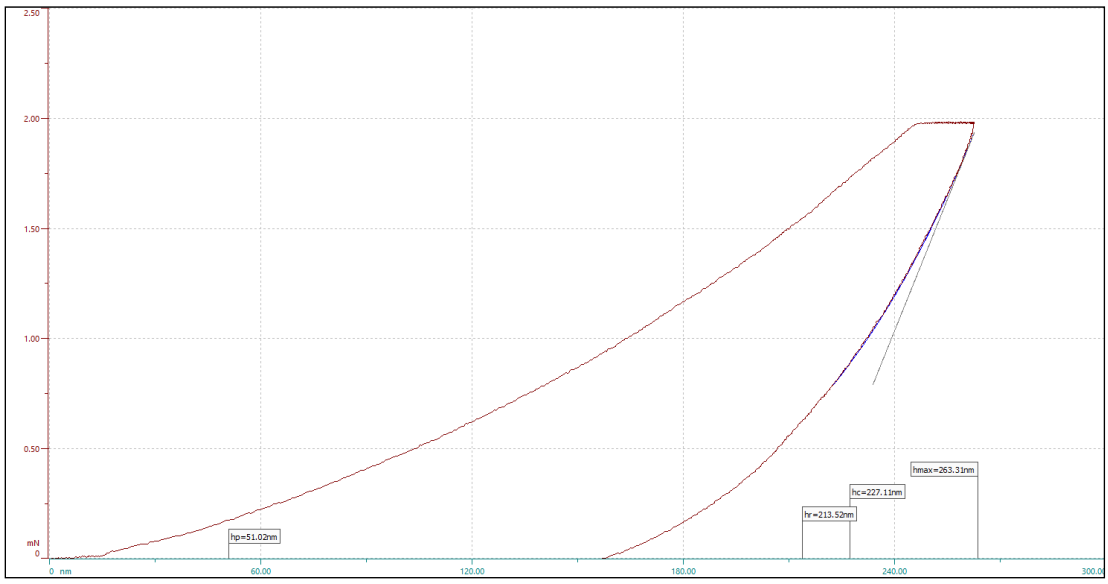

Figure 8.7 Load displacement generated by the nanoindentation software; the software computes the contacts depths and denote it on the graph corresponding to each indent.

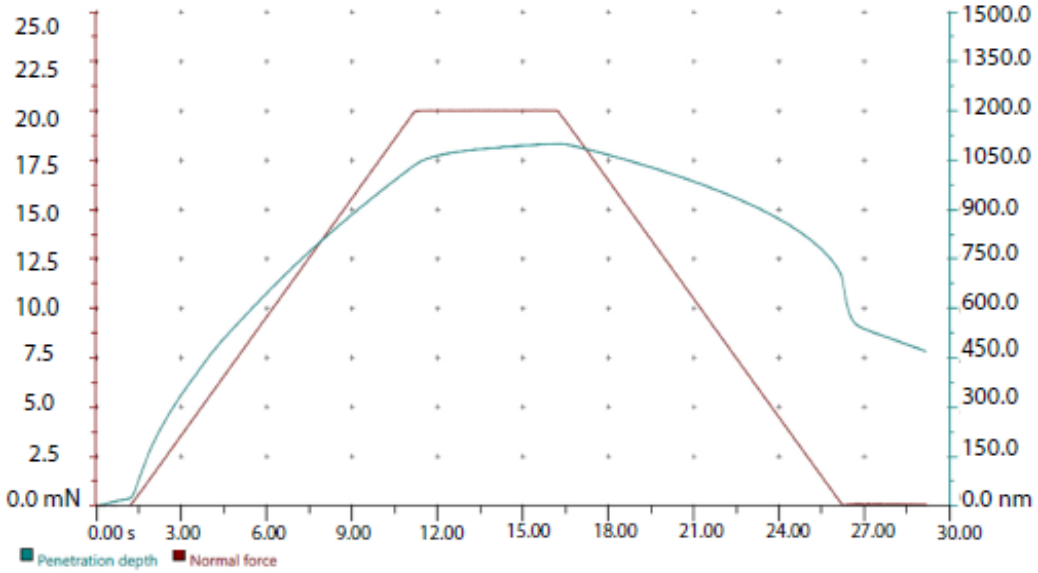

Figure 8.8 Plot showing the penetration depth and normal force.

Table 8.5 Average of the Elastic Modulus and Hardness of the short longitudinal porcine cortical bone specimens.

Grid size	Maximum Load (mN)	Elastic Modulus (Gpa)	Hardness (GPa)
20 x 20	0.5	21.771	1.014
20 x 20	0.5	18.584	0.572
3 x 3	2	21.193	0.849
10 x 10	2	20.557	0.739
10 x 10	2	14.821	0.551
20 x 20	2	21.221	0.802
20 x 20	2	18.619	0.694
20 x 20	2	32.481	1.181

A series of different sized grids were chosen for the porcine specimens in order to perform a statistical analysis of the nanoindentations. Especially, the grid sizes of 10x10 and 20x20 which generate 100 and 400 indents respectively are suitable for the statistical nanoindentation analysis. Every indentation records its location and the computed indentation modulus and hardness. Each indentation corresponds to each data point. All the data points are considered for the statistical deconvolution and the phase map corresponding to average modulus and hardness are obtained. Figures 8.9 and 8.10 show the frequency plots of the elastic modulus and hardness of the porcine cortical bone specimens. Figure 8.11 depicts a scatter plot of E and H values for the cortical bone specimen corresponding to a grid of 20 x 20 indents operated at a maximum load of 0.5 mN. Further, Figures 8.12 and 8.13 show the phase map and elastic modulus map of the same test, 20 x 20 grid of indents carried out at a maximum load of 0.5 mN.

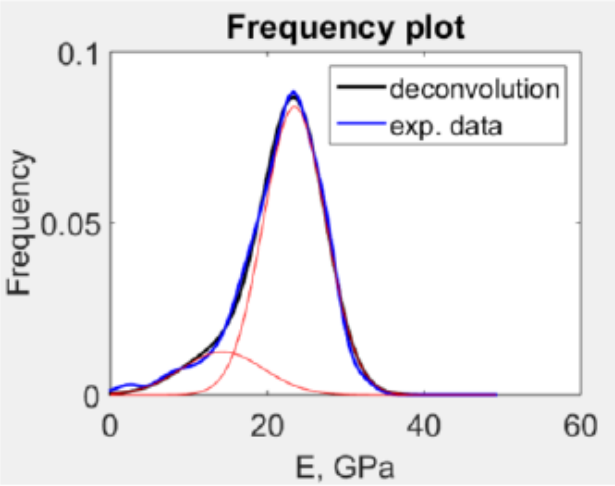

Figure 8.9 Frequency plot for Elastic modulus for a 20 x 20 grid corresponding to a peak load of 0.5 mN.

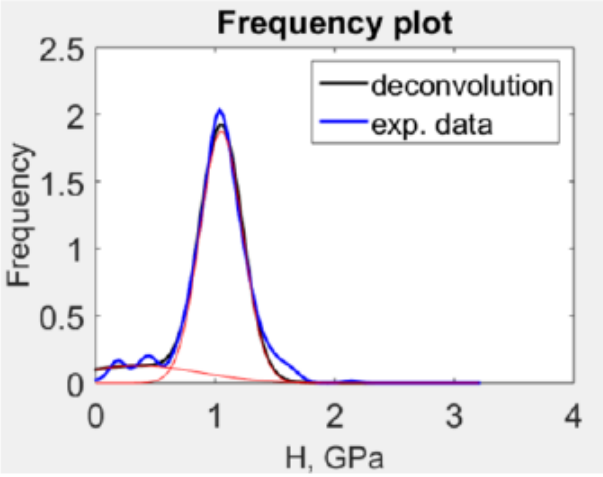

Figure 8.10 Frequency plot for Hardness for a 20 x 20 grid corresponding to a peak load of 0.5 mN.

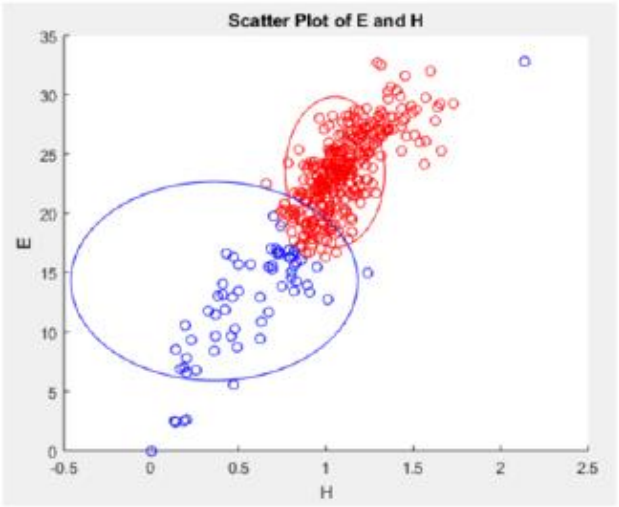

Figure 8.11 Scatter plot of the elastic modulus E (GPa) and H (GPa) of a 20 x 20 grid of indents corresponding to a peak load of 0.5 mN.

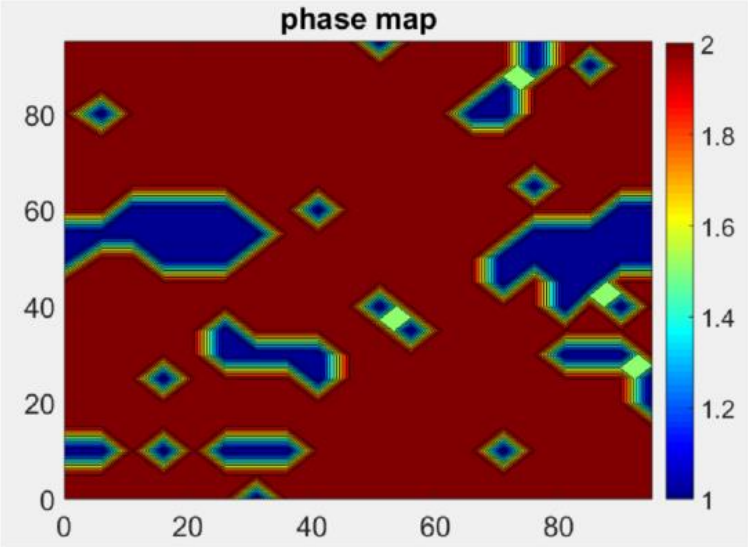

Figure 8.12 Phase map of a 20 x 20 indentation grid corresponding to a peak load of 0.5 mN on the porcine cortical bone specimen.

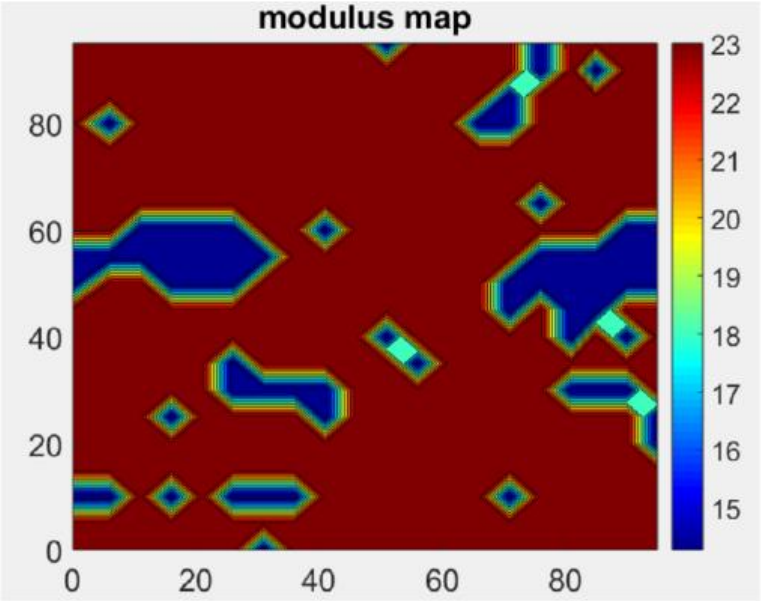

Figure 8.13 Modulus map of a 20 x 20 indentation grid corresponding to a peak load of 0.5 mN on the porcine cortical bone specimen.

Table 8.6 Average values from the statistical deconvolution of the nanoindentation tests performed at maximum load of 0.5 mN.

Phase	Elastic Modulus (Gpa)	Hardness (Gpa)	Volume Fraction
1	14.28	0.36	0.164
2	23.47	1.05	0.835

8.4 Chapter Summary

This chapter describes the application of nanoindentation technique for the mechanical characterization of porcine cortical bone specimens. Thus, the elastic modulus and hardness of the short longitudinal (transverse specimens) porcine cortical bone specimens were obtained based on the Oliver & Pharr method. Statistical deconvolution depicts the two phases observed in the porcine cortical bone specimens. The average values of the tests were reported and compared to the literature values mentioned in chapter 2.

CHAPTER 9

RATE EFFECT ANALYSIS

9.1 Introduction

Creep deformation occurs slowly upon the application of stress, unlike brittle fractures. Strain in the material is accumulated as a result of the long-term stress. Typically, creep is classified to three different stages on the time scale. Initial stage is the primary creep, with a high strain rate followed by the second stage which corresponds to secondary creep during which the strain rate is either linear or constant in general. The third stage corresponds to tertiary creep which corresponds to exponentially increasing strain rate.

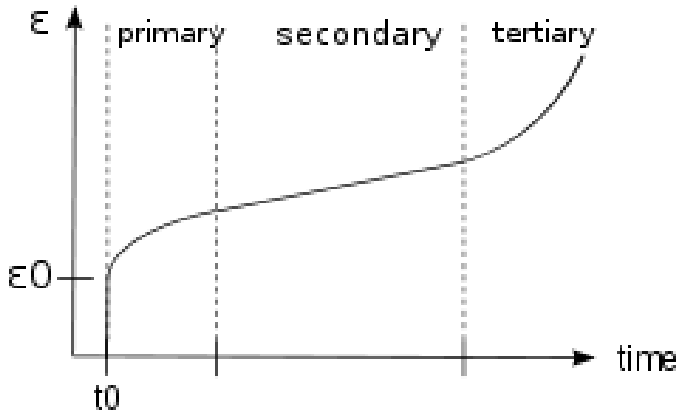

Figure 9.1 Typical strain rate curve showing different (three) stages of creep.

The first stage has a high strain rate which decreases with time due to the work hardening in the material. The second stage, a balance between the work hardening and annealing or thermal softening is called the steady state creep. The third state corresponds to the failure of the material where fracture occurs and the material permanently deforms (NADCA Design). Thus, creep is a time dependent deformation mechanism.

However, literature shows that the modeling of crack growth is essential to understand the effect of creep induced rate effects on the critical loads of the materials (Lee et al., 2002). Further, study shows that creep induced rate effect study is essential to understand the dynamic properties of material (Huang et al., 2007). This study uses different loading rates to study the creep properties of polycarbonate and epoxy.

9.2 Application to Cortical Bone Specimens

The literature review and the mechanical and fracture characterization tests performed so far shows the importance of study of cortical bone properties. Furthermore, studies showed the rate dependent nature of bone (Johnson et al., 2010; Adharapurapu et al., 2006; Lewis and Goldsmith, 1975; Tennyson et al., 1972; Roberts and Melvin, 1969; McElhaney et al., 1966). These studies focused on strain rates corresponding to those of physiologically relevant activities.

Similar to the study conducted by Huang et al., (2007) on the materials polycarbonate and epoxy, different loading rates are used on the cortical bone specimens in this study. For a material like bone which exhibits viscoelastic and viscoplastic behavior, creep induced rate effect studies so far were conducted mainly at the macroscale (Johnson et al., 2010).

In this study, micro scratch tests were conducted on the cortical bone in the longitudinal and transverse directions. Ten transverse sectioned and ten longitudinal sectioned specimens were tested for this study. On each specimen, two loading rates of 60 N/min and 90 N/min were used. For each loading rate, a diaspora of scratch speeds was adopted. For each scratch speed, at least 3 scratches were performed. This lead to a minimum of 45 micro scratch tests carried out on each specimen. In total, a minimum of 450 scratch tests were conducted in each direction. Of all the 900 tests conducted for this study, a representative test in each direction is shown below.

Table 9.1 Table showing the scratch speeds corresponding to the load rate of 60 N/min.

Fn(N/min)	V(mm/min)	Fn/V	V/Fn
60	0.4	150	0.006667
60	0.6	100	0.01
60	0.8	75	0.013333
60	1	60	0.016667

Table 9.1 (cont.)

60	2	30	0.033333
60	4	15	0.066667
60	6	10	0.1
60	8	7.5	0.133333

Table 9.2 Table showing the scratch speeds corresponding to the load rate of 90 N/min.

Fn(N/min)	**V(mm/min)**	**Fn/V**	**V/Fn**
90	0.6	150	0.006667
90	0.8	112.5	0.008889
90	1	90	0.011111
90	2	45	0.022222
90	4	22.5	0.044444
90	6	15	0.066667
90	8	11.25	0.088889

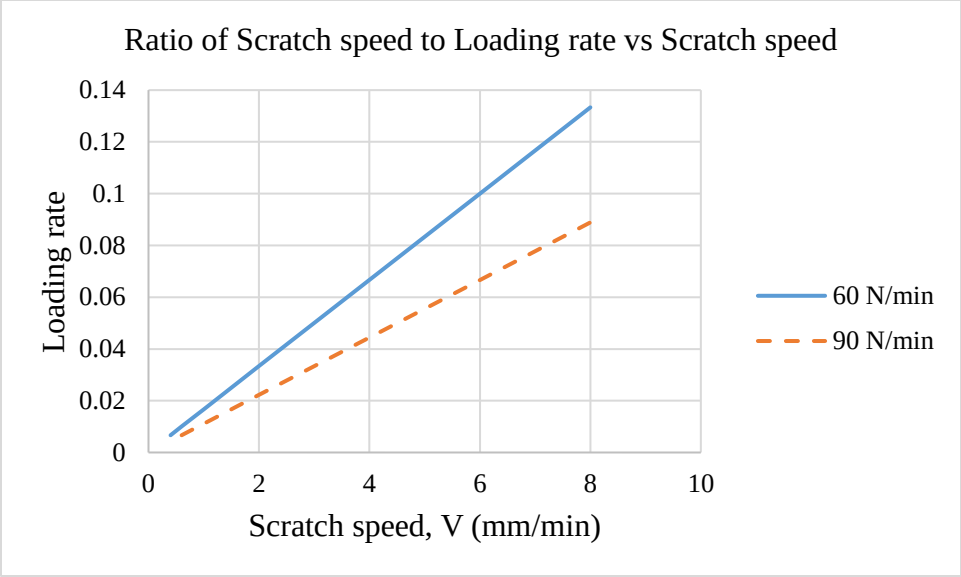

Figure 9.2 Plot showing the various scratch speeds adopted for testing the cortical bone specimens and the corresponding load rates used in this study.

Table 9.3 Parameters corresponding to the representative longitudinal specimen tested for the loading rates 60 N/min and 90 N/min.

Loading rate, Fn (N/min)	Scratch speed, V (mm/min)	Maximum load, (N)	Scratch length (µm)	Fracture Toughness, Kc (MPA/√m)	V/Fn
60	0.4	30	200	3.03	0.00667
60	0.6	30	300	3.48	0.01
60	0.8	30	400	3.75	0.01333
60	1	30	500	4.06	0.01667
60	2	30	1000	3.7	0.03333

Table 9.3 (cont.)

60	4	30	2000	4.31	0.06667
60	6	30	3000	3.09	0.1
60	8	30	4000	3.84	0.13333
90	0.6	30	200	1.74	0.00667
90	0.8	30	266.6666667	1.94	0.00889
90	1	30	333.3333333	1.96	0.01111
90	2	30	666.6666667	3.7	0.02222
90	4	30	1333.333333	3.82	0.04444
90	6	30	2000	3.49	0.06667
90	8	30	2666.666667	2.97	0.08889

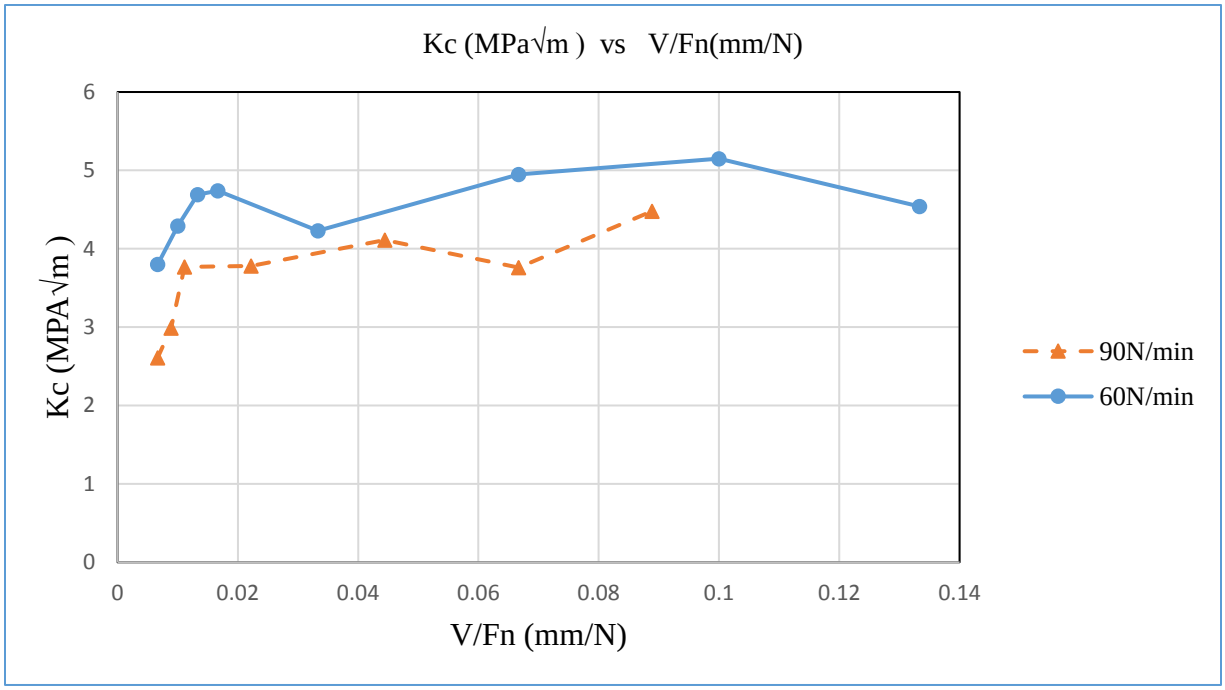

Figure 9.3 Plot showing the variation of fracture toughness with the ratio of *V/Fn* for a longitudinal cortical bone specimen.

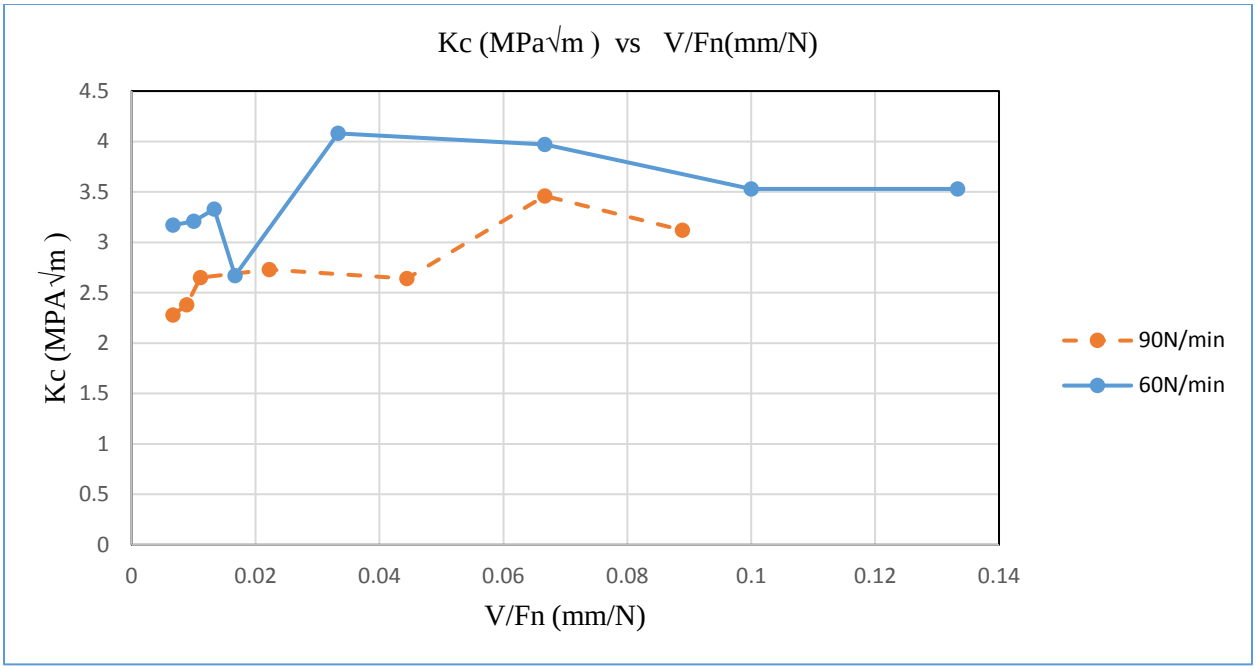

Figure 9.4 Plot showing the variation of fracture toughness with the ratio of *V/Fn* for a longitudinal cortical bone specimen.

As discussed earlier, on each transverse (SL) specimen a series of tests corresponding to both the loading rates 60N/min and 90N/min were conducted. The Figures 9.5 and 9.6 show the summary of the plots obtained for these rates, 60N/min and 90N/min respectively.

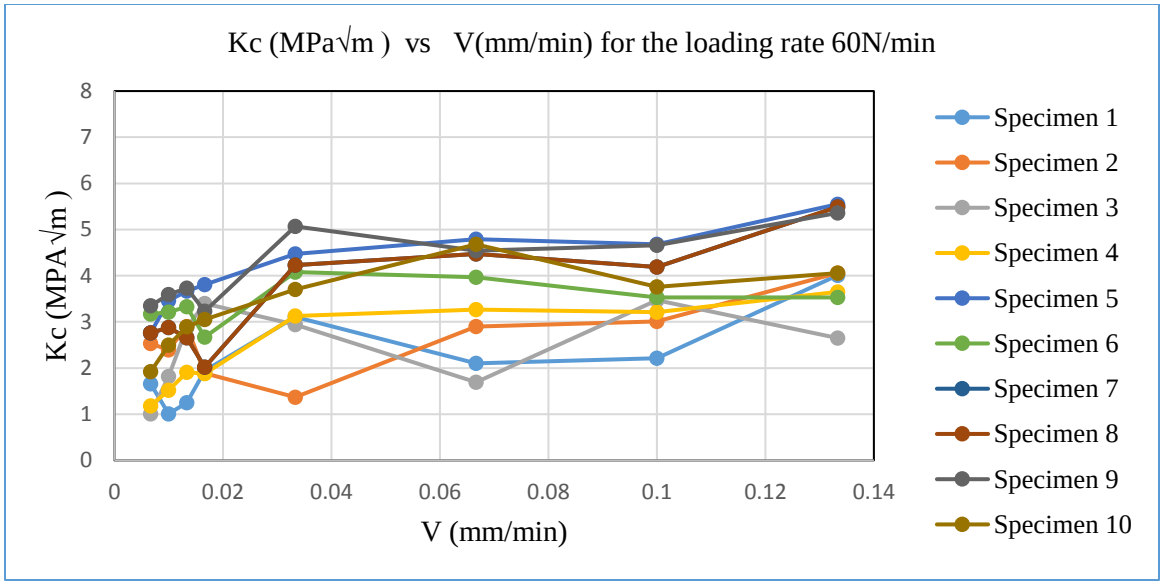

Figure 9.5 Summary of the fracture toughness vs the ratio of scratch speed to the Force *Fn* of the scratch tests performed on the transverse bovine cortical bone specimens (SL) under a loading rate of 60 N/min on 10 specimens.

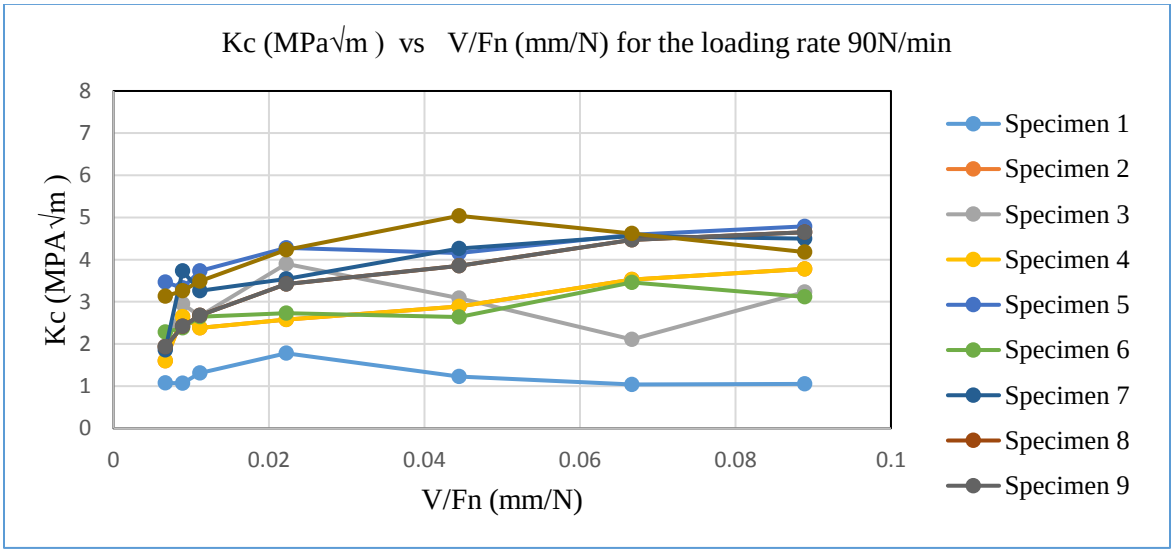

Figure 9.6 Summary of the fracture toughness vs the ratio of scratch speed to the Force *Fn* of the scratch tests performed on the transverse bovine cortical bone specimens (SL) under a loading rate of 90 N/min on 10 specimens.

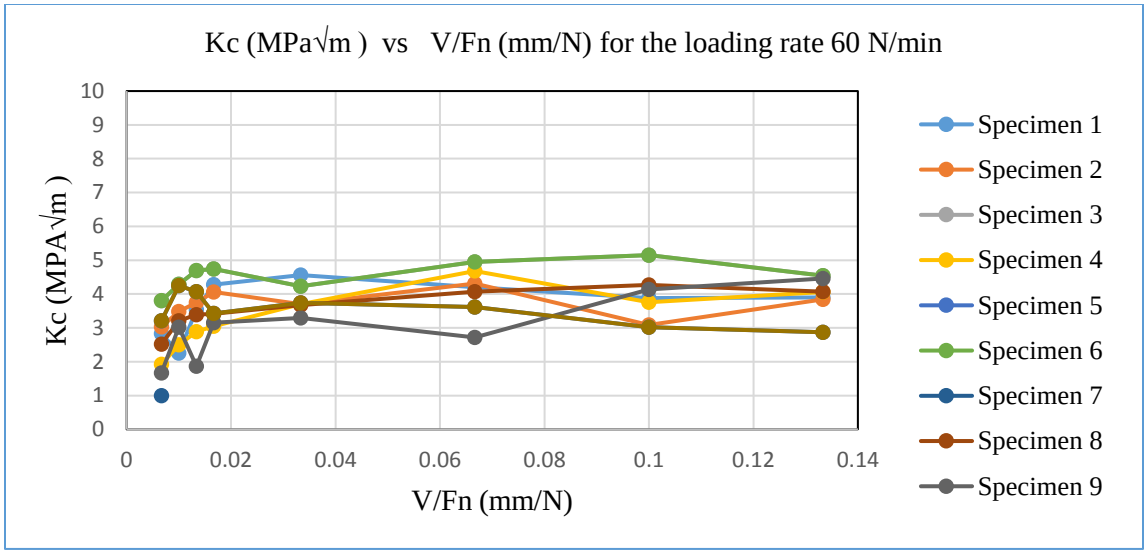

Figure 9.7 Summary of the fracture toughness vs the ratio of scratch speed to the Force *Fn* of the scratch tests performed on the longitudinal bovine cortical bone specimens (SL) under a loading rate of 90 N/min on 10 specimens.

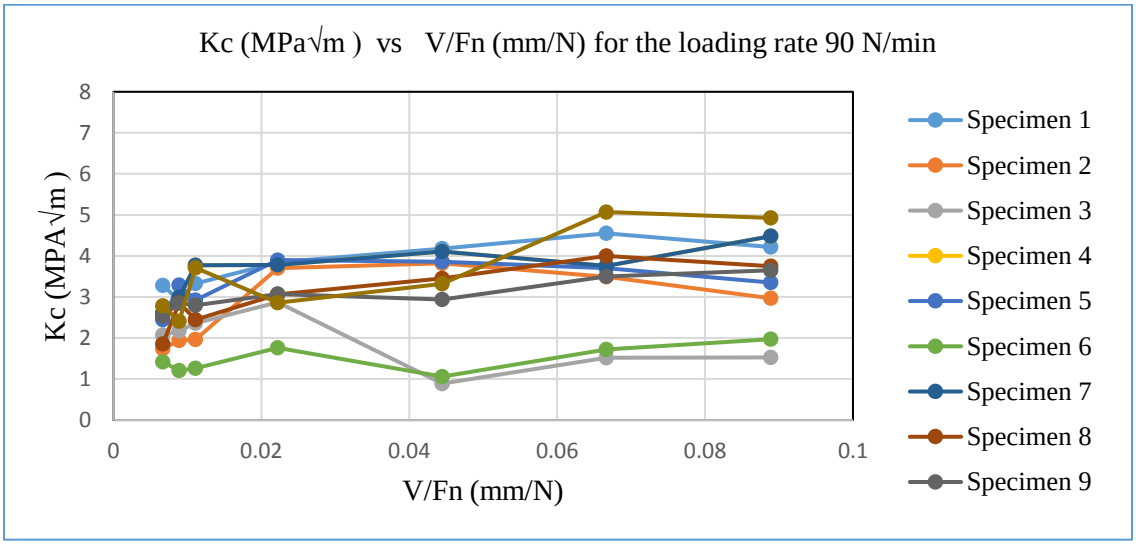

Figure 9.8 Summary of the fracture toughness vs the ratio of scratch speed to the Force *Fn* of the scratch tests performed on the longitudinal bovine cortical bone specimens (SL) under a loading rate of 90 N/min on 10 specimens.

Thus, from all the figures we observe that, for a constant loading rate, the fracture toughness tends to increase with the increase in the ratio of scratch speed to the force. However, for both the orientations, transverse and longitudinal, the fracture toughness of the bovine cortical bone specimens decreases with increase in loading rate. Furthermore, longitudinal specimens were observed to have relatively higher values of fracture toughness for the same values of loading rates and speeds.

9.3 Chapter Summary

The dynamic properties of cortical bone specimens have been studied previously. Bone displaying the behavior of viscoelasticity and viscoplasticity have been explored earlier, though mostly at the macro scale. This chapter shows a study on the fracture toughness of the cortical bone specimen at the microscopic scale. Two different loading rates in conjunction with several scratch sppeds were applied onto the longitudinal (LT) and transverse (SL) specimens and the trends in the fracture properties were reported.

CHAPTER 10

CONCLUSION AND PERSPECTIVES

This present study shows the application of novel micro scratch technique to determine the fracture toughness of the cortical bone specimens in two orientations, longitudinal and transverse considering the anisotropy of bone. It further shows the application of nanoindentation technique as well to determine the mechanical properties of the specimens. Thus, successful characterization of cortical bone specimens at small length scales such as meso, micro and sub-micron scales is shown. The meticulous specimen preparation protocol helped in preparing specimens under consistent and controlled conditions.

10.1 Summary of Findings

1. Micro scratch tests, which shows the mixed mode of fracture process in the cortical bone specimen, is a novel technique. The method determines the fracture toughness of the cortical bone specimens using non-linear fracture mechanics theory based on the J-integral calculation and the energetic size effect law.
2. Advanced imaging techniques such as Scanning electron microscopy and confocal microscopy showed the occurrence of fracture processes during these scratch tests. Further, the mechanisms such as crack bridging, micro cracking and crack deflection were reported

as well. The data from the scratch tests could show the anisotropy that exists in the bone specimens.

3. The statistical nanoindentation technique characterizes a grid of the cortical bone specimen and enables us in extracting the phase maps and modulus maps from the load displacement data obtained from the tests. This typically shows the phases in the cortical bone specimen and thus the average mechanical properties.
4. The rate effect study on the cortical bone specimens show the trends in the variation of the fracture toughness at the microscopic length scale.

10.2 Limitations and Perspectives

1. In spite of adopting a meticulous specimen preparation protocol, certain parameters like temperature and relative humidity could not be completely controlled during the testing procedure. These parameters have an influence on the microscopic properties of the cortical bone specimen. This is one of the reasons for the variability in the results.
2. Another reason for the variability might be due to the influence of the location from which the specimens were cut.
3. Creep and anisotropy of the cortical bone specimens could be addressed further by developing the advanced theoretical models.

10.3 Conclusions and Perspectives

A novel micro scratch technique was used to determine the fracture toughness of cortical bone samples. This technique addresses the mixed mode fracture of the bone specimens. This wasn't effectively captured using the macroscopic studies. Further, this method uses the complex non-linear fracture mechanics model based on the *J*-integral method to assess the fracture properties. In addition, the micro mechanisms show the fracture driven process that occurs in the cortical bone specimens post the plastic dissipation stage. The experimental results obtained also fall in the range of the values given in the literature. There by validating the application of the novel micro scratch technique to the cortical bone specimens.

BIBLIOGRAPHY

1. Ager, J., G. Balooch, and R. Ritchie, *Fracture, aging, and disease in bone.* Journal of Materials Research, 2006. **21**(08): p. 1878-1892.
2. Ager, J.W., et al., *Deep-ultraviolet Raman spectroscopy study of the effect of aging on human cortical bone.* Journal of biomedical optics, 2005. **10**(3): p. 034012-0340128.
3. Akkus, O., K. Jepsen, and C. Rimnac, *Microstructural aspects of the fracture process in human cortical bone.* Journal of Materials Science, 2000. **35**(24): p. 6065-6074.
4. Akkus, O., et al., *Aging of microstructural compartments in human compact bone.* Journal of Bone and Mineral Research, 2003. **18**(6): p. 1012-1019.
5. Akkus, O. and C.M. Rimnac, *Cortical bone tissue resists fatigue fracture by deceleration and arrest of microcrack growth.* Journal of Biomechanics, 2001. **34**(6): p. 757-764.
6. Akono, A., P. Reis, and F. Ulm, *Scratching as a fracture process: From butter to steel.* Physical review letters, 2011. **106**(20): p. 204302.
7. Akono, A.-T., N.X. Randall, and F.-J. Ulm, *Experimental determination of the fracture toughness via microscratch tests: application to polymers, ceramics, and metals.* Journal of Materials Research, 2012. **27**(02): p. 485-493.
8. Akono, A.-T. and F.-J. Ulm, *Scratch test model for the determination of fracture toughness.* Engineering Fracture Mechanics, 2011. **78**(2): p. 334-342.

9. Akono, A.-T. and F.-J. Ulm, *Fracture scaling relations for scratch tests of axisymmetric shape.* Journal of the Mechanics and Physics of Solids, 2012. **60**(3): p. 379-390.

10. Akono, A.-T. and F.-J. Ulm, *An improved technique for characterizing the fracture toughness via scratch test experiments.* Wear, 2014. **313**(1): p. 117-124.

11. Akono, A.-T., F.-J. Ulm, and Z.P. Bažant, *Discussion: Strength-to-fracture scaling in scratching.* Engineering Fracture Mechanics, 2014. **119**: p. 21-28.

12. An, Y.H. and K.L. Martin, *Handbook of histology methods for bone and cartilage*. 2003: Springer Science & Business Media.

13. Ashman, R., et al., *A continuous wave technique for the measurement of the elastic properties of cortical bone.* Journal of biomechanics, 1984. **17**(5): p. 349-361.

14. Ashman, R.B. and J.Y. Rho, *Elastic modulus of trabecular bone material.* Journal of biomechanics, 1988. **21**(3): p. 177-181.

15. ASTM, E., *384.* Standard Test Method for Microindentation Hardness of Materials, 1999.

16. Bahr, D.F., D. Kramer, and W. Gerberich, *Non-linear deformation mechanisms during nanoindentation.* Acta materialia, 1998. **46**(10): p. 3605-3617.

17. Bažant, Z.P., *Size effect in blunt fracture: concrete, rock, metal.* Journal of Engineering Mechanics, 1984. **110**(4): p. 518-535.

18. Behiri, J. and W. Bonfield, *Crack velocity dependence of longitudinal fracture in bone.* Journal of Materials Science, 1980. **15**(7): p. 1841-1849.

19. Blobe, G.C., W.P. Schiemann, and H.F. Lodish, *Role of transforming growth factor β in human disease.* New England Journal of Medicine, 2000. **342**(18): p. 1350-1358.

20. Bobji, M. and S. Biswas, *Estimation of hardness by nanoindentation of rough surfaces.* Journal of Materials Research, 1998. **13**(11): p. 3227-3233.

21. Bonfield, W., *Advances in the fracture mechanics of cortical bone.* Journal of biomechanics, 1987. **20**(11-12): p. 1071-1081.

22. Bonfield, W., J. Behiri, and B. Cullen, *Orientation and age-related dependence of the fracture toughness of cortical bone.* Journal of Biomechanics, 1985. **18**(7): p. 521-522.

23. Bonfield, W. and P. Datta, *Fracture toughness of compact bone.* Journal of Biomechanics, 1976. **9**(3): p. 131IN5133-132134.

24. Borah, B., et al., *The effect of risedronate on bone mineralization as measured by micro-computed tomography with synchrotron radiation: correlation to histomorphometric indices of turnover.* Bone, 2005. **37**(1): p. 1-9.

25. Boussinesq, J., *Application des potentiels à l'étude de l'équilibre et du mouvement des solides élastiques*. 1885: Gauthier-Villars.

26. Bowden, F. and D. Tabor, *The Friction and Lubrication of Solids II.* Clarendon Press, Oxford, 1964. **19**: p. 64.

27. Briscoe, B., L. Fiori, and E. Pelillo, *Nano-indentation of polymeric surfaces.* Journal of Physics D: Applied Physics, 1998. **31**(19): p. 2395.

28. Brown, C.U., Y.N. Yeni, and T.L. Norman, *Fracture toughness is dependent on bone location—a study of the femoral neck, femoral shaft, and the tibial shaft.* Journal of Biomedical Materials Research Part A, 2000. **49**(3): p. 380-389.

29. Broz, J., S. Simske, and A. Greenberg, *Material and compositional properties of selectively demineralized cortical bone.* Journal of biomechanics, 1995. **28**(11): p. 13571365-13631368.

30. Burr, D. and M. Hooser, *Alterations to the en bloc basic fuchsin staining protocol for the demonstration of microdamage produced in vivo.* Bone, 1995. **17**(4): p. 431-433.

31. Burr, D.B., et al., *Bone remodeling in response to in vivo fatigue microdamage.* Journal of biomechanics, 1985. **18**(3): p. 189-200.

32. Burr, D.B., M.B. Schaffler, and R.G. Frederickson, *Composition of the cement line and its possible mechanical role as a local interface in human compact bone.* Journal of Biomechanics, 1988. **21**(11): p. 939943-941945.

33. Burr, D.B., et al., *Does microdamage accumulation affect the mechanical properties of bone?* Journal of biomechanics, 1998. **31**(4): p. 337-345.

34. Burstein, A.H., et al., *The ultimate properties of bone tissue: the effects of yielding.* Journal of biomechanics, 1972. **5**(1): p. 35IN143-42IN244.

35. Burstein, A.H., D.T. Reilly, and M. Martens, *Aging of bone tissue: mechanical properties.* J Bone Joint Surg Am, 1976. **58**(1): p. 82-86.

36. Carden, A., et al., *Ultrastructural changes accompanying the mechanical deformation of bone tissue: a Raman imaging study.* Calcified Tissue International, 2003. **72**(2): p. 166-175.

37. Carnelli, D., et al., *Nanoindentation testing and finite element simulations of cortical bone allowing for anisotropic elastic and inelastic mechanical response.* Journal of biomechanics, 2011. **44**(10): p. 1852-1858.

38. Carter, D., W.C. Hayes, and D.J. Schurman, *Fatigue life of compact bone—II. Effects of microstructure and density.* Journal of biomechanics, 1976. **9**(4): p. 211-218.

39. Carter, D.R. and W.C. Hayes, *The compressive behavior of bone as a two-phase porous structure.* The Journal of Bone & Joint Surgery, 1977. **59**(7): p. 954-962.

40. Chen, T.-C., D. Shea, and M.D. Morris, *Effect of hydrogen peroxide bleaching on bone mineral/matrix ratio.* Applied spectroscopy, 2002. **56**(8): p. 1035-1037.

41. Currey, J., *'Osteons' in biomechanical literature.* Journal of biomechanics, 1982. **15**(9): p. 717.

42. Currey, J.D., *The structure and mechanics of bone.* Journal of Materials Science, 2012. **47**(1): p. 41-54.

43. De Groot, K., et al., *Plasma sprayed coatings of hydroxylapatite.* Journal of biomedical materials research, 1987. **21**(12): p. 1375-1381.

44. EVans, A.G. and E.A. Charles, *Fracture toughness determinations by indentation.* Journal of the American Ceramic society, 1976. **59**(7-8): p. 371-372.

45. Feng, L., et al., *Mechanical properties of porcine femoral cortical bone measured by nanoindentation.* Journal of biomechanics, 2012. **45**(10): p. 1775-1782.

46. Feng, L. and I. Jasiuk, *Multi-scale characterization of swine femoral cortical bone.* Journal of biomechanics, 2011. **44**(2): p. 313-320.

47. Feng, Z., et al., *Orientation and loading condition dependence of fracture toughness in cortical bone.* Materials Science and Engineering: C, 2000. **11**(1): p. 41-46.

48. Forwood, M.R. and A.W. Parker, *Repetitive loading, in vivo, of the tibiae and femora of rats: effects of repeated bouts of treadmill-running.* Bone and mineral, 1991. **13**(1): p. 35-46.

49. Fratzl, P., et al., *Structure and mechanical quality of the collagen–mineral nano-composite in bone.* Journal of materials chemistry, 2004. **14**(14): p. 2115-2123.

50. Fritsch, A. and C. Hellmich, *'Universal'microstructural patterns in cortical and trabecular, extracellular and extravascular bone materials: Micromechanics-based prediction of anisotropic elasticity.* Journal of Theoretical Biology, 2007. **244**(4): p. 597-620.

51. Fritsch, A., C. Hellmich, and L. Dormieux, *Ductile sliding between mineral crystals followed by rupture of collagen crosslinks: experimentally supported micromechanical explanation of bone strength.* Journal of Theoretical Biology, 2009. **260**(2): p. 230-252.

52. Frost, H.M., *Bone "mass" and the "mechanostat": a proposal.* The anatomical record, 1987. **219**(1): p. 1-9.

53. Fyhrie, D.P. and R. Zauel, *Directional tortuosity as a predictor of modulus damage for vertebral cancellous bone.* Journal of biomechanical engineering, 2015. **137**(1): p. 011007.

54. Gonczy, S.T. and N. Randall, *An ASTM standard for quantitative scratch adhesion testing of thin, hard ceramic coatings.* International Journal of Applied Ceramic Technology, 2005. **2**(5): p. 422-428.

55. Gupta, H.S., *Mechanisms of bone deformation and fracture.* IBMS BoneKEy, 2010. **7**(6): p. 218-228.

56. Habelitz, S., et al., *Nanoindentation and storage of teeth.* Journal of biomechanics, 2002. **35**(7): p. 995-998.

57. Hang, F. and A.H. Barber, *Nano-mechanical properties of individual mineralized collagen fibrils from bone tissue.* Journal of The Royal Society Interface, 2011. **8**(57): p. 500-505.

58. Health, U.D.o. and H. Services, *Bone health and osteoporosis: a report of the Surgeon General.* Rockville, MD: US Department of Health and Human Services, Office of the Surgeon General, 2004. **87**.

59. Heaney, R.P., *Is the paradigm shifting?* Bone, 2003. **33**(4): p. 457-465.

60. Hellmich, C. and F.-J. Ulm, *Micromechanical model for ultrastructural stiffness of mineralized tissues.* Journal of engineering mechanics, 2002. **128**(8): p. 898-908.

61. Hengsberger, S., A. Kulik, and P. Zysset, *A combined atomic force microscopy and nanoindentation technique to investigate the elastic properties of bone structural units.* Eur. Cells Mater, 2001. **1**: p. 12-17.

62. Hengsberger, S., A. Kulik, and P. Zysset, *Nanoindentation discriminates the elastic properties of individual human bone lamellae under dry and physiological conditions.* Bone, 2002. **30**(1): p. 178-184.

63. Hill, M.A., *Bone Histology.* Embryology, 2017.

64. Hoc, T., et al., *Effect of microstructure on the mechanical properties of Haversian cortical bone.* Bone, 2006. **38**(4): p. 466-474.

65. Hodgskinson, R. and J. Currey, *Young's modulus, density and material properties in cancellous bone over a large density range.* Journal of Materials Science: Materials in Medicine, 1992. **3**(5): p. 377-381.

66. Hoffler, C.E., et al., *An application of nanoindentation technique to measure bone tissue lamellae properties.* Journal of biomechanical engineering, 2005. **127**(7): p. 1046-1053.

67. Huang, L., J. Lu, and K. Xu, *Elasto-plastic deformation and fracture mechanism of a diamond-like carbon film deposited on a Ti–6Al–4V substrate in nano-scratch test.* Thin Solid Films, 2004. **466**(1): p. 175-182.

68. Hui, S.L., C.W. Slemenda, and C.C. Johnston Jr, *Age and bone mass as predictors of fracture in a prospective study.* Journal of clinical investigation, 1988. **81**(6): p. 1804.

69. Islam, A., X.N. Dong, and X. Wang, *Mechanistic modeling of a nanoscratch test for determination of in situ toughness of bone.* Journal of the mechanical behavior of biomedical materials, 2012. **5**(1): p. 156-164.

70. Kanis, J., et al., *A new approach to the development of assessment guidelines for osteoporosis.* Osteoporosis International, 2002. **13**(7): p. 527-536.

71. Koester, K.J., J. Ager, and R. Ritchie, *The true toughness of human cortical bone measured with realistically short cracks.* Nature materials, 2008. **7**(8): p. 672-677.

72. Kruzic, J., et al., *Indentation techniques for evaluating the fracture toughness of biomaterials and hard tissues.* Journal of the Mechanical Behavior of Biomedical Materials, 2009. **2**(4): p. 384-395.

73. Lee, T.C., et al., *Detecting microdamage in bone.* Journal of Anatomy, 2003. **203**(2): p. 161-172.

74. Linde, F., et al., *Mechanical properties of trabecular bone. Dependency on strain rate.* Journal of Biomechanics, 1991. **24**(9): p. 803-809.

75. Linde, F. and H.C.F. Sørensen, *The effect of different storage methods on the mechanical properties of trabecular bone.* Journal of biomechanics, 1993. **26**(10): p. 1249-1252.

76. Lucksanasombool, P., et al., *Fracture toughness of bovine bone: influence of orientation and storage media.* Biomaterials, 2001. **22**(23): p. 3127-3132.

77. Marshall, D., O. Johnell, and H. Wedel, *Meta-analysis of how well measures of bone mineral density predict occurrence of osteoporotic fractures.* Bmj, 1996. **312**(7041): p. 1254-1259.

78. Martin, R.B., *Determinants of the mechanical properties of bones.* Journal of biomechanics, 1991. **24**: p. 79-88.

79. Martin, R.B., D.B. Burr, and N.A. Sharkey, *Skeletal tissue mechanics*. Vol. 190. 1998: Springer.

80. McAlden, R., J. McGeogh, and M. Barker, *Court-Brown C (1993) Age related changes in the tensile properties of cortical bone: the relative importance of changes in porosity, mineralization and microstructure.* J Bone Joint Surg Am: p. 1193-1205.

81. Mccalden, R.W., J.A. McGeough, and M.B. Barker, *Age-related changes in the tensile properties of cortical bone. The relative importance of changes in porosity, mineralization, and microstructure.* J Bone Joint Surg Am, 1993. **75**(8): p. 1193-1205.

82. Melvin, J. and F. Evans. *Crack propagation in bone*. in *ASME Biomechanics Symposium, New York*. 1973.

83. Melvin, J.W., *Fracture mechanics of bone.* TRANSACTIONS-AMERICAN SOCIETY OF MECHANICAL ENGINEERS JOURNAL OF BIOMECHANICAL ENGINEERING, 1993. **115**: p. 549-549.

84. Mohsin, S., F.J. O'Brien, and T.C. Lee, *Osteonal crack barriers in ovine compact bone.* Journal of anatomy, 2006. **208**(1): p. 81-89.

85. Mori, S. and D. Burr, *Increased intracortical remodeling following fatigue damage.* Bone, 1993. **14**(2): p. 103-109.

86. Mullins, L., M. Bruzzi, and P. McHugh, *Measurement of the microstructural fracture toughness of cortical bone using indentation fracture.* Journal of Biomechanics, 2007. **40**(14): p. 3285-3288.

87. Nalla, R.K., J.H. Kinney, and R.O. Ritchie, *Mechanistic fracture criteria for the failure of human cortical bone.* Nature materials, 2003. **2**(3): p. 164-168.

88. Nalla, R.K., et al., *Mechanistic aspects of fracture and R-curve behavior in human cortical bone.* Biomaterials, 2005. **26**(2): p. 217-231.

89. Norman, T.L., D. Vashishth, and D. Burr, *Effect of groove on bone fracture toughness.* Journal of biomechanics, 1992. **25**(12): p. 1489-1492.

90. Norman, T.L., D. Vashishth, and D. Burr, *Fracture toughness of human bone under tension.* Journal of biomechanics, 1995. **28**(3): p. 309313-311320.

91. Norman, T.L. and Z. Wang, *Microdamage of human cortical bone: incidence and morphology in long bones.* Bone, 1997. **20**(4): p. 375-379.

92. Norman, T.L., et al., *Influence of microdamage on fracture toughness of the human femur and tibia.* Bone, 1998. **23**(3): p. 303-306.

93. Nyman, J.S., et al., *Measuring differences in compositional properties of bone tissue by confocal Raman spectroscopy.* Calcified tissue international, 2011. **89**(2): p. 111-122.

94. Nyman, J.S., M. Reyes, and X. Wang, *Effect of ultrastructural changes on the toughness of bone.* Micron, 2005. **36**(7): p. 566-582.

95. Oliver, W.C. and G.M. Pharr, *An improved technique for determining hardness and elastic modulus using load and displacement sensing indentation experiments.* Journal of materials research, 1992. **7**(06): p. 1564-1583.

96. Oliver, W.C. and G.M. Pharr, *Measurement of hardness and elastic modulus by instrumented indentation: Advances in understanding and refinements to methodology.* Journal of materials research, 2004. **19**(01): p. 3-20.

97. Parfitt, A.M., *Bone age, mineral density, and fatigue damage.* Calcified tissue international, 1993. **53**: p. S82-S86.

98. Parsamian, G.P. and T.L. Norman, *Diffuse damage accumulation in the fracture process zone of human cortical bone specimens and its influence on fracture toughness.* Journal of Materials Science: Materials in Medicine, 2001. **12**(9): p. 779-783.

99. Pharr, G. and W. Oliver, *Measurement of thin film mechanical properties using nanoindentation.* Mrs Bulletin, 1992. **17**(07): p. 28-33.

100. Phelps, J., et al., *Microstructural heterogeneity and the fracture toughness of bone.* Journal of biomedical materials research, 2000. **51**(4): p. 735-741.

101. Piekarski, K., *Fracture of bone.* Journal of applied physics, 1970. **41**(1): p. 215-223.

102. Piga, G., et al., *Is X-ray diffraction able to distinguish between animal and human bones?* Journal of archaeological science, 2013. **40**(1): p. 778-785.

103. Pope, M. and J. Outwater, *The fracture characteristics of bone substance.* Journal of Biomechanics, 1972. **5**(5): p. 457IN3461-460IN5465.

104. Randall, N., G. Favaro, and C. Frankel, *The effect of intrinsic parameters on the critical load as measured with the scratch test method.* Surface and Coatings Technology, 2001. **137**(2): p. 146-151.

105. Reilly, D.T. and A.H. Burstein, *The mechanical properties of cortical bone.* JBJS, 1974. **56**(5): p. 1001-1022.

106. Reilly, D.T. and A.H. Burstein, *The elastic and ultimate properties of compact bone tissue.* Journal of biomechanics, 1975. **8**(6): p. 393IN9397-396IN11405.

107. Reilly, G.C. and J.D. Currey, *The effects of damage and microcracking on the impact strength of bone.* Journal of biomechanics, 2000. **33**(3): p. 337-343.

108. Rho, J.Y., R.B. Ashman, and C.H. Turner, *Young's modulus of trabecular and cortical bone material: ultrasonic and microtensile measurements.* Journal of biomechanics, 1993. **26**(2): p. 111-119.

109. Rho, J.-Y., L. Kuhn-Spearing, and P. Zioupos, *Mechanical properties and the hierarchical structure of bone.* Medical engineering & physics, 1998. **20**(2): p. 92-102.

110. Rho, J.-Y. and G.M. Pharr, *Effects of drying on the mechanical properties of bovine femur measured by nanoindentation.* Journal of Materials Science: Materials in Medicine, 1999. **10**(8): p. 485-488.

111. Rho, J.-Y., T.Y. Tsui, and G.M. Pharr, *Elastic properties of human cortical and trabecular lamellar bone measured by nanoindentation.* Biomaterials, 1997. **18**(20): p. 1325-1330.

112. Rinnerthaler, S., et al., *Scanning small angle X-ray scattering analysis of human bone sections.* Calcified tissue international, 1999. **64**(5): p. 422-429.

113. Ritchie, R., *Mechanisms of fatigue crack propagation in metals, ceramics and composites: role of crack tip shielding.* Materials Science and Engineering: A, 1988. **103**(1): p. 15-28.

114. Ritchie, R., et al., *Fracture and ageing in bone: toughness and structural characterization.* Strain, 2006. **42**(4): p. 225-232.

115. Ritchie, R.O., *How does human bone resist fracture?* Annals of the New York Academy of Sciences, 2010. **1192**(1): p. 72-80.

116. Ritchie, R.O., *The conflicts between strength and toughness.* Nat Mater, 2011. **10**(11): p. 817-822.

117. Ritchie, R.O., M.J. Buehler, and P. Hansma, *Plasticity and toughness in bone.* Physics Today, 2009. **62**(6): p. 41-47.

118. Rockwell, H.M. and S.P. Rockwell, *Hardness-tester*. 1919, Google Patents.

119. Saha, S. and W. Hayes, *Relations between tensile impact properties and microstructure of compact bone.* Calcified Tissue International, 1977. **24**(1): p. 65-72.

120. Sardela, M., *Practical Materials Characterization*. 2014: Springer.

121. Schaffler, M., K. Choi, and C. Milgrom, *Aging and matrix microdamage accumulation in human compact bone.* Bone, 1995. **17**(6): p. 521-525.

122. Schaffler, M., E. Radin, and D. Burr, *Long-term fatigue behavior of compact bone at low strain magnitude and rate.* Bone, 1990. **11**(5): p. 321-326.

123. Schaffler, M.B. and D.B. Burr, *Stiffness of compact bone: effects of porosity and density.* Journal of biomechanics, 1988. **21**(1): p. 13-16.

124. Sneddon, I.N., *The relation between load and penetration in the axisymmetric Boussinesq problem for a punch of arbitrary profile.* International journal of engineering science, 1965. **3**(1): p. 47-57.

125. Sorelli, L., et al., *The nano-mechanical signature of ultra high performance concrete by statistical nanoindentation techniques.* Cement and Concrete Research, 2008. **38**(12): p. 1447-1456.

126. Stefan, U., B. Michael, and S. Werner, *Effects of three different preservation methods on the mechanical properties of human and bovine cortical bone.* Bone, 2010. **47**(6): p. 1048-1053.

127. Stilwell, N. and D. Tabor, *Elastic recovery of conical indentations.* Proceedings of the Physical Society, 1961. **78**(2): p. 169.

128. Tabor, D., *The hardness of metals*. 2000: Oxford university press.

129. Tai, K., H.J. Qi, and C. Ortiz, *Effect of mineral content on the nanoindentation properties and nanoscale deformation mechanisms of bovine tibial cortical bone.* Journal of Materials Science: Materials in Medicine, 2005. **16**(10): p. 947-959.

130. Tang, S. and D. Vashishth, *The relative contributions of non-enzymatic glycation and cortical porosity on the fracture toughness of aging bone.* Journal of biomechanics, 2011. **44**(2): p. 330-336.

131. Townsend, P.R., R.M. Rose, and E.L. Radin, *Buckling studies of single human trabeculae.* Journal of biomechanics, 1975. **8**(3-4): p. 199IN5201-200IN6.

132. Turner, C.H. and D.B. Burr, *Basic biomechanical measurements of bone: a tutorial.* Bone, 1993. **14**(4): p. 595-608.

133. Ulm, F.J., et al., *Statistical indentation techniques for hydrated nanocomposites: concrete, bone, and shale.* Journal of the American Ceramic Society, 2007. **90**(9): p. 2677-2692.

134. Vashishth, D., J. Behiri, and W. Bonfield, *Crack growth resistance in cortical bone: concept of microcrack toughening.* Journal of biomechanics, 1997. **30**(8): p. 763-769.

135. Vashishth, D., et al., *Influence of nonenzymatic glycation on biomechanical properties of cortical bone.* Bone, 2001. **28**(2): p. 195-201.

136. Vashishth, D., K. Tanner, and W. Bonfield, *Contribution, development and morphology of microcracking in cortical bone during crack propagation.* Journal of Biomechanics, 2000. **33**(9): p. 1169-1174.

137. Vashishth, D., K. Tanner, and W. Bonfield, *Fatigue of cortical bone under combined axial-torsional loading.* Journal of Orthopaedic Research, 2001. **19**(3): p. 414-420.

138. Wang, X. and C. Agrawal, *A mixed mode fracture toughness test of bone–biomaterial interfaces.* Journal of Biomedical Materials Research Part A, 2000. **53**(6): p. 664-672.

139. Wang, X., et al., *The role of collagen in determining bone mechanical properties.* Journal of orthopaedic research, 2001. **19**(6): p. 1021-1026.

140. Wang, X., J. Lankford, and C. Agrawal, *Use of a compact sandwich specimen to evaluate fracture toughness and interfacial bonding of bone.* Journal of Applied Biomaterials, 1994. **5**(4): p. 315-323.

141. Wang, X., Y. Yoon, and H. Ji, *A novel scratching approach for measuring age-related changes in the in situ toughness of bone.* Journal of biomechanics, 2007. **40**(6): p. 1401-1404.

142. Weiner, S. and H.D. Wagner, *The material bone: structure-mechanical function relations.* Annual Review of Materials Science, 1998. **28**(1): p. 271-298.

143. Wenzel, T., M. Schaffler, and D.P. Fyhrie, *In vivo trabecular microcracks in human vertebral bone.* Bone, 1996. **19**(2): p. 89-95.

144. Willems, G., et al., *Hardness and Young's modulus determined by nanoindentation technique of filler particles of dental restorative materials compared with human enamel.* Journal of biomedical materials research, 1993. **27**(6): p. 747-755.

145. Wimmer, R., et al., *Longitudinal hardness and Young's modulus of spruce tracheid secondary walls using nanoindentation technique.* Wood Science and Technology, 1997. **31**(2): p. 131-141.

146. Witte, F., et al., *Degradable biomaterials based on magnesium corrosion.* Current opinion in solid state and materials science, 2008. **12**(5): p. 63-72.

147. Wright, T. and W. Hayes, *Fracture mechanics parameters for compact bone—effects of density and specimen thickness.* Journal of Biomechanics, 1977. **10**(7): p. 419427-425430.

148. Xi, Y. and Z.P. Bažant, *Modeling chloride penetration in saturated concrete.* Journal of Materials in Civil Engineering, 1999. **11**(1): p. 58-65.

149. Xu, J., et al., *Atomic force microscopy and nanoindentation characterization of human lamellar bone prepared by microtome sectioning and mechanical polishing technique.* Journal of Biomedical Materials Research Part A, 2003. **67**(3): p. 719-726.

150. Yamashita, J., et al., *The use of dynamic mechanical analysis to assess the viscoelastic properties of human cortical bone.* Journal of biomedical materials research, 2001. **58**(1): p. 47-53.

151. Yan, J., et al., *Fracture toughness of manatee rib and bovine femur using a chevron-notched beam test.* Journal of biomechanics, 2006. **39**(6): p. 1066-1074.

152. Yan, J., J.J. Mecholsky, and K.B. Clifton, *How tough is bone? Application of elastic–plastic fracture mechanics to bone.* Bone, 2007. **40**(2): p. 479-484.

153. Yeni, Y., C. Brown, and T.L. Norman, *Influence of bone composition and apparent density on fracture toughness of the human femur and tibia.* Bone, 1998. **22**(1): p. 79-84.

154. Yeni, Y., et al., *The influence of bone morphology on fracture toughness of the human femur and tibia.* Bone, 1997. **21**(5): p. 453-459.

155. Yeni, Y.N. and D.P. Fyhrie, *A rate-dependent microcrack-bridging model that can explain the strain rate dependency of cortical bone apparent yield strength.* Journal of biomechanics, 2003. **36**(9): p. 1343-1353.

156. Yerramshetty, J.S. and O. Akkus, *The associations between mineral crystallinity and the mechanical properties of human cortical bone.* Bone, 2008. **42**(3): p. 476-482.

157. Zimmermann, E.A., H.D. Barth, and R.O. Ritchie, *The multiscale origins of fracture resistance in human bone and its biological degradation.* Jom, 2012. **64**(4): p. 486-493.

158. Zimmermann, E.A., et al., *Fracture resistance of human cortical bone across multiple length-scales at physiological strain rates.* Biomaterials, 2014. **35**(21): p. 5472-5481.

159. Zimmermann, E.A., et al., *Mixed-mode fracture of human cortical bone.* Biomaterials, 2009. **30**(29): p. 5877-5884.

160. Zimmermann, E.A., M.E. Launey, and R.O. Ritchie, *The significance of crack-resistance curves to the mixed-mode fracture toughness of human cortical bone.* Biomaterials, 2010. **31**(20): p. 5297-5305.

161. Zimmermann, E.A., et al., *Age-related changes in the plasticity and toughness of human cortical bone at multiple length scales.* Proceedings of the National Academy of Sciences, 2011. **108**(35): p. 14416-14421.

162. Zioupos, P., *Accumulation of in-vivo fatigue microdamage and its relation to biomechanical properties in ageing human cortical bone.* Journal of microscopy, 2001. **201**(2): p. 270-278.

163. Zioupos, P. and J. Currey, *Changes in the stiffness, strength, and toughness of human cortical bone with age.* Bone, 1998. **22**(1): p. 57-66.

164. Zioupos, P., M. Gresle, and K. Winwood, *Fatigue strength of human cortical bone: age, physical, and material heterogeneity effects.* Journal of biomedical materials research part A, 2008. **86**(3): p. 627-636.

165. Zysset, P.K., et al., *Elastic modulus and hardness of cortical and trabecular bone lamellae measured by nanoindentation in the human femur.* Journal of biomechanics, 1999. **32**(10): p. 1005-1012.